Measurement of a High-Intensity Gamma-Ray Beam and the Analyzing Power for $^2\mathrm{H}(\vec{\gamma}, \mathrm{n})\mathrm{p}$ Near Threshhold

by

Eric C. Schreiber

Department of Physics
Duke University

Date

Approved:

Henry R. Weller, Supervisor

Vladimir Litvinenko

Berndt Mueller

Patrick O'Shea

John Thomas

Dissertation submitted in partial fulfillment of
the requirements for the degree of
Doctor of Philosophy in the Department of
Physics in the Graduate School
of Duke University

2000

Abstract

(Physics – TUNL)

Measurement of a High-Intensity Gamma-Ray Beam and the Analyzing Power for $^2\mathrm{H}(\vec{\gamma}, \mathrm{n})\mathrm{p}$ Near Threshhold

by

Eric C. Schreiber

Department of Physics
Duke University

Date

Approved:

Henry R. Weller, Supervisor

Vladimir Litvinenko

Berndt Mueller

Patrick O'Shea

John Thomas

An abstract of a dissertation submitted in partial
fulfillment of the requirements for the degree
of Doctor of Philosophy in the Department
of Physics in the Graduate School
of Duke University

2000

Abstract

Measurement of a High-Intensity Gamma-Ray Beam, and the Analyzing Power for $^2\mathrm{H}(\vec{\gamma},\mathrm{n})\mathrm{p}$ Near Threshold

The Duke Free-Electron Laser Laboratory and Triangle Universities Nuclear Laboratory have developed a free-electron laser-based γ-ray facility. Gamma-rays are generated by the intracavity Compton scattering FEL photons from high-energy electrons in the Duke storage ring. The facility is predicted to be capable of producing γ-rays having energies between 2 and 200 MeV at fluxes as high as $10^{11}\gamma$'s/sec over all energies. Energy resolutions as low as $\Delta E/E = 0.1\%$ will be achievable by collimating the γ-ray beam, and the γ-rays will be 100% linearly polarized. This dissertation documents experiments which demonstrated operation between 2.76 and 55 MeV at fluxes as high as 10^7 γ's/sec and energy resolutions as low as to $\Delta E/E = 0.76\%$. Gamma-ray beams within this range have been used to perform the first nuclear physics experiment at this facility, the near-threshold photodisintegration of deuterium at $E_\gamma = 3.58$ MeV. A measurement of the analyzing power at $\theta = 150^\circ$ was used to extract the relative E1 and M1 contributions to the cross section. The results are in good agreement with both two-body calculations and effective field theory

calculations.

Acknowledgements

The nature of the γ-ray project gave me the opportunity to work with two excellent laboratories, Triangle Universities Nuclear Laboratory and the Duke Free-Electron Laser Laboratory. Between these labs, there are many people to thank, without whom my experiment never would have happened at all, let alone succeeded. My advisor, Henry Weller, has been a source of knowledge, motivation, and enthusiasm throughout my years here. Vladimir Litvinenko and Patrick O'Shea have also provided a great deal of encouragement and advice throughout the development of this project. I would also like to thank the two directors of TUNL during my tenure here, Werner Tornow and N. Russell Roberson, for their support of both the HIGS project, and of me personally. Outside of TUNL and DFELL, Blaine Norum and Richard Prior have been a tremendous help.

Most of the work done on this project was accomplished by working with postdocs and other grad students, and I am indebted to all of them. The Radiative Capture Group at TUNL has been a great source of assistance and entertainment for all my years here. Grad students Brian Rice, Mark Godwin, Greg Schmidt, Eric Wulf, Shane Canon, Steve Nelson, Konstantin Sabourov, and Brendan Crowley have all helped make this a fun and productive place to be. Postdocs John "Ned" Kelley, Sally Gaff, and Mark Spraker have all been great sources of information and support. Students and postdocs from DFELL, Bentley Burnham, Ying Wu, Seong Hee Park, and Igor Pinayev, were invaluable collaborators, as well as being fun to work with.

When I started graduate school, the HIGS facility had just gotten over being a hole in the ground. The technical staff at TUNL and DFELL has been tremendous

in getting the facility up and running, and in helping with my own unique requests. They never seemed to mind that I kept coming to them asking for strange things that nobody had ever asked for before. From TUNL, Richard O'Quinn, John Dunham, and Paul Carter have all, at various times, cheerfully undertaken the occasionally ridiculous requests I've had for them, and Sidney Edwards and Patrick Mulkey helped transplant a bit of TUNL over to FEL to make nuclear experiments possible. At FEL, Owen Oakley, Joe Faircloth, Janet Patterson, Mark Emamian, Gary Swift, Jim Murphy, and operators Jim Gustavsson and Brian Hoffman all helped make my experiments run as smoothly as possible.

To say that the only people who helped get me through graduate school were the ones who helped me with my work would be horribly wrong. The people I've met here have made what was a trying experience into one of the best times of my life. Thanks to Greg, Mark, Mike, Wulf, Alex, Nate, Ab, Ben, Karen, Jen, Mari, Linda, Jeff, Bill, and everyone else who has been part of my life here at Duke.

A special thank you has to go to Lisa Criscione, who I met pretty much exactly as things at the FEL came crashing to an extended halt, making me suspect the existence of some conservation law for good things in my life. Even if there were such a law, I'd make the same exchange again in a second.

Finally, I want to thank my family for years of encouragement and support, and for giving me something to live up to. Now, finally, my parents can stop trying to explain to people why their son is STILL in school.

Contents

List of Figures

List of Tables

Chapter 1

Introduction

This dissertation describes a High-Intensity Gamma-ray Source (HIGS) and the use of this facility to measure a polarization asymmetry in the $^2\mathrm{H}(\vec{\gamma},\mathrm{n})\mathrm{p}$ reaction at γ-ray energies near the deuteron breakup threshold. The HIGS facility has many useful characteristics that will allow many previously difficult or impossible nuclear physics experiments to be undertaken. The first of these measurements, the $^2\mathrm{H}(\vec{\gamma},\mathrm{n})\mathrm{p}$ analyzing power, uses the flux, energy resolution, and polarization of the HIGS γ-ray beam to extract electromagnetic properties of the deuteron in an energy region where little previous data are available.

1.1 Photonuclear Physics

The primary motivation for the development of a high-intensity γ-ray source comes from the utility of using electromagnetic interactions to study the nucleus. Because a nucleus can not be observed directly, its properties must be inferred by

observing the interaction between the nucleus and some incident particle or field. These observations can be compared to the predictions of theoretical models to test our understanding of the underlying processes.

In general, a nuclear reaction can be described using complex transition matrix elements (TME). Determining the TMEs for a reaction defines the underlying physics. The TME is approximately defined as

$$T = \langle \Psi_f \, | H | \, \Psi_i \rangle \ , \tag{1.1}$$

where Ψ_i and Ψ_f are the initial and final state wavefunctions, respectively, and H is the interaction Hamiltonian that describes the transition. For a pure nucleon-nucleon reaction, the Hamiltonian is defined by the strong interaction potential. Because the exact nature of the strong interaction is complicated and not yet fully known, there are many different models for the potentials used to describe it that have varying degrees of success in fitting different data sets. The predictions of a particular calculation will therefore depend on the nucleon-nucleon potential chosen.

The interaction between a nucleus and a photon, however, is described by the well-understood electromagnetic operator, which is given by

$$H = -\frac{1}{c} \int \vec{J}(\vec{r}) \cdot \vec{A}(\vec{r}) d\vec{r} \, , \tag{1.2}$$

where $\vec{J}$ is the nuclear current density, $\vec{A}$ is the vector potential in the radiation gauge, and $\vec{r}$ is the relative position of the particles. This operator can be expanded in terms of electric and magnetic multipoles, with different multipoles being associated with the possible angular momentum states allowed in the reaction. This expansion provides a convenient and well-defined way to characterize the TMEs corresponding to a given set of quantum numbers. This makes photonuclear reactions an excellent tool for determining nuclear quantum numbers and wave functions [DeB64].

1.2 High-energy Photon Sources

In the early days of nuclear physics, a scientist wanting to induce a photonuclear reaction had to use a naturally occurring radioactive element as a source of γ-rays. The scope of possible experiments was therefore restricted by the limited γ-ray intensities possible from available sources, and by the small set of available γ-ray energies. Furthermore, since all γ-rays produced by natural sources are unpolarized, polarization effects could not easily be explored.

More recently, the most common high-energy γ-ray source for nuclear physics experiments has been bremsstrahlung radiation. By impinging a high-energy electron beam on a thin target, a spectrum of γ-rays is generated having energies ranging from zero up to the full initial energy of the electron. The relativistic energies of the electron beam cause this spectrum to be emitted in a narrow cone centered on the electron beam axis with an opening angle of $1/\gamma$, where γ is the relativistic Lorentz factor for the electrons. Although a target placed in the path of a bremsstrahlung beam is exposed to the full γ-ray spectrum, the γ-ray energy corresponding to a particular event can be determined by measuring the energy of the corresponding recoil electron. This "tagging" process is generally the limiting factor in determining the usable γ-ray flux for a given facility. A typical tagging rate is on the order of $10^4 - 10^5$ counts/MeV of resolution [Nor94].

On-axis γ-rays from a typical bremsstrahlung facility will be unpolarized if the electron beam and the target are also unpolarized. There are, however several methods for extracting polarized γ-rays from a bremsstrahlung source. For an unpolarized beam and target, high-energy γ-rays emitted off the center axis are linearly polarized in a direction perpendicular to their emission plane [Bet34]. The degree of polarization

varies with angle, and is maximized around $\theta = 1/\gamma$. Using a collimator subtending a small solid angle around this location typically obtains a degree of polarization on the order of 0.3-0.6 [Are91]. Because multiple scattering of photons in the radiator can cause unpolarized photons to be scattered through the collimator, the radiator must be made as thin as possible, reducing the beam intensity. Linearly polarized γ-rays can also be produced by impinging the electron beam on a precisely aligned crystalline target [Lut68]. Polarizations on the order of 0.5-0.7 can be obtained in this manner [Are91]. Multiple scattering in the crystal does not significantly effect polarization, so a thick radiator can be used. Finally, to produce circularly polarized γ-rays, a circularly polarized electron beam is required. Polarizations on the order of 0.8 can be obtained using this technique. A summary of the capabilities of several bremsstrahlung facilities is shown in Table 1.1.

For many experiments, the broad spectrum produced by a bremsstrahlung beam facility is adequate, and even useful. Data for a given reaction can be simultaneously acquired over a large range of the energy spectrum, with information from the tagger allowing data for a particular γ-ray energy to be isolated. For some experiments, however, the large backgrounds and energy spread from a bremsstrahlung source are undesirable. For these experiments, a more monochromatic γ-ray spectrum is required. Such a spectrum can be produced by Compton scattering laser light off of a high-energy electron beam. This technique was first suggested in [Mil63, Aru64]. The energy of the scattered photons is increased by a factor on the order of $4\gamma^2$, where γ is the Lorentz factor for the electron beam. As is the case for a bremsstrahlung beam, relativistic effects cause the γ-rays to be emitted in a narrow cone centered along the axis of electron propagation. However, the energy of a scattered photon is correlated with its scattering angle in a Compton event. This means that, rather

than having the entire γ-ray spectrum projected more or less uniformly throughout the beam, the γ-ray energy varies with scattering angle, with the highest energy γ-rays being projected along the beam axis, and lower energy γ-rays being scattered at larger angles. The energy resolution of the γ-ray spectrum can therefore be defined by placing a small collimator along the beam path. The resulting kinematic restriction on possible γ-ray energies is usually combined with electron tagging to determine photon energy information for a given event.

To a very high degree, the polarization of a scattered photon is identical to the polarization of the incident laser light. Because a laser can be put in any polarization state with little difficulty, the polarization properties of a γ-ray beam generated in this manner are extremely flexible and readily changed during the course of an experiment. Linear and circular polarizations of a degree very close to 1.0 can be produced using this technique (see Section 2.3.3). The capabilities of several existing and planned Compton γ-ray sources are listed in Table 1.1.

1.3 Properties and Capabilities of HIGS Facility

The High-Intensity Gamma-ray Source (HIGS) at the Duke Free-Electron Laser Laboratory (DFELL) generates γ-rays via the Compton scattering technique described above. Most of the presently operating systems using this technique use an external laser as a photon source. In the HIGS facility, however, the Compton scattering occurs inside the optical cavity of a storage ring free-electron laser. This is desirable because the intracavity photon intensity is larger than extracavity intensity by a factor of Q, where Q is the quality factor of the cavity [Q=(stored energy)/(outcoupled energy per pass+losses per pass)]. The resulting γ-ray flux will

Facility	Type	Polarization	Degree	E_γ^{max} [MeV]	ΔE_γ [MeV]	Flux [kHz/MeV]
Mainz	Brem.	Linear	0.4	400	2.0	50
		Circular	0.8	840	2.0	50
Bonn	Brem.	Linear	0.4	1200	10.0	10
		Circular	0.8	2400	10.0	5
CEBAF	Brem.	Linear	0.4	1800	10.0	50
		Circular	0.8	6000	20.0	2
LEGS	Compton	Both	1.0	333	5.0	33
GRAAL	Compton	Both	1.0	1800	15.0	6
ROKK	Compton	Both	1.0	1400		1
DFELL-TUNL	Compton	Linear	1.0	225	0.8	10000
UVSOR†	Compton	Both				
Super-ACO†	Compton	Linear				

Table 1.1: Comparison of present and planned γ-ray facilities. Parameters may vary with operating energy. The listed parameters correspond to the highest photon energy possible. The information in this table was taken from [Nor94]. †The UVSOR and Super-ACO facilities have performed initial measurements at 25.2 and 33.2 MeV respectively. No facility projections have been published.

increase by the same factor. For the DFELL facility, Q can have a value of several hundred at the wavelengths of interest. This extra factor, together with the high photon intensities achievable with a free-electron laser, allow the HIGS facility to produce γ-rays at fluxes three orders of magnitude higher than existing sources.

The wide range of tunability of a free-electron laser gives a similar range of tunability for the outgoing γ-rays, which have an energy proportional to the FEL photon energy and the square of the electron energy. At the HIGS facility, this allows the peak γ-ray energy to be tuned from 2 to 200 MeV. The lower limit of possible energy resolution for a Compton scattered γ-ray beam is usually defined by the energy and momentum spread of the electron beam. The high-quality of the electron beam in the DFELL storage ring will produce γ-ray energy resolutions approaching $\Delta E/E = 0.1\%$. The momentum spread in the DFELL storage ring is

sufficiently small that the above energy resolutions can be achieved by collimation alone, eliminating the need for tagging the electron beam.

A free-electron laser generates light by inducing electron oscillations in an alternating magnetic field region called a wiggler. The direction of these oscillations define the direction of polarization of the laser light. The DFELL currently operates with an optical klystron consisting of two planar wigglers producing only one direction of linear polarization, causing all γ-rays to exhibit the same polarization. The use of optics to rotate the FEL photon polarization and the planned installation of a helical undulator will allow γ-ray beams to be produced with 100% linear polarization in the x or y directions, and 100% circular polarization with left- or right-handed helicity.

The capabilities of the HIGS facility are compared with those of several other γ-ray facilities in Table 1.1. A more detailed discussion of the properties of the HIGS facility will be given in Section 2.3.

1.4 Possible HIGS Experiments

The high intensity and energy range of the HIGS facility will allow many previously unviable experiments to be performed, making important and unique contributions to many subfields of nuclear physics. The range of experiments includes, but is by no means limited to, low-energy measurements of astrophysically relevant nuclear reactions, intermediate-energy tests of fundamental sum rules, and high-energy studies of Chiral Perturbation Theory near pion-production threshold. Examples of a few of the proposed measurements are discussed below.

At low energies ($E_\gamma < 10$ MeV), the HIGS facility will be able to measure cross sections of astrophysical relevance. Direct observation of stellar and astrophysical

processes is often impossible, making our understanding of these processes dependent on laboratory measurements of the relevant reactions. Many of these reactions are radiative capture reactions, in which two nuclei or nucleons are fused into a single nucleus, releasing energy in the form of a γ-ray. In a star, these reactions typically occur at low energies where cross sections are small enough to make direct laboratory measurements impossible. One such reaction is $^{12}\mathrm{C}(\alpha,\gamma)^{16}\mathrm{O}$, which occurs during the helium burning phase of a red giant star. This reaction is responsible for the majority of the $^{12}\mathrm{C}$ present in the universe [Kra88]. At the most effective energy for helium burning, $E_\alpha = 300$ keV, the $^{12}\mathrm{C}(\alpha,\gamma)^{16}\mathrm{O}$ cross section is approximately 10^{-8} nbarns. This reaction can not be studied directly, but must be extrapolated from measurements made at $E_\alpha = 1.2$ MeV or higher, leading to considerable uncertainties [Ji90]. Gamma-rays from the HIGS facility can be used to study the inverse reaction, $^{16}\mathrm{O}(\vec{\gamma},\alpha)^{12}\mathrm{C}$, and reduce the uncertainties of the extrapolation considerably.

At intermediate energies ($E_\gamma \sim 80$ MeV), γ-rays from the HIGS facility can begin to probe the internal structure of the nucleons. In particular, the cross section for the Compton scattering of γ-rays off the proton becomes dependent on the electric (α) and magnetic (β) polarizabilities of the proton. In a non-relativistic picture, the polarizabilities are constants describing the ability of an external electric (magnetic) field to induce a dipole moment in the proton such that $\vec{p} = \alpha\vec{E}$ (or $\vec{m} = \beta\vec{B}$). Previous experiments have determined these constants by Compton scattering unpolarized γ-rays from liquid hydrogen targets [Mac95]. Because the unpolarized Compton cross section can only be expressed in terms of the difference or sum of the polarizabilities, the numerical determination of α and β has relied on model-specific sum rules. The Compton scattering cross section for polarized γ-rays can be used to determine α and β independently. Polarized γ-rays from the HIGS facility can therefore be used to

determine the polarizabilities in a model-independent manner. Simulations predict that the present uncertainties can be reduced by an order of magnitude in two weeks of data taking, assuming only modest beam parameters [L'v90].

Operating at high energies ($E_\gamma > 140$ MeV), the HIGS facility can be used to perform experiments studying the carriers of the strong force, the π^0 and $\pi^\pm$ mesons. Of particular interest are tests of the predictive power of Chiral Perturbation Theory (ChPT), a low energy (below 500 MeV) manifestation of Quantum Chromodynamics (QCD), which, despite having no direct solution for the nucleus, is currently the most fundamental theory of the nuclear strong force. ChPT will be further described in Section 4.2. The HIGS facility is uniquely positioned to resolve several discrepancies between the predictions of ChPT and earlier experimental results. One such discrepancy lies in the E2 transition matrix element associated with the $p(\gamma,\pi^0)p$ reaction. Figure 1.1 shows the discrepancy between the photon asymmetry predicted by ChPT and experimental values deduced from unpolarized data. Assuming modest beam parameters, this discrepancy could be resolved to within 5% statistical accuracy with only 84 hours of beam time.

1.5 $^2\mathrm{H}(\vec{\gamma},\mathrm{n})\mathrm{p}$

The first nuclear physics experiment performed at HIGS was a near-threshold measurement of the analyzing power for the $^2\mathrm{H}(\vec{\gamma},\mathrm{n})\mathrm{p}$ reaction. This reaction was chosen as the initial measurement for several reasons: a relatively high cross-section ($\sigma_{tot} \sim 1.5$ mb around E_γ=3.0 MeV), the allowable energies and fluxes of the initial operating range of the HIGS facility, the immediate relevance of the measurement to important problems in big-bang nucleosynthesis, and interest on the part of both

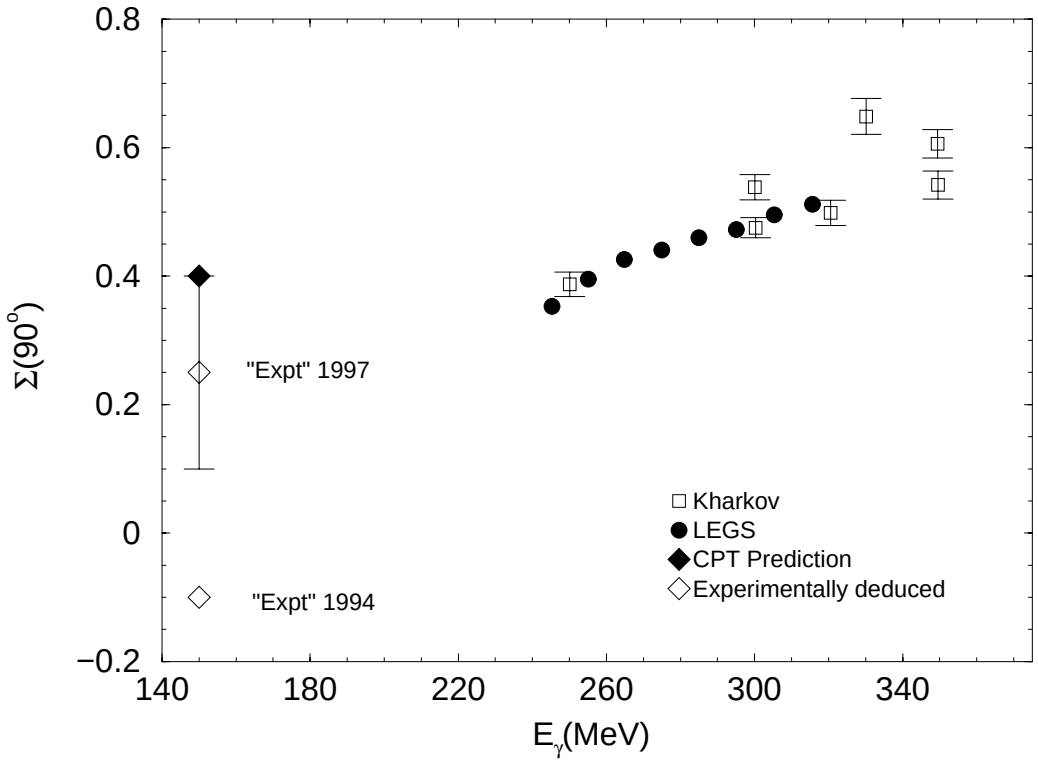

Figure 1.1: Analyzing power for the $p(\vec{\gamma}, \pi^o)p$ reaction. The data, ChPT predictions, and experimentally deduced values are taken from [Fuc96, Ber94, Ber97].

potential model and effective field theorists.

1.5.1 Motivation

The field of photonuclear physics began in 1934 when Chadwick and Goldhaber studied the breakup of the deuteron using photons from a ThC" source [Cha34]. Since then, deuteron photodisintegration, and its reverse process n-p radiative capture, have been among the most thoroughly studied reactions in nuclear physics. Because the deuteron is a two-body system, an exact solution of the Schrödinger equation is possible for both bound and scattering states. This makes the deuteron a useful system in which to study many interesting nuclear properties, including the nucleon-

nucleon interaction. The effects of meson-exchange currents, for example, were first revealed by trying to understand precision measurements of the n-p capture cross section for thermal neutrons [Ris72].

Due to the comparative availability of neutron beams over photon beams, the majority of the studies of this system have focused on n-p capture, rather than on photodisintegration. Numerous previous experiments over a wide range of energies are documented in [Are91]. One energy regime that has not received a great deal of experimental attention is the region in which the incident neutron has a center of mass energy of a few hundred keV. In this energy region, the cross section is dominated by approximately equal E1 and M1 amplitudes, as shown in Figure 1.2.

Measurements in this energy regime are experimentally difficult because neutrons having energies of a few hundred keV thermalize very easily. The thermal neutron capture cross section is approximately 10^3 times higher than that for keV neutrons, so any n-p capture experiment performed in this region will experience very high backgrounds. N-p capture cross section information is therefore most easily obtained by measuring photodisintegration cross sections. The triangle data points shown in Figure 1.2 are based on photodisintegration measurements made with γ-rays between 2.51 and 2.75 MeV, corresponding to neutron energies of 550 and 1080 keV, respectively [Bis50]. Virtually all other photodisintegration experiments have taken place at much higher energies, utilizing accelerator based γ-ray sources like those discussed in Section 1.2. Because the available data does not clearly define the cross section in this region, further measurements are warranted.

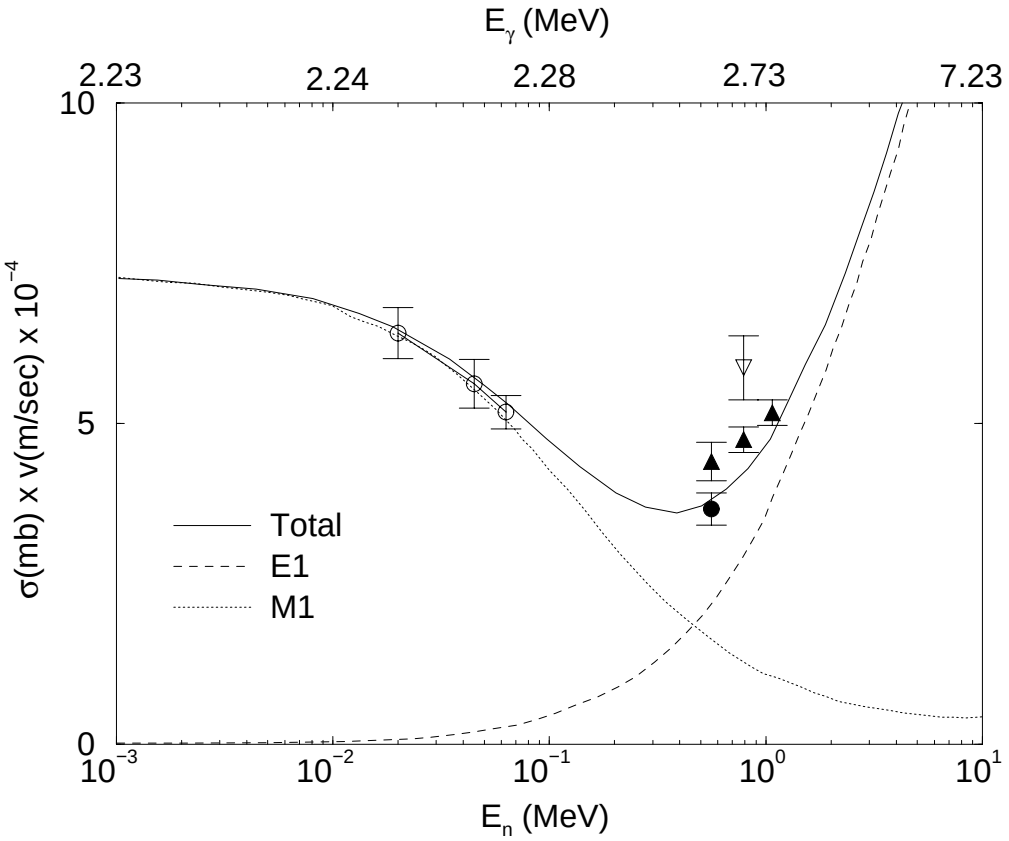

Figure 1.2: Relative E1 and M1 contributions to the n-p capture cross section. The lower energy scale is incident neutron energy in the laboratory frame. The upper energy scale is the photon energy in the corresponding photodisintegration reaction. Figure taken from [Nag97].

1.5.2 Big-Bang Nucleosynthesis

All the galaxies and solar systems in the universe are presumed to be built out of materials formed during the period immediately following the big bang. According to this theory, the universe started from a singularity with essentially infinite temperature and density, then expanded and cooled with a characteristic temperature that varied with time according to [Kra88]

$$T = \frac{1.5 \times 10^{10}}{t^{1/2}} \ , \tag{1.3}$$

where T is the temperature in Kelvin and t is the age of the universe in seconds. For times $t < 10^{-6}$ sec, photons from blackbody radiation had sufficient energy to create particle-antiparticle pairs of leptons, nucleons, and heavier particles. Charge-Parity violating decays of heavy particles led to a slight imbalance of matter over antimatter, so that when the temperature dropped below the point where nucleonic pair creation could occur, the antimatter annihilated with an equal amount of matter, leaving a quantity of residual matter nucleons. All the heavy nuclei present in the universe were built out of these residual nucleons.

In order to produce heavy nuclei, the first reaction that must occur is

$$n + p \rightarrow d + \gamma \ . \tag{1.4}$$

This first step is necessary because the negligible probability of three nucleons interacting simultaneously prevents the direct formation of heavy nuclei from the residual nucleons. Once deuterium nuclei are created, heavier nuclei can be formed by reactions such as

$$\begin{aligned} d + n &\rightarrow {}^{3}\mathrm{H} + \gamma \ , \\ d + p &\rightarrow {}^{3}\mathrm{He} + \gamma \ , \\ {}^{3}\mathrm{He} + n &\rightarrow {}^{4}\mathrm{He} + \gamma \ , \\ {}^{3}\mathrm{H} + {}^{4}\mathrm{He} &\rightarrow {}^{7}\mathrm{Li} + \gamma \ , \end{aligned} \tag{1.5}$$

and others. Because the Coulomb barrier for reactions forming heavier nuclei gets larger with increasing atomic number, the probability of forming nuclei heavier than ^{7}Li becomes very small. Most of the remaining heavier elements present in the universe were formed much later out of lighter elements during various phases of stellar evolution.

Because the n-p capture reaction is responsible for producing all the deuterium in the early universe, a detailed knowledge of the $p(n, \gamma)$ cross section is necessary

for determining the relative yields of all the primordial light elements [Nag97]. The energy range for which this reaction is most relevant for big-bang nucleosynthesis is determined by the ambient temperature at which the process occurred, and is calculated to be between 25 and 200 keV [Bur99]. As is shown in Figure 1.2, the previous measurements near this region do not adequately determine the cross section. Recent theoretical calculations [Bur99, Che99b] have found that the experimental uncertainty in the $p(n,\gamma)$ cross section is the dominant uncertainty in the calculation of these predictions.

1.5.3 HIGS Contribution

The flexibility of the HIGS facility allows two different approaches for determining the ^{2}H($\vec{\gamma}$,n)p cross section. The first and most straightforward approach would be to tune the γ-ray beam through the relevant energy region and directly measure the photodisintegration cross section. This cross section is related to the n-p capture cross section through the principle of detailed balance, which states that the reactions $N_A(\gamma,n)N_{A-1}$ and $N_{A-1}(n,\gamma)N_A$ can be expressed [Hay70]

$$\sigma(\gamma,n) = \frac{(2I_{A-1}+1)}{(2I_A+1)}\frac{A-1}{A}\frac{(E_e-T)}{E_e^2}2Mc^2\sigma(n,\gamma), \tag{1.6}$$

where N_A is a nucleus with atomic mass A, I_A is the total angular momentum of the nucleus with atomic mass A, T is the binding energy of the neutron in N_A, and E_e is the excitation energy defined as

$$E_e = \frac{A-1}{A}E_n + T\ . \tag{1.7}$$

An absolute cross section measurement requires a complete understanding of all experimental variables. A high γ-ray flux is necessary both to give a low statistical

uncertainty and to allow an experimental apparatus with a low systematic uncertainty. To operate in the energy region relevant to BBN calculations, the detector efficiencies must also be carefully understood in an energy region in which they are not often used. A program to increase the HIGS γ-ray flux and develop an experimental apparatus for an absolute cross section measurement of $^2\mathrm{H}(\vec{\gamma},\mathrm{n})\mathrm{p}$ is currently underway.

A second method of measuring the $^2\mathrm{H}(\vec{\gamma},\mathrm{n})\mathrm{p}$ cross section is to determine the photoelectric and photomagnetic contributions to the cross section. As shown in Figure 1.2, the cross section is dominated by an E1 amplitude and an M1 amplitude in the relevant region. The shape of the cross section can be expressed in terms of the electric and magnetic contributions as [Are91]

$$\sigma(\theta) \propto a + b \sin^2\theta \ , \tag{1.8}$$

where a represents the strength of the spherically symmetric (isotropic) magnetic contribution and b represents the strength of the electric dipole contribution. Several previous measurements, listed in [Are91], have attempted to extract the relative electric and magnetic amplitudes by measuring an angular distribution of outgoing protons and neutrons. The angular distribution is most sensitive to the isotropic (magnetic) term near 0° and 180°. Because these angles are difficult to measure accurately due to possible interactions between the detectors and the incident beam, these early results have large systematic errors.

The E1 and M1 amplitudes can also be extracted by observing polarization effects. Because the γ-rays from the HIGS facility are 100% linearly polarized, the shape of the $^2\mathrm{H}(\vec{\gamma},\mathrm{n})\mathrm{p}$ cross section will have an azimuthal dependence. This shape, as will be

derived in Section 4.3.1, can be expressed as

$$\sigma(\theta, \phi) \propto a + b \sin^2 \theta \left[1 + \cos 2\phi\right] \ , \tag{1.9}$$

where ϕ is the azimuthal angle with respect to the direction of γ-ray polarization. By measuring the analyzing power, defined as

$$\Sigma(\theta) = \frac{\sigma(\theta, 0^\circ) - \sigma(\theta, 90^\circ)}{\sigma(\theta, 0^\circ) + \sigma(\theta, 90^\circ)} = \frac{b \sin^2 \theta}{a + b \sin^2 \theta} \ , \tag{1.10}$$

the relative E1 and M1 contributions to the cross section can be determined at any angle. Since the value for $\Sigma(\theta)$ would be exactly 1.0 for the case of pure E1 absorption (a=0), any measured deviation from this value provides a measurement of the M1 contribution.

Measuring the relative E1 and M1 contributions to the cross section in this manner avoids the systematic uncertainties of absolute cross section measurements and angular distribution measurements of ^{2}H($\vec{\gamma}$, n)p. This dissertation reports the first such measurement made at the HIGS facility as part of a larger program to determine the cross section and electromagnetic properties of the deuteron in this understudied energy region.

Chapter 2

Gamma-ray Production: Theory

The production of γ-rays via the intracavity Compton scattering of laser photons in a storage ring FEL was first suggested by A. Sandorfi as a possible upgrade to the LEGS facility [San83]. The DFELL/TUNL High-Intensity Gamma-ray Source (HIGS), proposed by V. N. Litvinenko in 1993, represents the first implementation of this technique. The properties of the Duke facility give HIGS many capabilities useful for nuclear physics research

2.1 Duke Free-Electron Laser Laboratory

2.1.1 Principles of FEL operation

Theoretical development of the free-electron laser (FEL) began in 1971 at Stanford University by J. M. J. Madey [Mad71]. An FEL produces a high-power tunable laser beam that has all the coherence and monochromatic properties of a conventional

laser. However, where a conventional laser gains optical power by de-exciting a discrete energy state in an atom or molecule, an FEL gains optical power by decelerating relativistic free electrons in an electromagnetic field.

In its most basic form, an FEL consists of three components: an electron source, a magnetic undulator, and an optical cavity. The electron source injects short pulses of electrons into the FEL system. These electrons pass through an undulator, sometimes called a wiggler. An undulator is a region of alternating magnetic fields that causes the electrons to "wiggle" back and forth as they pass through the magnetic fields. This acceleration of the charged particles causes them to radiate some of their energy away in the form of photons. Because the "wiggle" is periodic, some wavelengths of emitted photons will constructively interfere with each other, causing a certain range of wavelengths to be amplified in the resulting optical field. This range of wavelengths is dependent on the undulator and electron beam parameters. The interaction between the electrons and the resulting photon pulses can cause new photons to be added coherently to the optical field.

2.1.2 The Duke Free-Electron Laser

The Duke Free-Electron Laser Laboratory (DFELL) is a 52,000 square foot facility housing two operational FELs. The first commissioned laser in the facility is the Mark III IR FEL, which consists of a 45 MeV linear accelerator and a permanent magnetic undulator. A more recent commissioning placed an optical klystron in an electron storage ring. This FEL is designed to operate at high power and produce photons from 2-12 eV (103-620 nm. Wavelength=(1240 eV nm)/photon energy). This range of tunability, as well as the advantageous properties of the electron beam in the storage ring, make the storage ring free-electron laser ideal for use in γ-ray

production. A schematic of the DFELL facility is shown in Figure 2.1.

Linear Accelerator

The electrons for the FEL are provided by a linear accelerator. The linac consists of eleven sections of the former SLAC Mark III accelerator, three klystrons, and a photoinjector. An N_2 laser fires a pulsed beam on to a heated photocathode, causing narrow pulses of electrons to be ejected via the photoelectric effect. These electron packets are accelerated in a series of radio-frequency (RF) cavities until reaching energies between 240-280 MeV. The linac is capable of injecting 1.1×10^{10} electrons/sec into the storage ring.

Storage Ring

The electrons from the linac are injected into a storage ring. The storage ring has a race-track configuration consisting of two 34 m straight sections and two curved sections with a 6.2 m radius of curvature. Electrons from the linac enter the storage ring through a chicane on the north straight section. The electrons are kept in the storage ring by a series of 64 quadrupole and 40 dipole magnets. The quadrupole magnets form a focusing-defocusing (FODO) lattice, which alternately direct the beam towards and away from the center axis of the storage ring [Wu93]. The dipole magnets are arranged on the curved sections of the storage ring. Each dipole bends the electron beam path with a radius of curvature of $\sim$ 2 m. The dipole magnets are designed to contain electron beams with energies up to 1.2 GeV. These electron beams circulate in the ring with a revolution frequency of 2.79 MHz.

Electrons in the storage ring will slowly lose energy through synchrotron radiation. This energy is replaced by an RF cavity placed on the north straight section.

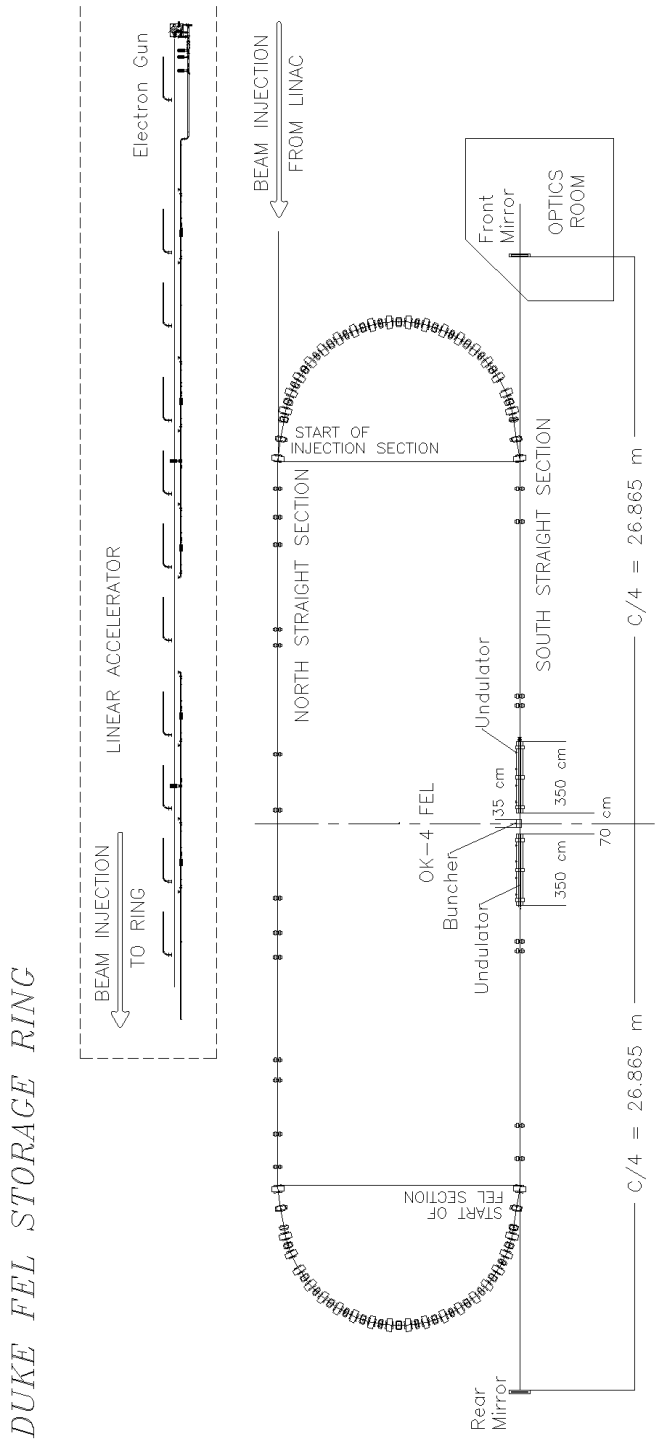

Figure 2.1: Layout of the Duke Free-Electron Laser Laboratory. Figure taken from [Lit95].

The cavity operates at 178.547 MHz. The current RF system is capable of correcting energy fluctuations of up to 3% of the initial energy (e.g. a 1.0 GeV electron that lost up to 30 MeV could be brought back to 1.0 GeV by the RF system) [Wu93]. The RF system is also able to gradually add energy to all electrons in the storage ring. This allows electron bunches injected into the storage ring at 280 MeV by the linac to be slowly accelerated, or "ramped", up to 1.1 GeV. This injection and ramping process lasts approximately 10-20 minutes per injection, with the electron beam generally lasting several hours before needing to be replenished.

OK-4 FEL

The FEL photons are generated when electron bunches in the storage ring pass through the Optical Klystron-4 (OK-4) [Lit93], placed on the south (right hand side of Figure 2.1) straight section of the storage ring. The OK-4 is 7.4 m long and consists of a series of electromagnets in two planar wigglers arranged to create alternating magnetic fields with a 10 cm period. The two planar wigglers are separated by a single-period bunching section (sometimes called a dispersion section) that temporarily deflects the electron bunch out of the optical field. A general schematic of the OK-4 is shown in Figure 2.2.

The wavelength of the photons generated in the OK-4 can be calculated by considering the wiggler sections as seen by the electron. In the electron rest frame, a wiggler appears to be a transverse magnetic field approaching the electron with a velocity approximately equal to c, where c is the speed of light. The magnetic field amplitude is given by $\gamma B_{\perp}$. The electron also sees a transverse electric field of amplitude $\sim c\gamma B_{\perp}$ perpendicular to the magnetic field [Jac75]. A transverse field of perpendicular electric and magnetic fields traveling with a velocity $\sim c$ appears as

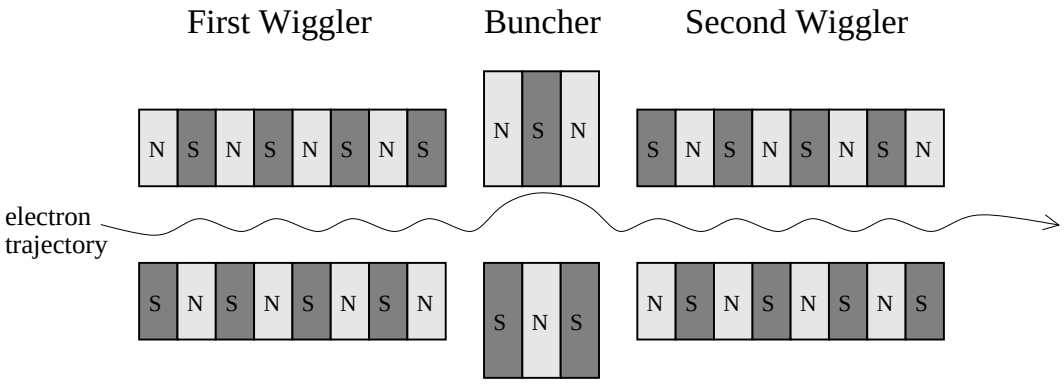

Figure 2.2: General schematic of the OK-4. Note that the direction of the electron "wiggle" is in and out of the page.

a photon, so the undulator can be treated as a virtual photon field in the electron rest frame. In the ideal case, the wavelength of the virtual photons is determined by relativistic length contraction, and given by $\lambda' = \lambda_w/\gamma$, where λ_w is the length of one wiggler period, and γ is the relativistic Lorentz factor for the electrons.

These virtual photons can then scatter off the electrons. Because the photon energies are so much less than the electron rest mass (typically a few mev), recoil is negligible, and the photons scatter without losing significant amounts of energy. These photons are Doppler shifted back into the lab frame, where they have a wavelength of $\lambda_o = \gamma\lambda'(1 - \beta_z \cos\theta) \approx \lambda_w/2\gamma^2$. This approximation is not completely correct, because β_z is less in the undulator than it is outside the undulator. This is because some portion of the longitudinal velocity is lost to the "wiggling" motion of the electrons. Accounting for this loss in longitudinal velocity, the wavelength of the generated FEL photons is given by

$$\lambda_o = \frac{\lambda_w}{2\gamma^2}\left[1 + \left(\frac{\lambda_w e B_\perp}{2\pi m_e c^2}\right)^2\right] = \frac{\lambda_w}{2\gamma^2}\left[1 + \frac{K_w^2}{2}\right]. \tag{2.1}$$

Equation 2.1 is known as the FEL equation, where e is the electron charge, $B_\perp$ is the magnetic field strength, and $m_e c^2$ is the mass of the electron in MeV [Mar85]. K_w^2

is a dimensionless parameter called the wiggler parameter. The wiggler parameter of the OK-4 can be varied between 0 and 5.42 [Lit93].

Equation 2.1 defines the central wavelength of the light emitted from the OK-4. If the wiggler sections were infinite in length, then the power spectrum would be a delta function centered at this wavelength. The actual power spectrum can be obtained by applying a Fourier transform over the length of the OK-4. For a single wiggler section, this becomes

$$E(\omega) = \frac{1}{\sqrt{2\pi}} \int_0^{N_w \lambda_o / c} E_o e^{i(\omega - \omega_o)t} dt \propto \frac{N_w}{\omega_o} \frac{\sin\left[\frac{N_w \pi(\omega - \omega_o)}{\omega_o}\right]}{\frac{N_w \pi(\omega - \omega_o)}{\omega_o}}, \tag{2.2}$$

where the actual power spectrum is given by $I(\omega) \propto |E(\omega)|^2$. This would produce the power spectrum shown in Figure 2.3. The presence of the buncher between the two wiggler sections adds a fine structure to this shape. A typical spontaneous radiation spectrum from the OK-4 is shown in Figure 2.4.

In the small-signal and low-gain regime, the single-pass gain of an FEL is proportional to the derivative of the spontaneous emission spectrum with respect to energy [Bra90]. A typical gain curve corresponding to the spontaneous spectrum shown in Figure 2.4 is given in Figure 2.5. This gain structure causes photons of some wavelength to be amplified more than the others. The intensity of photons at this favored wavelength will grow exponentially until, after many cycles, the intensity at other wavelengths is negligible by comparison. The linewidth of the resulting photon pulse becomes increasingly narrow as the center wavelength is continually amplified. The linewidth can decrease down to the Fourier limit, which is determined by a variety of beam parameters. For typical operating conditions, the linewidth of the photon pulses from the OK-4 is $\Delta\lambda/\lambda = (1-4) \times 10^{-4}$, although more narrow linewidths are possible under special beam conditions [Par00].

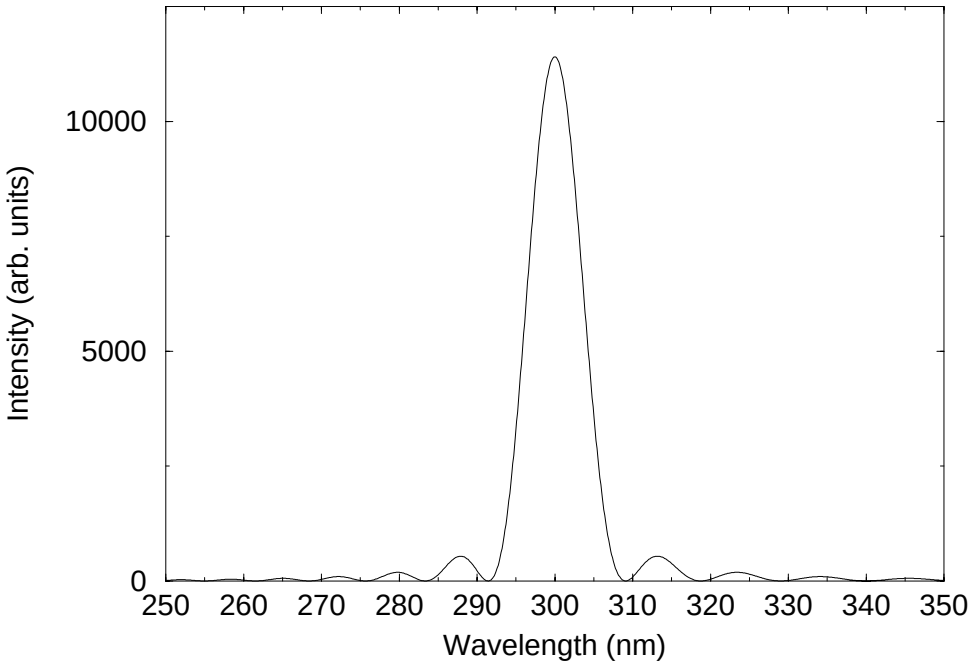

Figure 2.3: Spontaneous emission spectrum for a planar wiggler with a resonant wavelength of 300 nm. This spectrum corresponds to a wiggler with N_w=34.

The coherence of the OK-4 FEL light results from a longitudinal bunching effect within the electron beam. As electrons enter the OK-4, they are spread evenly throughout the bunch. Photons emitted by such an electron bunch are out of phase with each other, resulting in incoherent emission. Placing an optical cavity (described below) around the OK-4 captures the photon pulses and causes them to propagate through the OK-4 repeatedly. By arranging the cavity mirrors such that the round-trip time of the photon pulses in the optical cavity is equal to the round-trip time of electron bunches around the storage ring, the photon pulses and electron bunches can be made to co-propagate through the OK-4. As the electrons pass through the first wiggler section of the OK-4 they may gain or lose energy depending on the phase between the electron motion and the optical field. The electrons experience a transverse acceleration from the electric field of the photon pulses, which, when coupled

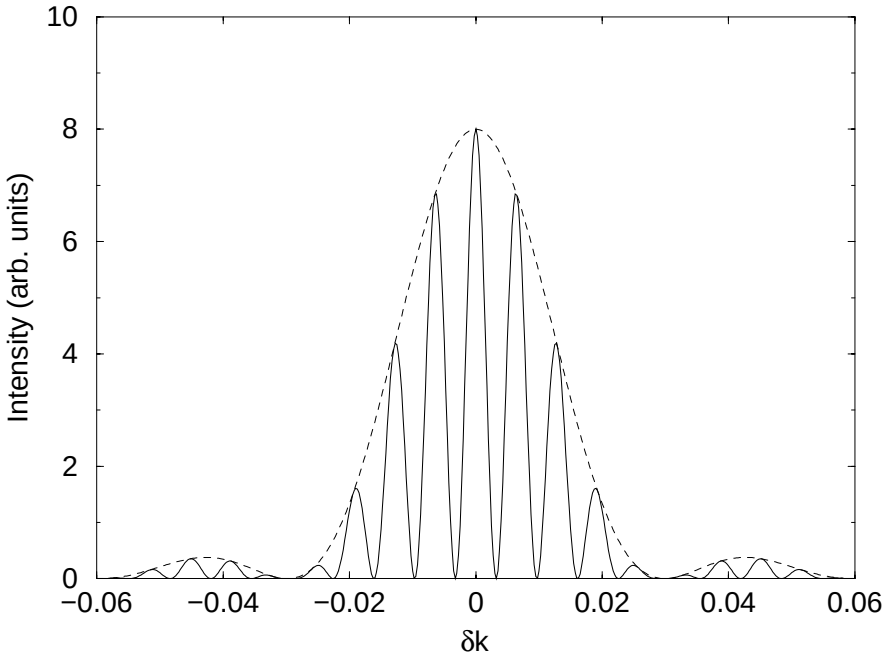

Figure 2.4: Ideal spontaneous radiation spectrum for the OK-4 FEL. δk represents deviations from the central wave number of the photon distribution (k=$2\pi/\lambda$). The dashed line represents the the spontaneous emission spectrum of a conventional FEL. Figure taken from [Par00].

with the magnetic field of wiggler, produces a net gain or loss of longitudinal velocity (this is the so called pondermotive force [Mar85]). For an idealized and infinite wiggler, this process would produce a series of small electron bunches spaced one optical wavelength apart, as shown in Figure 2.6. This coherent bunching effect would cause photons emitted by the electrons to be produced in phase with the existing optical field.

A real wiggler system can never achieve the perfect separation of small electron bunches shown in Figure 2.6. This coherent bunching effect is maximized in an optical klystron by the buncher region located between the two wiggler sections. The buncher consists of one period of deflecting magnets that bends the electron beam

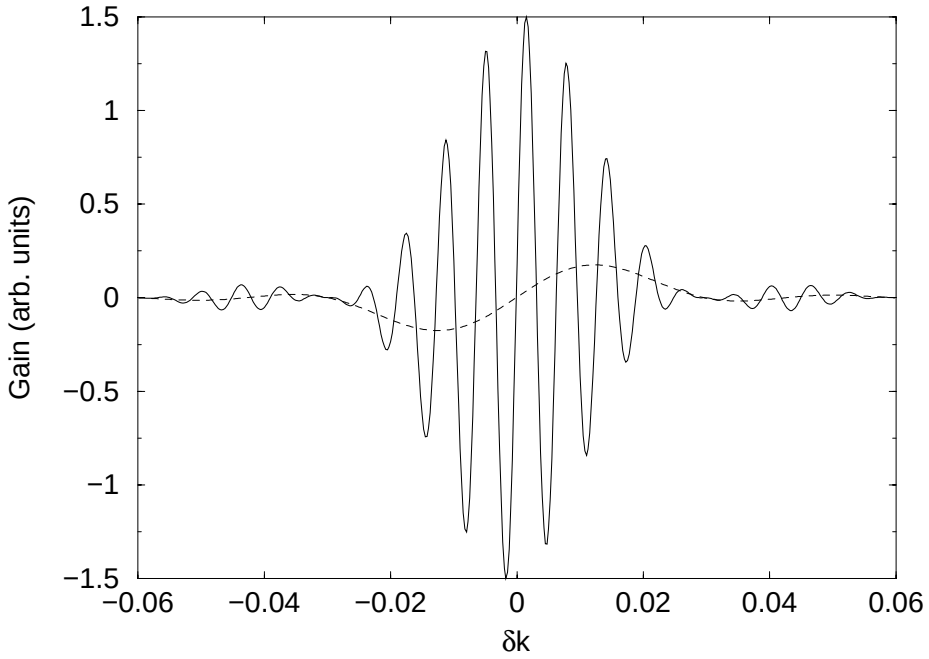

Figure 2.5: Gain spectrum for the OK-4 FEL corresponding to the spontaneous emission spectrum shown in Figure 2.4. δk represents deviations from the central wave number of the photon distribution (k=$2\pi/\lambda$). The dashed line represents the gain spectrum for a conventional FEL. Figure taken from [Par00].

significantly away from the center axis. This allows electrons of different energies to drift into the smaller bunches without further interaction with the optical field. The electrons enter the second wiggler section with a higher degree of bunching than would have otherwise been possible, leading to a higher degrees of coherence and greater amplification. This process allows optical klystrons to operate with a much higher gain than is possible for single wiggler FELs. The gain of the OK-4 FEL can be 5-10 times higher than that of a single wiggler FEL, depending on specific beam parameters [Par00].

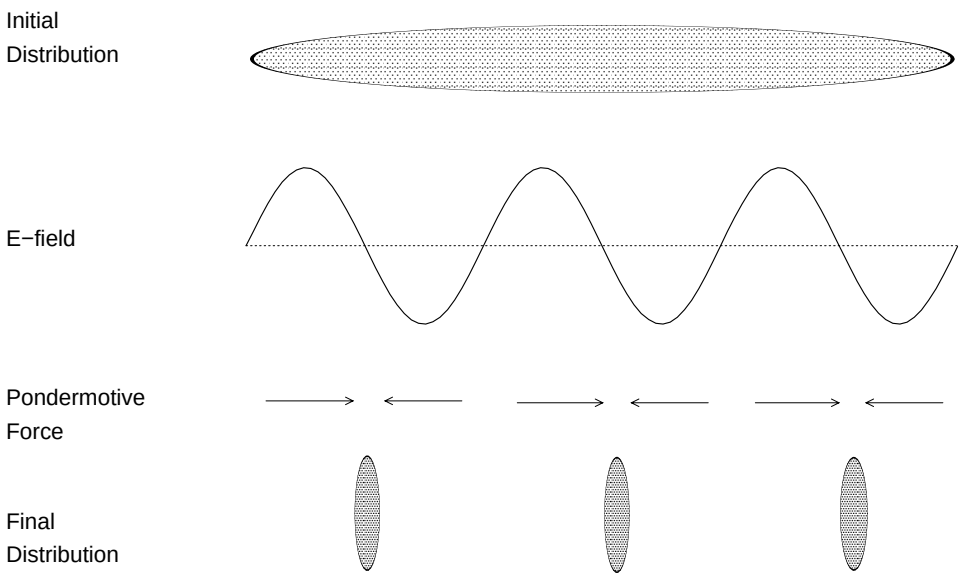

Figure 2.6: Idealized bunching of the electron distribution resulting from interaction with an FEL optical field. Real electron beam parameters prevent this degree of bunching from occurring.

Optical Cavity

The photon pulses generated in the OK-4 are projected into an optical cavity consisting of two spherical mirrors, described in [Par00] and references contained therein. The mirrors have a radius of curvature of 27.27 m and are placed 53.73 m apart. The mirrors are mounted on movable stages so that minor adjustments in position and angle can be made to maximize the overlap of the photon packet with the electron beam.

Because the OK-4 operates in an energy region where limited gain is possible, the cavity mirrors need to minimize losses in order to maintain lasing. High reflectivity is only available over a small range of wavelengths for a given set of mirrors, so different mirrors have to be installed for operation for a given wavelength range. Mirrors for operation near 225 nm, for example, are coated with MgO_2/Al_2O_3, and are highly

Electrons:	Current	up to 1.0 A
	Energy Range	230-1100 MeV
	Energy Resolution	0.0005
	Energy Acceptance	6%†
	Maximum β_x	12.92 m
	Maximum β_y	21.81 m
	Emittance*	$\sim 2 \times 10^{-8}$ m·rad
	σ_x ring	0.27 mm
	σ_x OK-4	0.5 mm
	σ_y	0.071 mm
	σ_z	33 ps
Photons:	Intracavity Flux	up to 5×10^{21} phot/sec
	Energy Range	2-12.5 eV
	Linewidth	(1-4)$\times 10^{-4}$
	Intracavity Power	10-1000 W
Storage Ring:	Vacuum	$\sim 10^{-10}$ Torr
	Revolution Frequency	2.8×10^{6} Hz

Table 2.1: DFELL Operating Parameters [Lit99]. *The emittance is a typical value only and can vary significantly.

reflective from 217-233 nm. [Par99].

2.1.3 DFELL Operating Parameters

A summary of DFELL parameters for the OK-4 laser system is shown in Table 2.1. The parameters reflect design parameters and have not all been achieved. Electron parameters β_x and β_y refer to the angular divergence of the electron beam in the x and y directions, respectively. The electron bunch size in the storage ring and the OK-4 is given by σ_x, σ_y and σ_z.

The performance of the OK-4 FEL can vary greatly depending on beam specifications. The maximum FEL intracavity power as a function of photon energy is

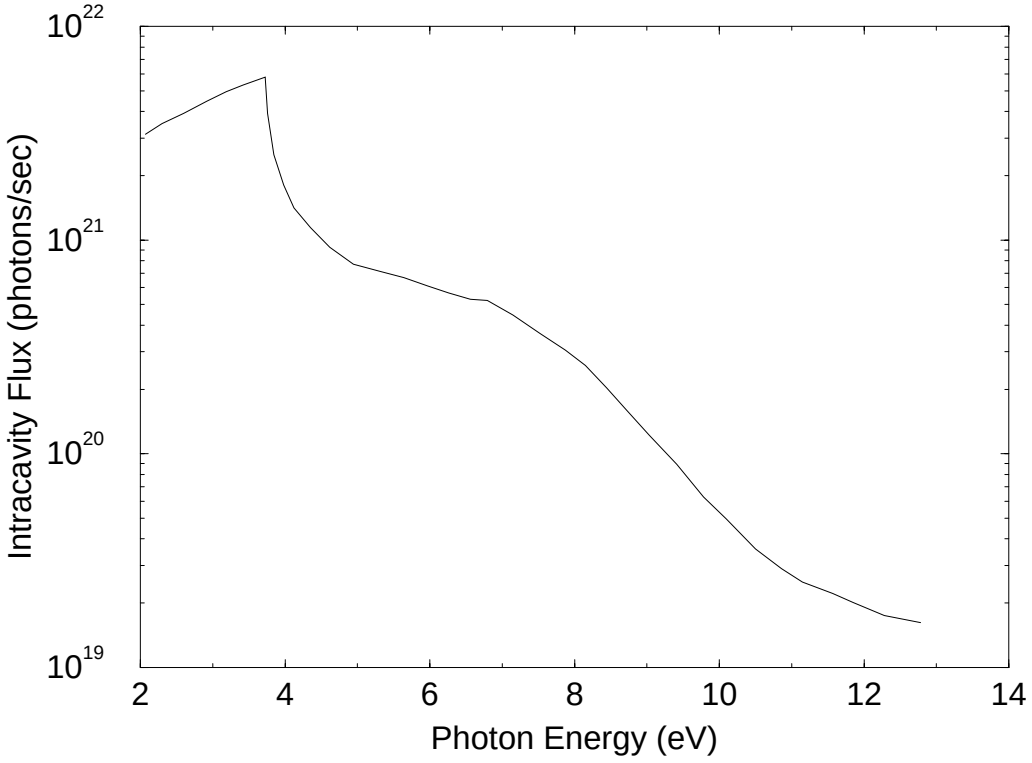

Figure 2.7: Maximum intracavity FEL flux for a given photon energy. The structure in the distribution results from the differences in the mirrors necessary to produce various photon energies. This distribution assumes 100 mA of current in the storage ring [Lit96b].

shown in Figure 2.7. This spectrum assumes a 100 mA electron bunch in the storage ring. The photon intensity in the OK-4 has been empirically determined to scale with electron current as approximately $I^{3/2}$, although this can vary for specific operating conditions and can be as large as I^2 [Par00, Lit00]. The complex structure of Figure 2.7 reflects contributions from many factors, including storage ring performance at different electron energies, and mirror availability at different wavelengths [Lit96b].

2.2 Compton Scattering

The simplest operation mode of the storage ring FEL has a single electron bunch circulating around the storage ring, allowing the electron bunch and the photon bunch it generates to co-propagate through the OK-4. The RF system is capable of maintaining up to 64 separate electron bunches in the storage ring simultaneously, allowing the injection of a second electron bunch at a position one half a ring circumference away from the first. This second electron bunch will be passing forward though the OK-4 at the same time the photon pulse from the initial electron bunch is traveling in the opposite direction in the same region. The resulting photon-electron interaction is described by Compton scattering.

2.2.1 Kinematics

The kinematics of Compton scattering can be completely described by applying the conservation of energy and momentum to the electron-photon system. Applying these conservation laws to a photon scattering off of a stationary electron gives the classical Compton scattering equation, in which the final photon energy is related to the initial energy and scattering angle by

$$E' = \frac{E}{1 + \frac{E}{m_e c^2}(1 - \cos\Theta)}, \tag{2.3}$$

where E and E' are the initial and final photon energies, $m_e c^2$ is the electron rest mass, and θ is the scattering angle with respect to the initial photon direction. In this frame, the photon always scatters with less energy than it had initially, because some of its energy is lost to electron recoil. In this frame, the electron experiences a net gain in energy, because it was initially at rest.

The kinematics for Compton scattering in any reference frame can be derived by considering the conservation of 4-momentum. The energy of the scattered photon E_γ is given by

$$E_\gamma = E_\lambda \frac{1 + \beta \cdot \cos\theta_i}{1 - \beta \cdot \cos\theta_f - E_\lambda/E_e \cdot (1 - \cos\theta_{ph})}, \tag{2.4}$$

where θ_i is the angle between the initial photon direction and the initial electron momentum, θ_f is the angle between the scattered photon and electron, and θ_{ph} is the angle between the initial and scattered photons. The electron and photon initial energies are given by E_e and E_λ, respectively, and β is the ratio of the electron velocity to the speed of light. The case most relevant for the DFELL facility is "head-to-head" scattering, in which $\theta_i = \pi$. Writing $\theta = \theta_f = \pi - \theta_{ph}$, we can reduce Equation 2.4 to

$$E_\gamma = E_\lambda \frac{1 + \beta}{1 + r - (\beta - r) \cdot \cos\theta} \tag{2.5}$$

where $r = E_\lambda/E_e$ accounts for electron recoil. In frames in which the electron and the photon make a head-to-head collision, the scattered photon energy is equal to or greater than its initial energy, because the electron loses some of its kinetic energy to recoil. If the electron energy is high enough, as is the case for the HIGS facility, the photon can gain sufficient energy to become a γ-ray. Scattering 246 nm (3.26 eV) FEL photons from 500 MeV electrons, for example, produces γ-ray energies as high as 12.2 MeV. Conservation of momentum requires that most of these photons be projected in the direction of electron propagation.

For the case $\gamma = E_e/mc^2 \gg 1$, as is always true at the DFELL facility, we can approximate the energy distribution as

$$E_\gamma \cong \frac{4\gamma^2 E_\lambda}{1 + (\gamma\theta)^2 + 4\gamma\frac{E_\lambda}{mc^2}}. \tag{2.6}$$

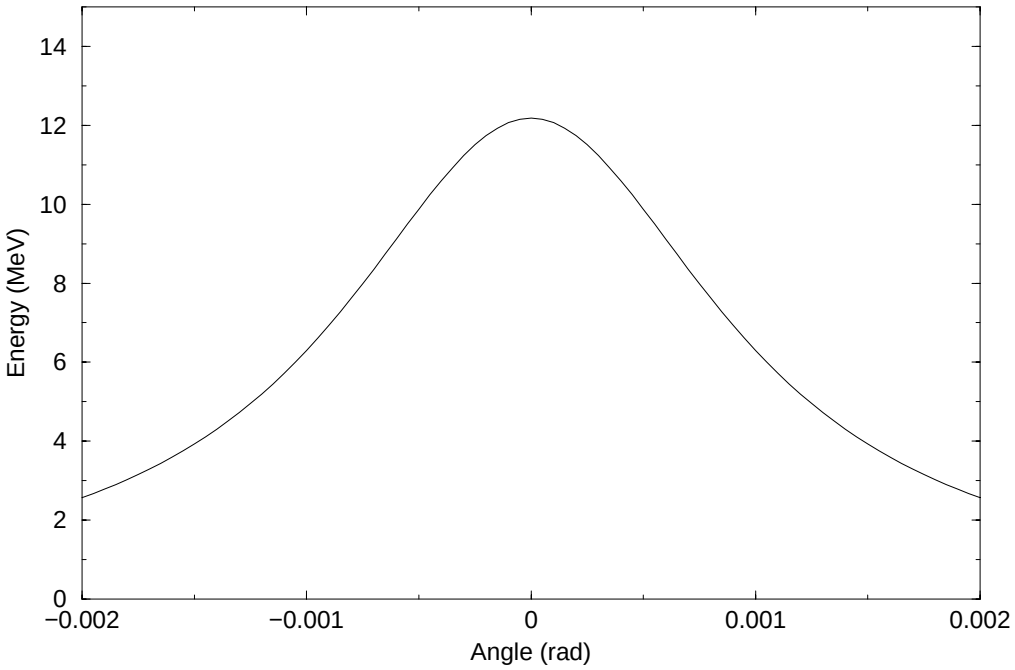

Figure 2.8: Energy-angle correlation for γ-rays generated by scattering 246 nm (3.26 eV) FEL photons off of 500 MeV electrons.

A sample energy distribution as a function of laboratory scattering angle is shown in Figure 2.8. This distribution is typical over the range of operating parameters at HIGS.

2.2.2 Scattering Cross Section

The scattering of a photon by an electron in any reference frame can be completely described by quantum electrodynamics (QED). Following [Ber71, Lit96b], we derive the scattering cross section in the laboratory frame for linearly polarized photons and unpolarized relativistic electrons. In QED, cross sections can be conveniently

expressed in terms of three kinematic invariants given by

$$\begin{aligned} s &= (p+k)^2 = (p'+k')^2 = m^2 + 2pk = m^2 + 2p'k'; \\ t &= (p-p')^2 = (k-k')^2 = 2(m^2 - pp') = -2kk'; \\ u &= (p-k')^2 = (p'-k)^2 = m^2 - 2pk' = m^2 - 2p'k; \\ s+t+u &= 2m^2, \end{aligned} \tag{2.7}$$

where p and p' are the incident and scattered momentum 4-vectors for the electron, and k and k' are the incident and scattered momentum 4-vectors for the photon. The cross section can be written generally as

$$d\sigma = \frac{1}{32\pi^2} \frac{dtd\phi}{(s-m^2)^2} |M_{fi}|^2, \tag{2.8}$$

where ϕ is the azimuthal angle and M_{fi} is the scattering amplitude for the process. The scattering amplitude is defined by the two Feynman diagrams shown in Figure 2.9. The scattering amplitude for these processes is given by

$$M_{fi} = -4\pi e^2 \epsilon'^*_\mu \epsilon'_\nu \left[\overline{u}' \left(\frac{\gamma^\mu (p+k+m) \gamma^\nu}{s-m^2} + \frac{\gamma^\nu (p-k'+m) \gamma^\mu}{u-m^2} \right) u \right], \tag{2.9}$$

where ϵ is the polarization 4-vector for the photon and u is the bispinor amplitude for the electron.

It is convenient to simplify the kinematic invariants to two variables given by

$$x = \frac{s-m^2}{m^2} \; ; \; y = \frac{m^2-u}{m^2} \tag{2.10}$$

These kinematic invariants are valid in any reference frame. In the lab frame, these expressions become:

$$x = \frac{2pk}{m^2} = \frac{2\gamma E_\lambda (1 - \beta \cos\theta_i)}{mc^2} \; ; \; y = \frac{2pk'}{m^2} = \frac{2\gamma E_\gamma (1 - \beta \cos\theta_f)}{mc^2} \tag{2.11}$$

For unpolarized photons and electrons, Equation 2.8 becomes

$$d\overline{\sigma} = \frac{8\pi r_e^2}{x^2} dy \left\{ \left(\frac{1}{x} - \frac{1}{y} \right)^2 + \left(\frac{1}{x} - \frac{1}{y} \right) + \frac{1}{4} \left(\frac{x}{y} - \frac{y}{x} \right) \right\}, \tag{2.12}$$

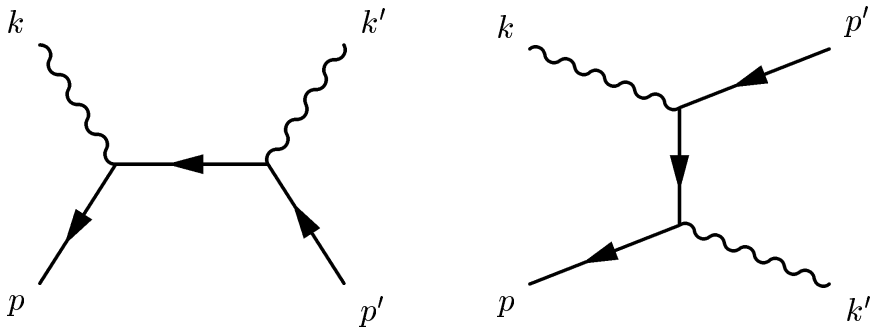

Figure 2.9: Feynman diagrams for Compton scattering. The incident and outgoing electron momenta are given by p and p', while k and k' correspond to the photon.

where we use $\mathrm{d}\overline{\sigma}$ to denote an unpolarized cross section. In the electron rest frame ($p = 0$), this expression reduces to the Klein-Nishina equation [Kle30].

$$d\overline{\sigma} = \frac{r_e^2}{2}\left(\frac{\omega'}{\omega}\right)\left\{\frac{\omega}{\omega'} + \frac{\omega'}{\omega} - \sin^2\theta\right\} d\Omega' \tag{2.13}$$

Including polarization makes the expansion of Equation 2.9 much more complicated. The cross section for unpolarized electrons and photons with arbitrary polarization becomes

$$\begin{aligned} d\sigma = \frac{d\overline{\sigma}}{2} + 2r_e^2\frac{dyd\phi}{x^2}\Bigg\{&(\xi_3 + \xi_3')\left[-\left(\frac{1}{x} - \frac{1}{y}\right)^2 - \left(\frac{1}{x} - \frac{1}{y}\right)\right] + \\ &+\xi_1\xi_1'\left(\frac{1}{x} - \frac{1}{y} + \frac{1}{2}\right) + \xi_2\xi_2'\frac{1}{4}\left(\frac{x}{y} + \frac{y}{x}\right)\left(1 + \frac{2}{x} - \frac{2}{y}\right) + \\ &+\xi_3\xi_3'\left[\left(\frac{1}{x} - \frac{1}{y}\right)^2 + \left(\frac{1}{x} - \frac{1}{y}\right) + \frac{1}{2}\right]\Bigg\}, \end{aligned} \tag{2.14}$$

where $\vec{\xi} = (\xi_1, \xi_2, \xi_3)$ and $\vec{\xi'} = (-\xi_1', -\xi_2', \xi_3')$ are the Stokes parameters for the incident and scattered photons. If we sum over the polarization of the final photons by setting $\vec{\xi'} = 0$ and doubling the remaining terms, we get an expression for the differential

cross section for γ-rays as a function of lab scattering angle as

$$d\sigma = \frac{8r_e^2}{x^2}\left\{\frac{1}{4}\left(\frac{x}{y}+\frac{y}{x}\right)+(1-\xi_3)\left[\left(\frac{1}{x}-\frac{1}{y}\right)^2+\left(\frac{1}{x}-\frac{1}{y}\right)\right]\right\}\cdot\left(\frac{E_\gamma}{mc^2}\right)^2 d\Omega', \tag{2.15}$$

where the dependence on the scattering angle is contained in the expressions for y (Equation 2.11) and E_γ (Equation 2.5). The Stokes parameter ξ_3 for the case of linearly polarized incident FEL photons is given by $\xi_3 = \cos 2\phi$. A sample distribution of Equation 2.15 is shown in Figure 2.10. If the incident FEL beam were circularly polarized, $\xi_3 = 0$, and the distribution would lose its azimuthal dependence. The differential cross section as a function of the lab scattering angle would be given by the $\phi = 45°$ case shown in Figure 2.10 for all azimuthal angles.

2.2.3 Ideal Case

The "ideal" case of Compton scattering at DFELL would involve laser light scattering off of a point source of a perfectly monoenergetic electrons with zero angular divergence. In this case, the energy-angle correlation given in Equation 2.5 and Equation 2.6 is perfectly preserved, allowing γ-rays of different energy to be separated geometrically by an experimenter. Placing a circular aperture collimator centered along the γ-ray beam axis allows the passage of a γ-ray beam with energies ranging from the maximum energy to a lower limit defined by the collimator radius. The distribution of γ-ray energies can be obtained by writing the differential cross section in terms of the electron, photon, and γ-ray energies by using the relations from Equation 2.5. The kinematic ratios x and y can be rewritten as [Lit96b]

$$x = \frac{2E_e\left(1+\beta\right)E_\lambda}{\left(m_e c^2\right)^2}; y = x\frac{\beta E_e - E_\gamma}{\beta E_e - E_\lambda}; dy = -x\frac{dE_\gamma}{\beta E_e - E_\lambda}. \tag{2.16}$$

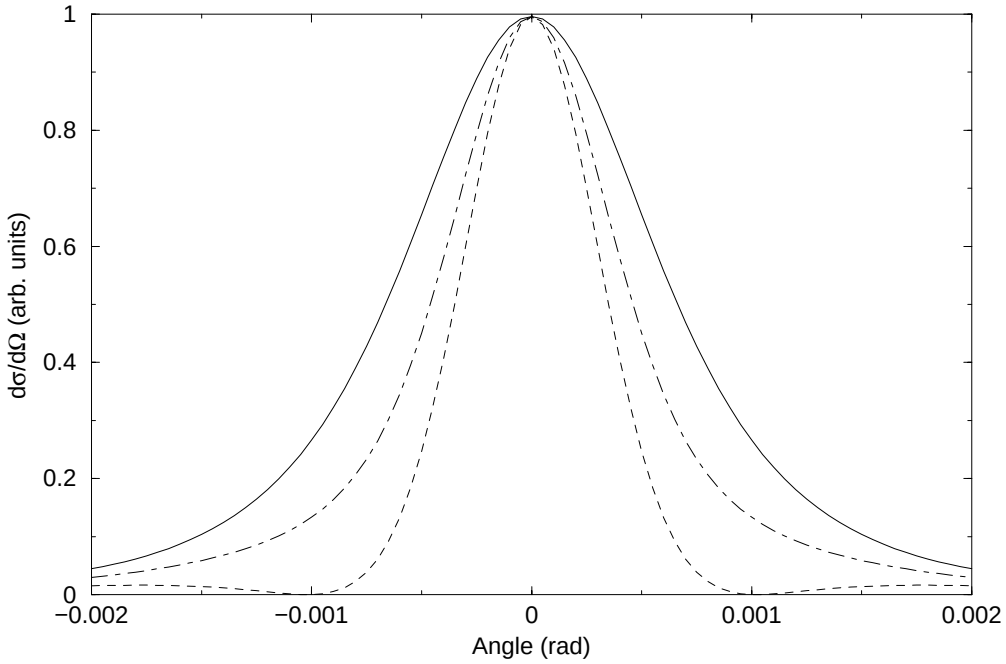

Figure 2.10: Differential cross section for 12.2 MeV γ-rays generated by scattering 3.26 eV FEL photons from 500 MeV electrons. The solid line is the cross section for an azimuthal angle $\phi = 90°$, the dot-dashed line is $\phi = 45°$, and the dotted line represents $\phi = 0°$. ϕ is defined with respect to the plane of γ-ray polarization.

Using these relations, the differential cross section from Equation 2.12 becomes

$$\frac{d\overline{\sigma}_{en}}{dE_\gamma} = \frac{8\pi r_e^2}{x}\left\{\left(\frac{1}{x}-\frac{1}{y}\right)^2 + \left(\frac{1}{x}-\frac{1}{y}\right) + \frac{1}{4}\left(\frac{x}{y}+\frac{y}{x}\right)\right\}\frac{r\,(1+\beta)}{(\beta-r)\,(1-\beta+2r)}. \tag{2.17}$$

A sample distribution is shown in Figure 2.11. The large number of low-energy γ-rays results from the increase in available solid angle for a given $d\sigma/d\Omega$ for large angles. Each energy in the above distribution corresponds to a specific divergence angle, and can be selected by a collimator of appropriate size. For example, a 5 mm diameter collimator placed 30 m from the scattering point subtends an angle of $\theta = 8.33 \times 10^{-5}$ radians from the γ-ray beam axis. This collimator would therefore block any γ-ray having an energy less than 12.10 MeV.

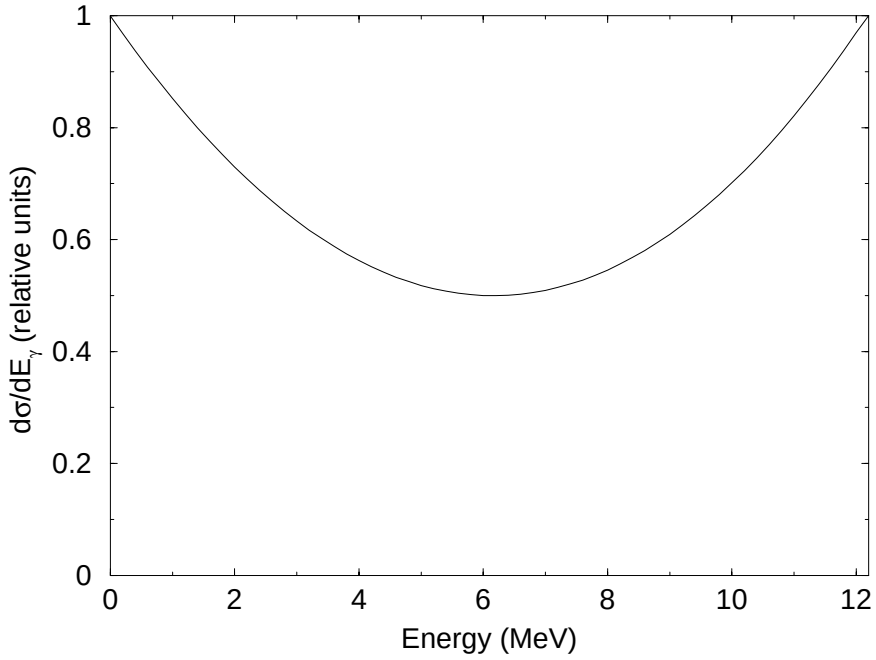

Figure 2.11: Differential γ-ray flux as a function of energy. This spectrum was generated by assuming 3.26 eV FEL photons and 500 MeV electrons.

2.3 Predictions of HIGS Performance

This section applies the theoretical treatment of a Compton backscattering γ-ray source and applies it to the specific parameters available at DFELL. This was first done by V. N. Litvinenko in 1993. Most differences between the predicted γ-ray distributions for DFELL and the ideal distributions described above are the result of the finite energy and momentum spreads in the electron beam. Rather than being a monoenergetic point source of electrons, the electrons stored in the storage ring have a distribution function given by [Lit96b]

$$f_e\left(\vec{r},\vec{p}\right) = \frac{1}{(2\pi)^3\epsilon_x\epsilon_y\sigma_p} \times exp\left\{-\frac{1}{2}\left(\frac{(x-x'z)^2+(\beta_x x')^2}{\beta_x\epsilon_x} + \frac{(y-y'z)^2+(\beta_y y')^2}{\beta_y\epsilon_y} - \frac{(p_z-p_o)^2}{\sigma_p^2}\right)\right\}, \quad (2.18)$$

where ϵ_x and ϵ_y are the beam emittances in the x and y direction, respectively. We have neglected the axial length of the electron beam. For the Duke facility, $\epsilon_x \gg \epsilon_y$, so most of our calculations will neglect the effect of uncertainties in the y-direction. "Emittance" will therefore refer to emittance in the x-direction. Typical values for the electron distribution are given in Table 2.1.

2.3.1 Energy Distribution

For γ-ray beams passing through small aperture collimators, the energy distribution is dominated by uncertainties in the electron beam. A monte carlo code GAMDIST was written to calculate the energy distribution for an arbitrary set of beam parameters. The parameters allowed to vary are beam position (x and y), energy, angular divergence, and collimator position. The uncertainty of photon linewidth ($\Delta E_\lambda / E_\lambda \sim 10^{-4}$) was neglected, as this only contributes a small uncertainty to the final distribution. GAMDIST randomly chooses a point inside the collimator aperture. It then randomly chooses the initial conditions for the electron generating the γ-ray, assuming Gaussian distributions with user defined parameters for the distribution functions. GAMDIST then checks this γ-ray against the cross section (Equation 2.15) to determine the probability of such a γ-ray being produced, and randomly accepts or rejects the γ-ray according to that probability. The set of accepted γ-rays are then binned and normalized for comparison with other distributions.

The finite parameters of the electron electron beam place a limit on the achievable resolution. Variations in the electron energy can raise or lower the energy of an observed γ-ray from the centroid value. Variations in the electron initial position and momentum always produce γ-rays with energies lower than the centroid energy

Parameter	Value
Electron Energy	1000 MeV
Photon Energy	8.0 eV
σ_x	0.0268 cm
σ_y	0.0071 cm
σ_θ	6.7×10^{-5} rad
$\Delta E_e/E_e$	5×10^{-4}
Collimator Diameter	1 mm
Collimator Distance	30 m

Table 2.2: DFELL parameters used in generating the spectra in Figure 2.12. The parameters were obtained from [Car96].

by allowing the center of the collimator to be hit by a γ-ray scattered at a non-zero scattering angle. Because most uncertainties allow lower energy γ-rays through a small collimator while only one comparatively small process allows higher energy γ-rays through, a typical γ-ray spectrum will be asymmetric with a sharp peak just below the calculated maximum γ-ray energy. Above this peak, the flux drops quickly, because only electrons in the high-energy tail of the electron energy distribution can generate these γ-rays. Below the centroid, the distribution decreases more gradually, resulting in a low energy tail. This low energy tail is more pronounced at higher electron energies, where angular deviations have a larger effect on the energy of a scattered γ-ray.

A typical γ-ray distribution at high energies is shown in Figure 2.12. The spectrum was generated by assuming 8 eV photons and 1.0 GeV electrons. Other beam parameters used in the calculation are given in Table 2.2. The low energy tail is shown to be strongly suppressed by reducing the angular uncertainty (σ_θ) of the electron bunch. This reduction can be accomplished by adjusting the tune of the electron orbit in order to decrease the angular divergence (x' or y'). This is done at the expense of increasing the bunch size (x or y).

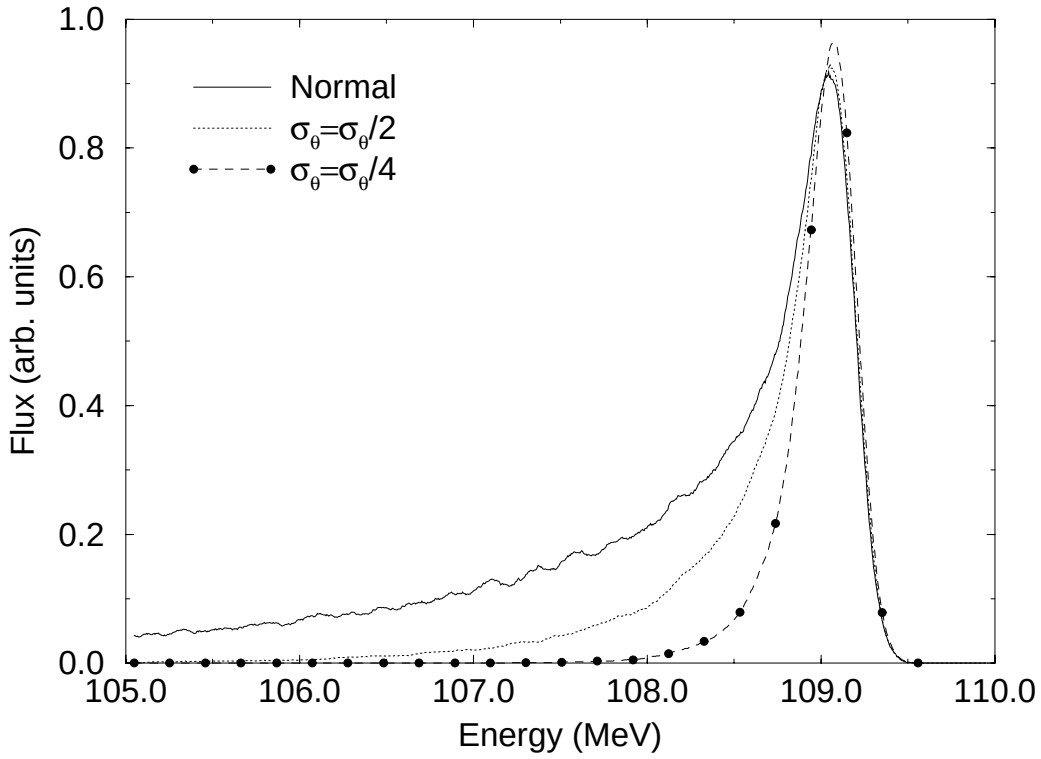

Figure 2.12: Gamma-ray distributions for varying angular divergences. The distribution was generated by assuming 8.0 eV photons and 1.0 GeV electrons.

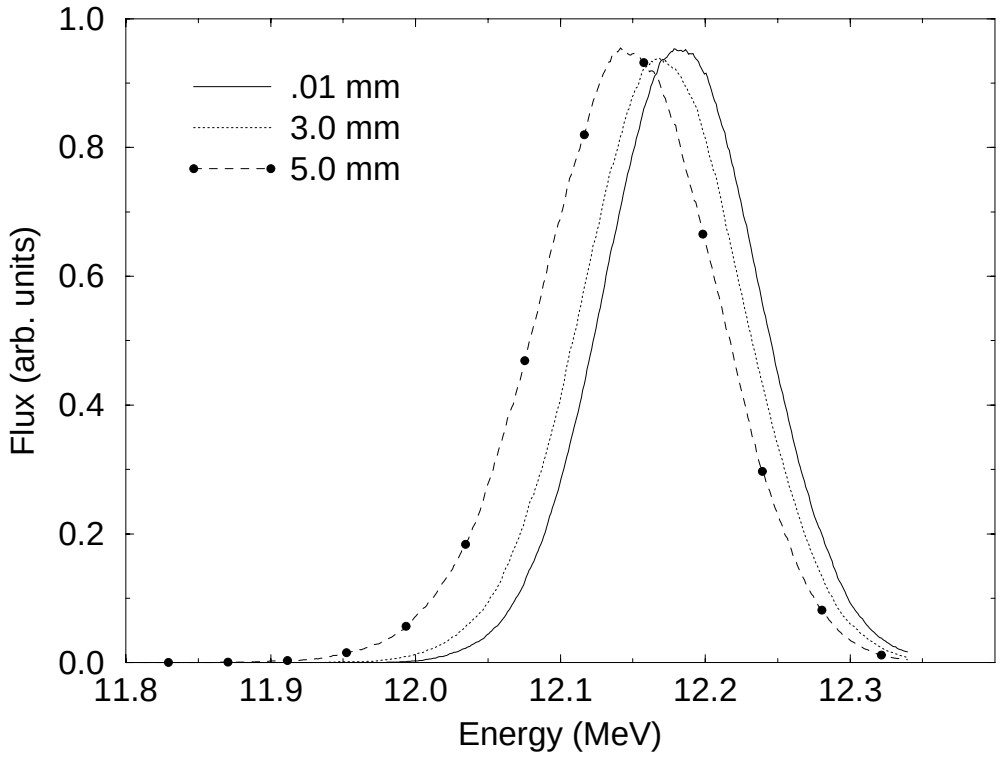

Figure 2.13: Gamma-ray distributions for varying collimator size. The distribution was generated assuming 3.26 eV photons and 500 MeV electrons. The FWHM of the .01, 3.0, and 5.0 mm distributions are 127, 128, and 143 keV, respectively.

Parameter	Value
Electron Energy	500 MeV
Photon Energy	3.26 eV
σ_x	0.0268 cm
σ_y	0.0071 cm
σ_θ	2.3×10^{-5} rad
$\Delta E_e/E_e$	2.2×10^{-3}
Collimator Distance	30 m

Table 2.3: DFELL parameters used in generating the spectra in Figure 2.13. The parameters were obtained from [Lit96a].

For low γ-ray energies (below $\sim$ 20 MeV), the γ-ray distribution is less focused, so that angular uncertainties in the electron beam have a less pronounced effect on the γ-ray energy distribution. Because low-energy tails are the result of angular uncertainties, they are strongly suppressed in low-energy γ-ray spectra, causing low-energy γ-ray distributions to appear more symmetric than higher energy distributions.

In the absence of uncertainties in the electron beam, the energy resolution $\Delta E_\gamma/E_\gamma$ can be made arbitrarily small by choosing a sufficiently small collimator. Uncertainties in the electron beam place a lower limit on achievable energy resolution for a given set of beam parameters. Figure 2.13 shows the energy resolution of the same γ-ray beam passing through collimators of increasing width. The beam parameters used, shown in Table 2.3, reflect the status of the storage ring during measurements taken in December 1996 (see Section 3.2). The FWHM energy resolution corresponding to the three collimators are 127 keV, 128 keV, and 143 keV for the 0.02, 3.0, and 5.0 mm diameter collimators, respectively. This indicates that decreasing the collimator size below 3 mm will not appreciably improve the energy resolution of this particular γ-ray beam. This calculated minimum resolution of 1% is in excellent agreement with measured values [Lit97]. Note that the center of the γ-ray distribution appears

to change slightly for different collimators. This is the result of the scattering cross section being relatively flat across the small angular differences subtended by the different collimators. The centroid energy represents the average energy of γ-rays passing through the collimator.

2.3.2 Flux

We define flux, according to convention used for similar γ-ray facilities, as the number of γ-ray photons incident on some target per second. The γ-ray fluxes possible for the HIGS facility are dependent on the available range of DFELL parameters. The total flux of γ-rays produced over all angles is proportional to the scattering cross section, the number of electrons available for scattering, and the number of photons in the optical cavity. The total scattering cross section can be determined by integrating the unpolarized differential cross section given in Equation 2.12. The resulting total cross section is given by

$$\overline{\sigma}_{tot} = \frac{2\pi r_e^2}{x}\left\{\left(1 - \frac{4}{x} - \frac{8}{x^2}\right)\ln\left(1+x\right) + \frac{1}{2} + \frac{8}{x} - \frac{1}{2\left(1+x\right)^2}\right\}. \tag{2.19}$$

For scattering in which the incident photon energy is much less than the electron rest mass, as is the case at the Duke facility, $x \ll 1$, and Equation 2.19 reduces to

$$\overline{\sigma}_{tot} \cong \frac{8\pi r_e^2}{3}\left(1 - x\right), \tag{2.20}$$

which is approximately equal to the classical Thompson cross section [Ber71].

The maximum intracavity photon flux available for Compton scattering for a given photon energy is shown in Figure 2.7. The number of electrons available for scattering photons will be some portion of the total current in the storage ring. One advantage to intracavity Compton scattering in an FEL is the automatic alignment

of the electron bunches and the laser light. The set of possible photon positions and trajectories is defined by the geometry of the optical cavity, suggesting that a misalignment may be possible. However, photon trajectories that do not intersect the electron trajectories do not allow the photons to be amplified, so laser modes operating in such a state will not experience gain. It can be assumed, therefore, that the electron and photon beams are well aligned, and all electrons and photons are available for Compton scattering. The number of "target" electrons available for scattering photons is therefore the total number of electrons in the storage ring. As determined in Section 2.1.3, the number of photons generated for a typical electron beam is approximately proportional to $I^{3/2}$, where I is the electron current. The total γ-ray flux is therefore proportional to $I^{5/2}$ for most operating conditions [Par98].

An exception to the above scaling law occurs when one or more electron bunches are prevented from lasing. The simplest manifestation of this configuration would be to have two electron bunches in the storage ring: a small "lasing" bunch that operates normally, and a larger "target" bunch that is prevented from lasing by reshaping the bunch such that the peak current is below lasing threshold [Par98]. In this mode, γ-rays are only produced when photons generated by the lasing bunch scatter from electrons in the target bunch. Because the target bunch will not experience the increased momentum spread associated with lasing, the resulting γ-rays have a lower intrinsic energy spread than they would if they were generated in a standard operating mode in which all electrons bunches are allowed to lase. In this operating mode, the photon flux is proportional to the product of $I_{lasing}^{3/2}$ and I_{target}, rather than to $I_{total}^{5/2}$.

In the standard operating mode, the rate of γ-ray production for a given set of beam parameters can be calculated by taking the product of the cross section (Equation 2.19), the number of electrons, and the photon flux (Figure 2.7) and dividing by

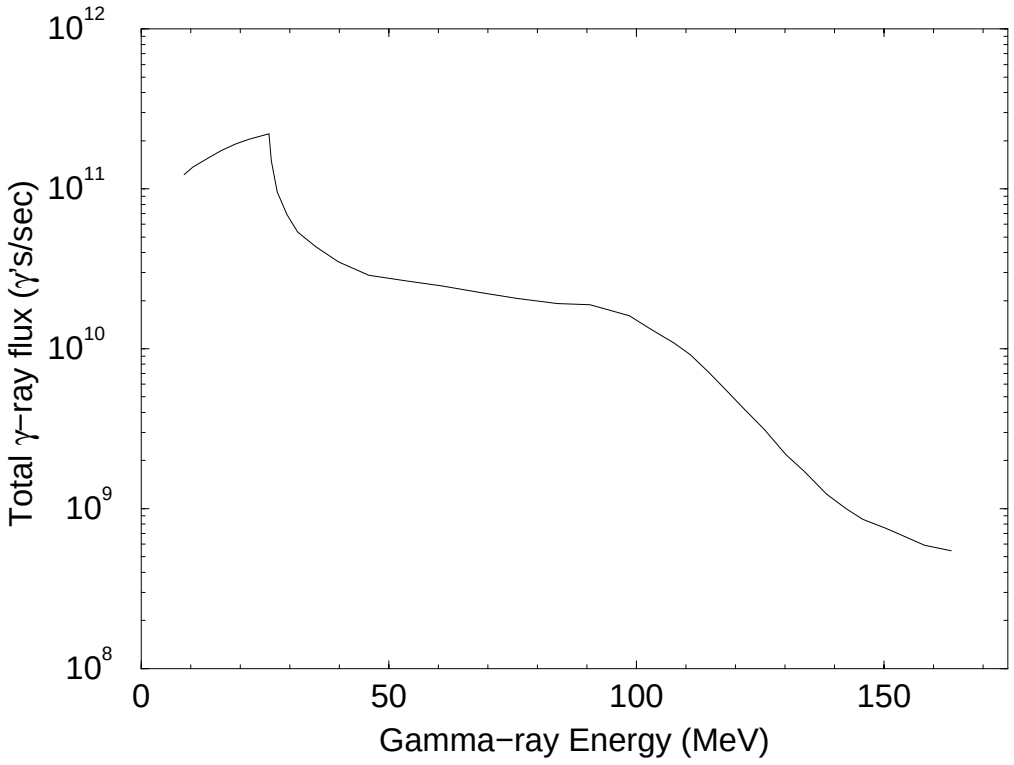

Figure 2.14: Maximum γ-ray flux for a given γ-ray peak energy assuming a 10 mA lasing bunch and a 100 mA scattering bunch in the storage ring [Lit96b].

the effective interaction area for the photons and electrons [Lit96b]. The resulting total γ-ray fluxes are shown in Figure 2.14. This distribution assumes 110 mA of current in the storage ring. Because the storage ring was designed to eventually store one Amp of current, these fluxes can, in principle, be increased by a large factor.

Most experiments will not be able to utilize the entire fluxes shown in Figure 2.14 because most experiments require a narrow energy resolution. As stated previously, energy resolution is achieved by collimating the γ-ray beam, which prevents a significant fraction of γ-rays from reaching the experimental area. The flux through a given collimator can be calculated by integrating the differential cross section over the area of the collimator. For most experiments, any practical collimator will subtend a small enough angle that the cross section is essentially constant throughout the area. The flux through a collimator therefore scales with the area of the collimator. Calculating the flux for a desired energy resolution requires the inclusion of specific beam parameters, and can therefore only be calculated numerically. Gamma-ray fluxes for an energy resolution of $\Delta E/E = 1\%$ can be estimated from Figure 2.14 by taking 1.5% of the total shown. The factor of 1.5 comes from taking the average flux vs. energy, as shown in Figure 2.11, where we note that the flux near the maximum energy is approximately 1.5 times this average.

2.3.3 Polarization

The polarization of scattered γ-rays is strongly dependent on the polarization of the incident FEL photons. This is most easily seen by considering the scattering in the rest frame of the electron. The use of this frame is valid because changing from the electron rest frame to the laboratory frame can not rotate a photon's polarization vector.

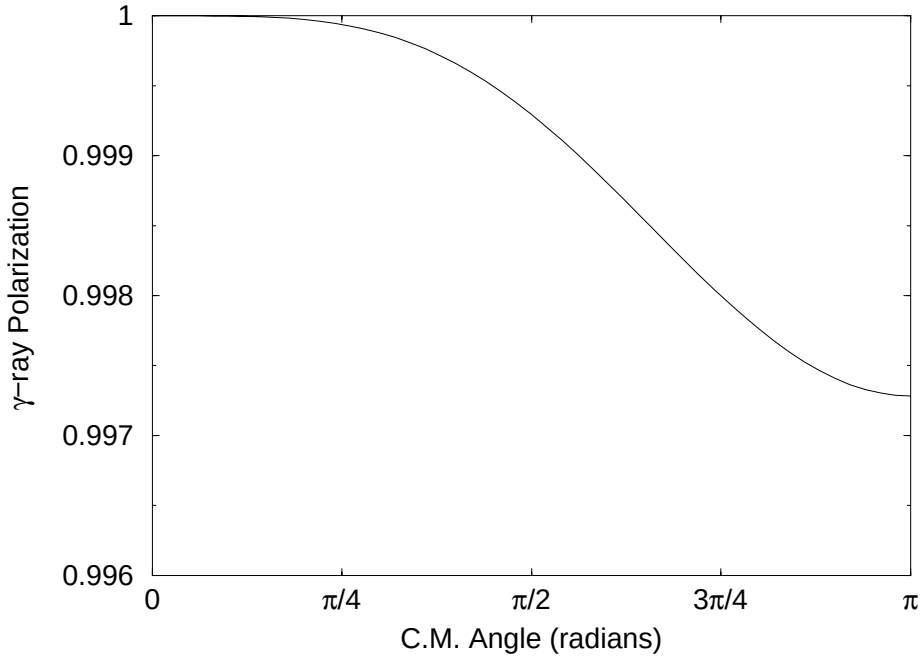

Figure 2.15: Gamma-ray polarization as a function of scattering angle in the electron rest frame. This distribution assumes 5 eV FEL photons scattering from 1 GeV electrons.

We consider the polarization-dependent cross section in the electron rest frame for the case of linearly polarized incident photons. Equation 2.14 becomes [Ber71]

$$d\sigma = \frac{1}{4} r_e^2 \left(\frac{E'}{E}\right)^2 \left(\frac{E'}{E} + \frac{E}{E'} - 2 + 4\cos^2\Theta\right) d\Omega, \tag{2.21}$$

where E and E' are the incident and scattered photon energies and Θ is the angle between the incident and scattered photon polarization vectors. In the low energy limit when $E \ll m_e c^2$, $E \approx E'$ and the cross section goes to $d\sigma = r_e^2 \cos^2\Theta d\Omega$. The polarization of the γ-rays is defined as

$$P = \frac{\sigma_{||} - \sigma\perp}{\sigma_{||} + \sigma_\perp} = \frac{2}{\frac{E}{E'} + \frac{E'}{E}}, \tag{2.22}$$

where $\sigma_{||}$ and $\sigma_\perp$ are the cross sections for scattered photon polarizations parallel and perpendicular to the incident photon polarization, respectively. In the nonrelativistic

limit, the polarization of the scattered photons is therefore given by $P = 1.0$. This is approximately correct for the DFELL facility. For example, a 5 eV FEL photon appears as a 19.6 keV photon in the rest frame of a 1 GeV electron in the storage ring. This photon energy is well below the electron rest mass, so we expect the scattered photon to have approximately the same energy as the incident photon. Using the energy-angle correlation from Equation 2.3, we can express Equation 2.22 in terms of scattering angle. A sample distribution in the electron rest frame is shown in Figure 2.15. The scattered γ-ray polarization is never less than 0.997 for any scattering angle. Because the incident FEL photons are known to be 100% linearly polarized in the horizontal direction, the scattered γ-rays will also be $\sim 100\%$ linearly polarized in the same plane.

2.3.4 Backgrounds

Synchrotron Radiation

All charged particles undergoing acceleration will radiate some portion of their energy away in the form of photons. Because the total radiated power is inversely proportional to the square of the particle mass, electron accelerators are particularly susceptible to producing a photon background in this manner. The process of emitting photons while an electron is traveling along a curved trajectory is called synchrotron radiation.

Synchrotron radiation is not expected to produce a significant γ-ray background at the HIGS facility because the energy distribution of the synchrotron photons is centered at an energy far below that of γ-rays produced by Compton backscattering. Synchrotron radiation is characterized by a critical frequency ω_c above which only

negligible radiation is emitted [Jac75]. For a 1 GeV electron beam, this critical frequency is given by

$$\omega_c = 3\left(\frac{E_e}{m_e c^2}\right)^3 \frac{c}{\rho} = 3.36 \times 10^{18}\ rad/sec, \tag{2.23}$$

which corresponds to a photon energy of 2.22 keV. Because this is so far below the γ-ray energies produced via Compton backscattering, any signal produced by synchrotron radiation can easily be filtered out of the γ-ray beam before it reaches the target.

Bremsstrahlung

A source of background with a greater potential to pollute the γ-ray beam is bremsstrahlung. Bremsstrahlung originates when high-energy electrons interact with the residual atoms in the evacuated beam line. As the electrons pass the atoms, the positive nuclei accelerate the electrons, causing them to radiate away some percentage of their energy in the form of photons. Depending on how much of the electron's kinetic energy is lost in the collision, the photons can have energies ranging from almost nothing to the full initial energy of the electron. In addition, the photons can be emitted directly down the beam axis, allowing them to co-propagate with Compton-scattered γ-rays, thus polluting the γ-ray beam with photons that have similar energies, but that lack the polarization and energy-angle correlation of the Compton scattered γ-rays.

The idealized spectrum for bremsstrahlung radiation is well documented, and is derivable from quantum-electrodynamics [Gro93]. A rigorous treatment of the bremsstrahlung background for a particular facility is highly dependent on the specific characteristics of the facility in question. A good treatment of bremsstrahlung

in electron storage rings is given in [Rin82]. This approximation shows that the number of bremsstrahlung photons having energies between k and k+dk for an electron beamline of length L is given by

$$F_k dk = 8.21 \times 10^{11} Z(Z+1) P \left(\frac{273}{T}\right) I \frac{dk}{k} \times \left[\left(1 + \left(\frac{k}{E_0}\right)^2 - \frac{2}{3}\left(\frac{k}{E_0}\right)\right) \ln\left(183 Z^{-\frac{1}{3}}\right) + \frac{1}{9}\left(\frac{k}{E_0}\right)\right] \times L \quad (2.24)$$

where Z is the average atomic number of the residual gas in the beamline, P is the pressure in Torr, T is the temperature in degrees Kelvin, I is the electron current in electrons/sec, and E_0 is the energy of the electron beam in MeV. Typical operating parameters for the Duke Storage Ring are 10 mA of beam current (I=$6.23 \times 10^{16} e/s$), pressures of P=10^{-9} Torr, temperatures of 300 K, and an active length of L=35 m of beamline from which bremsstrahlung can co-propagate with Compton scattered γ-rays. If we conservatively estimate the average Z of the residual gas to be ~ 10, then an 800 MeV electron beam will produce approximately 73 photons/sec with energies between 198 and 200 MeV. Because this conservative estimate is still several orders of magnitude below our predicted flux of good γ-rays, bremsstrahlung is not expected to be a major problem as a source of background.

Chapter 3

Gamma-ray Production: Measurements

3.1 Background Measurements

The predictions of Section 2.3.4 indicate that the bremsstrahlung γ-ray background is not expected to occur in fluxes comparable to that of the Compton scattered γ-rays. These predictions were tested as soon as the DFELL Storage Ring became operational.

3.1.1 NaI Detectors

Measurements of bremsstrahlung background were made using a Sodium Iodide (NaI) scintillating crystal. The detector consisted of a 25.4 $\times$ 25.4 cm cylindrical crystal encased in a thin aluminum shell. A γ-ray entering the detector would interact

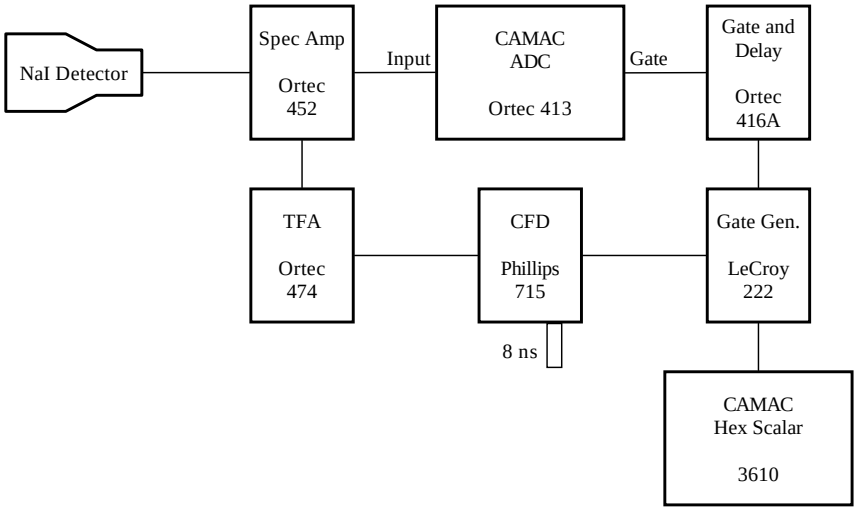

Figure 3.1: Standard setup for NaI detector electronics.

with the crystal and produce a shower of low energy photons and electrons. The number of low-energy photons produced is roughly proportional to the energy of the initial γ-ray. A small doping of thallium (Tl) shifts the wavelength of the low energy photons to a range at which photomultiplier tubes can detect them with high efficiency. Six RCA 8575 photomultiplier tubes convert the photon pulses into current pulses, which are then converted to voltage pulses whose voltage is proportional to the energy of the incident γ-ray to within some intrinsic energy resolution. This detector has has been extensively tested [Wel81], and the energy resolution over the range of interest for the γ-ray facility varies from about 6% for 4 MeV γ-rays to about 3% or better for γ-rays above 15 MeV.

The voltage pulses from the six photomultiplier tubes are added together and sent through the electronics setup shown in Figure 3.1. A spectroscopy amplifier shapes and amplifies the voltage pulse into a form suitable for an analog-to-digital converter (ADC). The unipolar output of the spectroscopy amplifier is sent to the analog input of the ADC, while the bipolar signal is sent through the circuit that gates that ADC. This circuit consists of a timing filter amplifier (TFA) and constant fraction discriminator (CFD) that tests the signal against a voltage threshold set by the experimenter. Because a poorly shaped pulse can sometimes cause the CFD to produce two gates corresponding to the same input signal, the NIM output of the CFD is sent to a series of two gate and delay modules. The first module creates a long ($\sim 10\ \mu sec$) gate that triggers on the first pulse to come from the CFD. Because the second pulse, if any, would arrive before the long pulse ended, the module does not react to the second pulse, and no spurious gates are sent to the ADC or the scalar counter modules. The resulting long gate triggers a shorter gate ($\sim 1\ \mu sec$) in the second gate and delay module, which is sent to the ADC to act as a gate for the analog signal. The ADC digitizes the analog signal from the NaI, and the results are analyzed using the TUNL XSYS data acquisition system.

Because the NaI(Tl) detector has an imperfect efficiency and energy resolution, the spectrum produced by the data acquisition system is not an entirely accurate representation of the γ-ray distribution incident on the detector. To correct for this, the response function of the detector had to be determined. This was accomplished by simulating the detector system with the EGS4 code [Nel85]. EGS4 (which stands for Electron-Gamma Shower version 4) is a monte carlo program that simulates the electromagnetic interactions of electrons, positrons, and photons as they pass through various materials in a user defined geometry. The simulation used to determine the

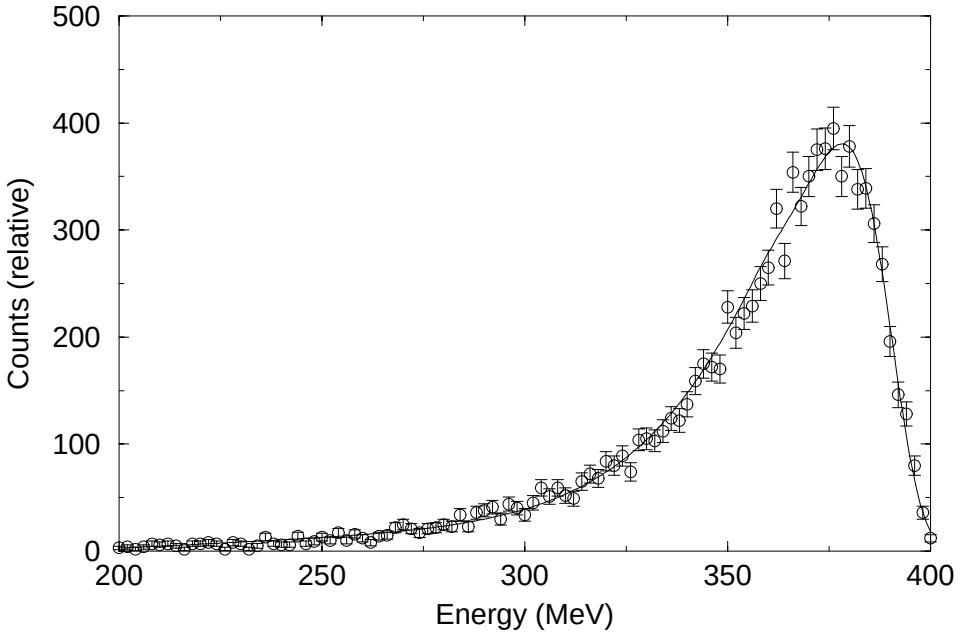

Figure 3.2: Response function for 400 MeV γ-rays on a 10"x10" NaI crystal. The circles represent results from an EGS4 Monte Carlo calculation, and the solid line is a fit to the EGS4 results consisting of two quartic exponentials.

NaI(Tl) response function assumed a perfectly monochromatic pencil beam of 400 MeV γ-rays incident on the center of the front face of a pure NaI crystal matching the geometry of our detector. The small amount of thallium in the crystal was not expected to affect our results, and was therefore left out of the simulation. For each incident γ-ray, the total amount of energy deposited in the crystal was recorded.

The resulting response function is shown in Figure 3.2. In order to use this line-shape for γ-ray energies other than exactly 400 MeV, a functional fit was performed. Previous experiments at TUNL [Bal92] have demonstrated that a NaI(Tl) response function can effectively fit using two quartic exponentials, as shown below.

$$\begin{aligned} f(x) &= e^{A+Bx+Cx^2+Dx^3+Ex^4} \text{ for } E_{low} \leq x \leq S; \\ g(x) &= e^{F+Gx+Hx^2+Ix^3+Jx^4} \text{ for } S \leq x \leq E_{high}, \end{aligned} \tag{3.1}$$

where x is the total energy deposited in the crystal from the initial γ-ray, A-J are

Coefficient	Value
A	-108.7136072935135
B	1.540180714862355
C	-8.0499325728083215e-3
D	1.8655418340624033e-5
E	-1.5910043827471888e-8
F	-46493.58155795427
G	508.1288253919843
H	-2.082486846401332
I	3.7935059737028285e-3
J	-2.5914663920353161e-6
S	356.7770173883060
E_{low}	200
E_{high}	401

Table 3.1: Coefficients and constants used in fitting the NaI response function for 400 MeV γ-rays.

coefficients, and S is the point at which f(x) and g(x) are equal in magnitude and slope. This function was fit using the code LINEFIT [Bal92], which used the chi-square minimization routine MINUIT to fit the eleven parameters. Because the exponential functions are extremely sensitive to small changes in the values for the coefficients, a high degree of accuracy was required. The resulting coefficients are given in Table 3.1, and the functional fit is shown with the EGS4 results in Figure 3.2. The resulting function could then be scaled and used as the response function for any high-energy γ-ray for which the NaI(Tl) resolution is approximately the same.

3.1.2 Measurement Results

The background measurements for electron energies of 400, 600 and 800 MeV are shown in Figure 3.3. The measured backgrounds were found to be very consistent with the expected bremsstrahlung distribution. The calculated distribution for 400

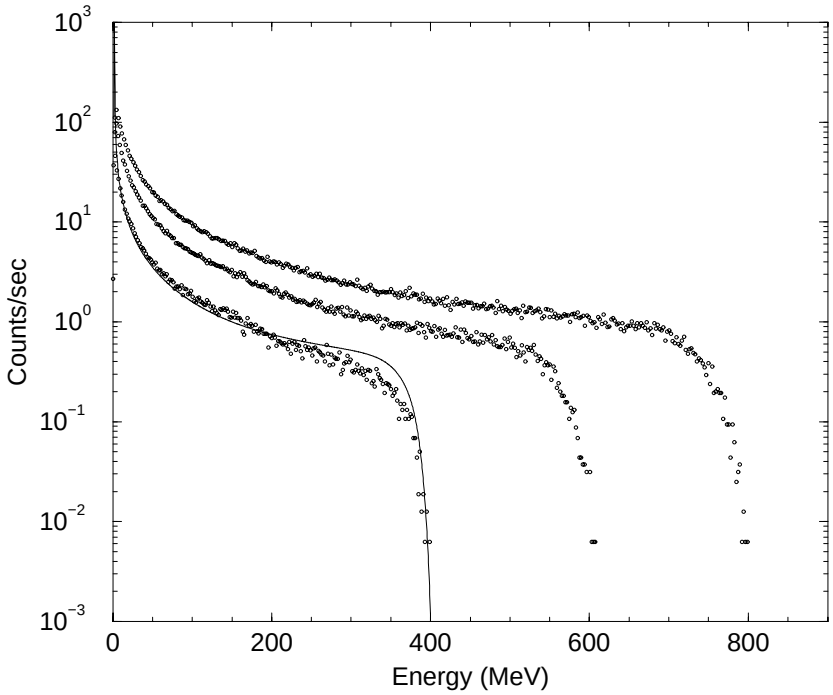

Figure 3.3: Calculated (solid line) and measured (points) bremsstrahlung spectra for E_e=400, 600, and 800 MeV.

MeV electrons is shown along with the experimental data in Figure 3.3. The calculated spectrum was generated by assuming a bremsstrahlung spectrum described by Equation 2.24 and convoluting it with the NaI response function described by Equation 3.1. The good correlation between our calculations and the data confirms our expectation that the largest contributor to γ-ray background at HIGS will be bremsstrahlung. The bremsstrahlung count rate is on the order of 10^2 γ's/sec at the likely energies of Compton scattered γ-rays, meaning that ratio of "good" γ-rays to background γ-rays will be on the order of 10^5 or better.

3.2 Initial γ-ray Measurements

The first γ-rays from the HIGS facility were observed in December 1996 [Lit97]. A variety of measurements, documented below, demonstrated that the properties of the γ-ray beam which was produced were in agreement with our expectations.

3.2.1 Beam Parameters

The γ-ray beam used for the initial experiments was at the low end of the projected energy range of the facility. The electrons were injected at 270 MeV and ramped to an energy of E_e=500 MeV (γ=978.5). Two electron bunches containing 1.2 mA each were injected in this manner, and both were allowed to lase. The OK-4 produced a photon wavelength of λ=379.4 nm, corresponding to a photon energy of 3.27 eV. This wavelength was measured with a monochromator. The resulting intracavity power was measured to be 0.54 W, corresponding to an FEL photon flux of 1.03×10^{18} sec^{-1} [Lit97].

These beam parameter were calculated to produce a γ-ray beam with a peak energy of 12.2 MeV at a flux of $2.6 \times 10^5 \gamma$'s/sec [Lit97]. Allowing both electron bunches to lase was expected to add an additional energy spread to the γ-ray beam, typically on the order of $0.4\% - 0.5\%$ FWHM. This energy spread would be in addition to any energy spread resulting from collimator size.

3.2.2 Experimental Setup

The experimental area for these measurements is shown in Figure 3.4. The γ-ray beam originates in the OK-4, passes through the optical cavity mirror and the CaF_2

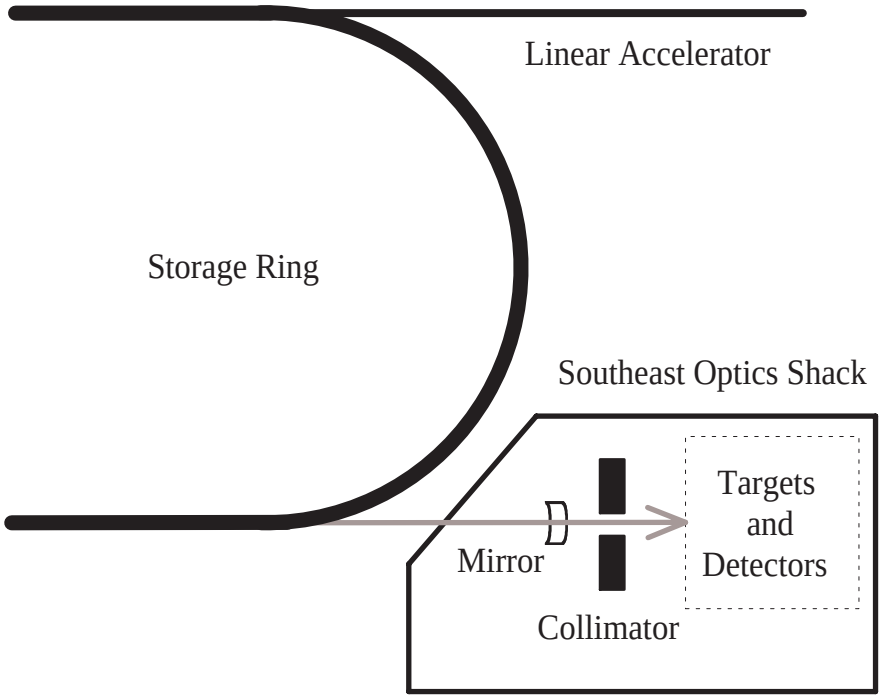

Figure 3.4: General layout of 1996 γ-ray measurements.

window, and propagates through open air in the optics shack. A large collimator ($\sim$ 5 cm in diameter) consisting of stacked lead blocks shielded the experimental area from scattered γ-rays not propagating directly down the beam axis. The beam then passed through a smaller collimator consisting of a $2'' \times 4'' \times 8''$ lead brick with a hole drilled through the 4" axis at the center of the $2'' \times 8''$ face. This collimator, the diameter of the which was varied using a series of inserts depending on the nature of the measurement being taken, defined the energy resolution of the γ-ray beam. The beam then entered the detector area, which held a variety of detector systems, depending on whether the flux, energy resolution, or polarization of the γ-ray beam was being measured.

Alignment between the collimator and γ-ray beam was of critical importance.

The beam spot from the laser light provided a rough estimate of the center of the γ-ray distribution. This did not provide an entirely accurate position for the γ-rays for two reasons. First, although the FEL light is always projected in the forward direction with respect to the mean electron beam path through the undulator, the direction of γ-ray scattering can vary as a function of the location of the collision point, since the instantaneous direction of the scattering electrons is changed. Second, the laser light can be reflected and refracted through mirrors and beam splitters, while the γ-ray trajectory will remain unchanged.

The method used for aligning the collimator and the center of the γ-ray distribution was the maximization of flux through the collimator. Because the Klein-Nishina cross section is maximum for $\theta = 0°$, a collimator centered on the γ-ray distribution will allow the greatest number of γ-rays though the aperture for a given set of storage ring parameters. The collimator was therefore roughly aligned with the FEL laser beam, and fine adjustments to the position of the collimator were made by hand or by stepper motors until the flux was maximized.

3.2.3 Flux Measurement

The first measurement taken of the Compton scattered γ-rays was an attempt to measure the flux. Because a measurement of the entire γ-ray beam was desired, a large aperture (1") collimator was used to allow virtually all of the γ-rays through. The γ-rays were detected by the same NaI(Tl) detector apparatus and electronics described in Section 3.1.1. The expected flux calculated in Section 3.2.1 would overload the NaI(Tl) detector, so a 10 cm lead wall was placed between the beam and the detector. This wall attenuated the γ-ray beam by a factor of ~ 150, reducing the flux to a level more manageable by the detector.

After correcting the data for detector efficiency and attenuation from the lead shielding, the γ-ray flux was found to be $2.0 \times 10^5 \gamma$'s/sec. This result is in good agreement with the expected flux of $2.6 \times 10^5 \gamma$'s/sec [Lit97]. The possible causes of this discrepancy include a misalignment of the collimator and possible instabilities in the FEL lasing mode, leading to a time-averaged lower photon flux than expected.

3.2.4 Energy Resolution Measurement

The flux measurements made by the NaI detector correspond to the total number of γ-rays scattered from the electron beam. These γ-rays have energies ranging from 12.2 MeV down to a few keV, although the cross section becomes very small for energies less than 3 MeV.

Many nuclear physics experiments require a more monochromatic beam. As described in Section 2.2, the correlation between γ-ray energy and angle makes it possible to monochromatize the beam by inserting a collimator between the collision point and the detector. For our measurements, a 3 mm diameter collimator was placed along the beam axis approximately 30 m from the collision point. The collimator consisted of a 10 cm thick piece of lead with a 3 mm diameter hole drilled through it. The collimator position was optimized by making small position adjustments until the flux was maximized.

HPGe Detectors

With γ-ray energy resolutions predicted to be $\Delta E/E \leq 1\%$, it is clear that the NaI detector used in the flux measurement would not be able to observe this resolution directly. A precision energy resolution measurement was therefore made using a

coaxial High Purity Germanium (HPGe) detector. The intrinsic energy resolution of an HPGe detector has been measured to be 1.5 keV at E_γ=1.33 MeV and 4.2 keV at E_γ=5.5 MeV [Sch96].

An HPGe detector is a semiconductor detector. When a γ-ray enters the active region of the detector, it creates electron-hole pairs that are accelerated by a large electric bias. This bias is applied to a high-voltage lead running down the center of the crystal. The high-voltage lead is biased to +3000 V. An aluminum cylinder surrounding the crystal acts as ground.

The detector used for our measurements is a p-type HPGe. This is the standard type of Germanium detector and is doped with Gallium to create extra holes in the crystal. As the electrons and holes accelerate towards the high-voltage lead, they cascade and produce additional electron-hole pairs. The lead then collects the current pulse which has a charge proportional to the energy of the incident γ-ray. The current pulse is changed into a proportionate voltage pulse by a preamplifier mounted on the detector. Noise in the preamp signal is minimized by keeping the detector and preamp in thermal contact with a liquid nitrogen dewar which keeps the entire system below $\sim$100 K. This low temperature also reduces the number of thermally produced electron-hole pairs in the crystal. A thermal sensor in contact with the detector deactivates the power supply if the temperature increases to a level that is potentially damaging for the preamplifier or crystal.

A typical spectrum for an HPGE detector is shown in Figure 3.5. The spectrum is representative of the energy deposited by a 5.5 MeV γ-ray from ^{2}H(p,γ). The structure in the spectrum results from both the geometry of the detector and the physical processes that contribute to γ-ray absorption. At low energies, generally a few hundred keV and below, the dominant photoabsorption process is the photoelec-

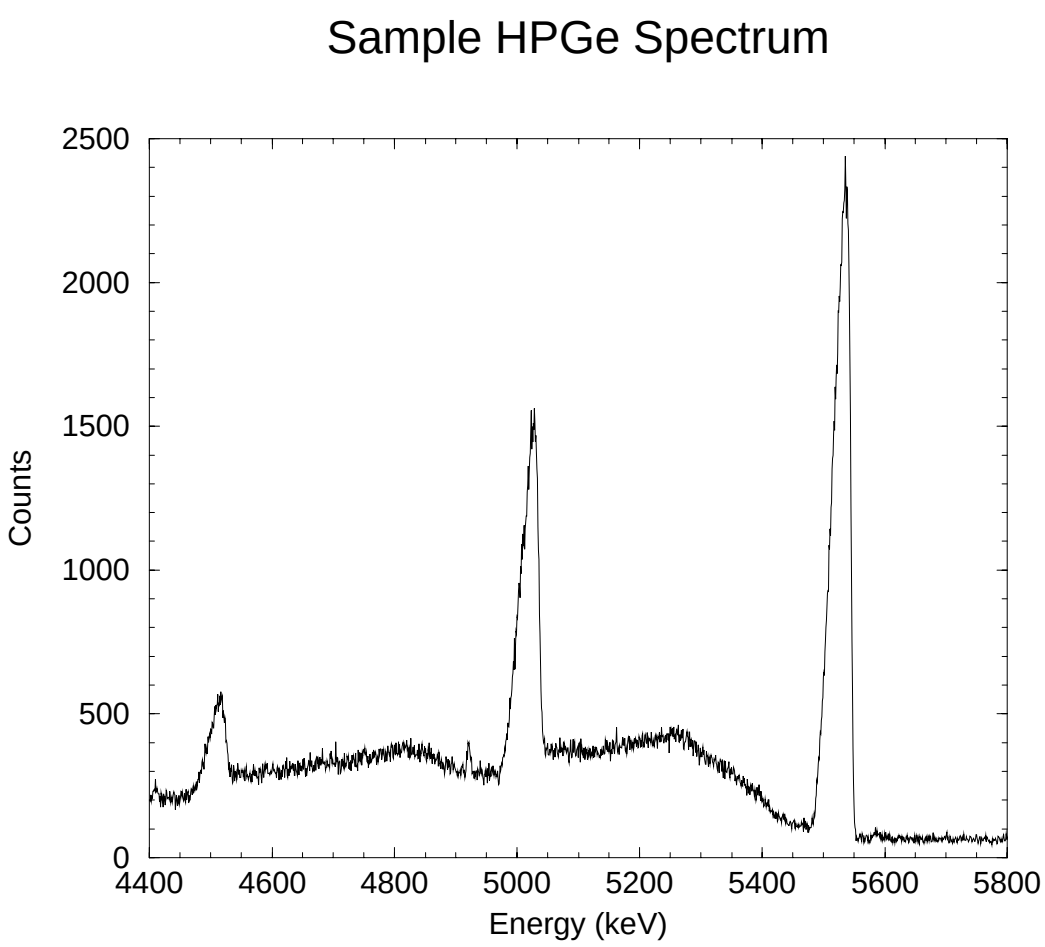

Figure 3.5: Sample HPGe spectrum. This distribution is generated from a nearly monochromatic source of γ-rays from the ^{2}H(p,γ) reaction. The spectrum is taken from [Wul98].

tric effect. In this process, the γ-ray energy is absorbed by an atom or lattice, from which an electron is emitted with a kinetic energy equal to the γ-ray energy minus the binding energy or work function of the electron. This binding energy is generally on the order of a few eV.

At higher energies, Compton scattering becomes the dominant photoabsorption process. In Compton scattering, the γ-ray scatters from a bound electron, losing some of its energy to electron recoil. The energy of the scattered γ-ray can be related to

the scattering angle by requiring conservation of energy and momentum, which gives the following expression:

$$E' = \frac{E}{1 + \frac{E}{m_e c^2}(1 - \cos\theta)} \tag{3.2}$$

where E and E' are the energies of the incident and scattered γ-rays, $m_e c^2$ is the rest mass of the electron, and θ is the scattering angle in the electron rest frame. This means that the scattered γ-ray can have an energy ranging from $E = E_\gamma/(1 + 2E_\gamma/m_e c^2)$ to the full initial energy as θ varies from 0 to 180°. The Compton distribution on the γ-ray spectrum results when the scattered γ-ray escapes from the crystal and the recoil energy of the electron is detected. The Compton edge occurs when this scattering occurs at 180°, in which case the γ-ray deposits all but $E = E_\gamma/(1 + 2E_\gamma/m_e c^2)$ in the crystal.

If the γ-ray has an energy greater than 1.022 MeV, the γ-ray can spontaneously become an electron-positron pair in the field of an atomic nucleus. This effect, called pair production, becomes the dominant photoabsorption process at energies greater than a few MeV. The electron and positron both deposit their kinetic energy in the detector by interacting with electrons in the crystal via bremsstrahlung and atomic ionization. When the positron loses all of its kinetic energy, it annihilates with an electron and produces two 511 keV γ-rays emitted at 180° with respect to each other. When one of these photons escapes, the HPGe records the entire energy of the initial γ-ray minus 511 keV, forming the first escape peak shown in the spectrum. When both 511 keV photons escape, a second escape peak is formed.

The efficiency of this HPGe detector has been measured and calculated in a previous work [Sch96], as shown in Figure 3.6. The low photopeak efficiency ($\leq 10\%$ for $E_\gamma > 10$ MeV) and the comparatively long signal size (~ 10 μsec) of the HPGe detector limit the detector's usefulness in flux measurements.

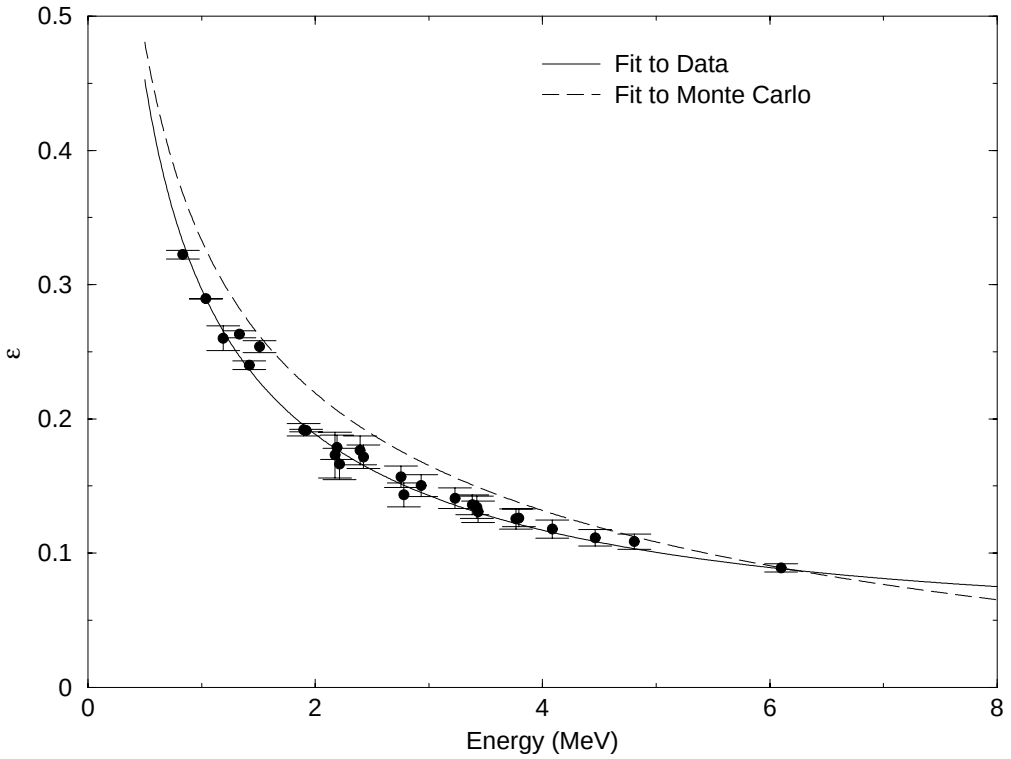

Figure 3.6: Measured and simulated γ-ray detection efficiencies for an HPGe detector.

The electronics for the HPGe setup are very similar to those used for the NaI(Tl) detector shown in Figure 3.1. Because of the comparatively long signal width from the HPGe ($\sim 10\ \mu sec$), only one gate and delay module was employed. However, the maximum count rate which could be tolerated and still maintain a quality spectrum was considerably less than for the NaI(Tl) detector.

Measurement Results

The initial set of measurements demonstrated that the γ-ray beam had been successfully monochromatized to within $\Delta E/E \sim 1\%$. To obtain an accurate measurement of the γ-ray energy and energy resolution, the HPGe detector was calibrated using two γ-ray emission lines from a ^{60}Co source (1.173 and 1.333 MeV) and the full

energy and first escape peak from an AmBe source (4.439 and 3.928 MeV). A typical spectrum is shown in Figure 3.7. The full energy peak is clearly visible at the appropriate energy (12.2 MeV), as are the first escape peak and Compton distributions. The energy spread of the γ-ray beam was determined by performing a Gaussian fit to the full energy peak. Because this peak and the Compton distribution run together, the initial Gaussian fit was calculated by constraining the centroid to be at 12.2 MeV and only fitting the high energy side of the distribution. The result of this fit, shown in the insert of Figure 3.7, indicates a FWHM of 120 keV, corresponding to an energy resolution of $\Delta E/E = 0.98\%$. Fitting a Gaussian to the entire peak indicated an energy spread of $\Delta E/E = 1.25\%$. The "true" value should lie between these limits. A calculation based on the procedure outlined in Section 2.3.1 indicated that an energy resolution of $\Delta E/E = 1.05\%$ should have been observed. This agrees extremely well with the measured value.

An attempt was then made to separate the γ-ray lineshape from the detector response function by isolating the first escape peak. This was accomplished by placing a NaI annulus around the HPGe detector. The annulus had an inner diameter of 10 cm, an outer diameter of 23 cm, and was comprised of four separate NaI sections, each subtending 90°. The four sections were fanned together to make the annulus behave as a single detector.

A software cut was enacted that only counted HPGe events that were coincident with events in the NaI annulus corresponding to 511 keV. Under these conditions, all counts in the HPGe spectrum should correspond to γ-ray events in the first escape peak, events in the second escape peak in which the second 511 keV γ-ray is not detected by the annulus, and Compton events that deposit 511 keV in the NaI crystal. The poor energy resolution of the NaI annulus allowed additional events to leak

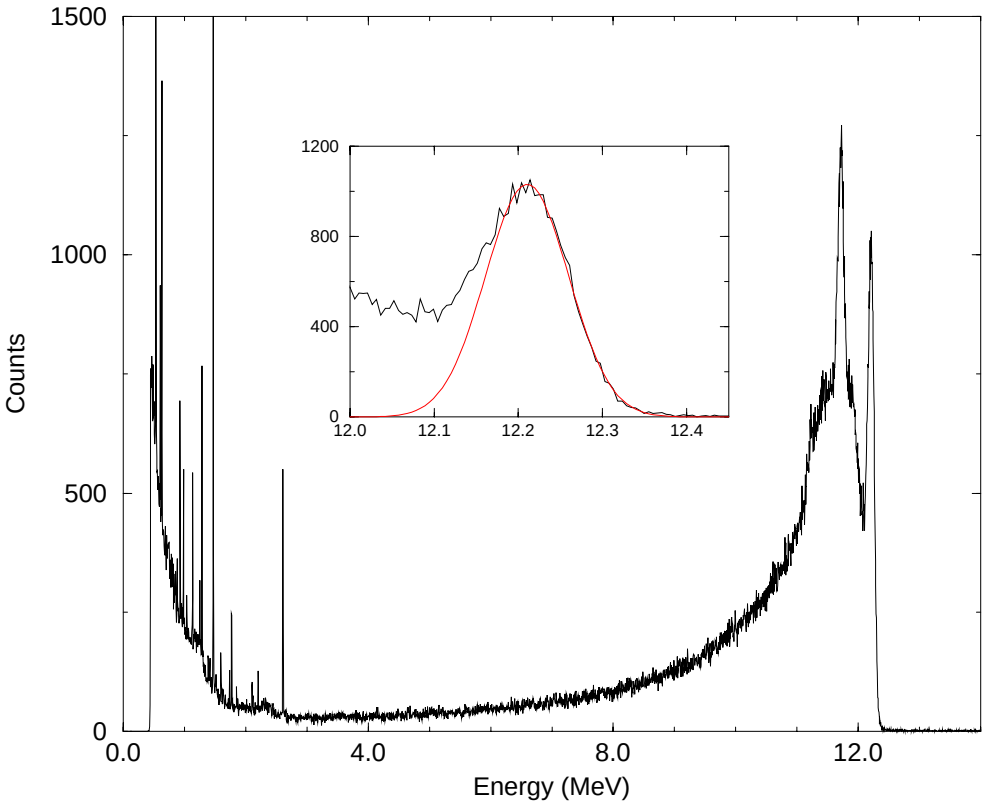

Figure 3.7: Full γ-ray spectrum for E_γ=12.2 MeV. The insert shows a Gaussian fit to the photopeak. The fit has a FWHM of 120 keV, indicating a 1% energy resolution.

into the spectrum as background. This background contribution could be observed independently of the γ-ray events of interest by setting additional gates on the NaI spectrum above and below the 511 keV peak. This background could then be subtracted from the "good" HPGe spectrum. The results of this measurement are shown in Figure 3.8. A measurement of the width of the first escape peak at E_γ=11.69 MeV confirms that the FWHM energy resolution of the γ-ray beam is $\Delta E/E = 1\%$.

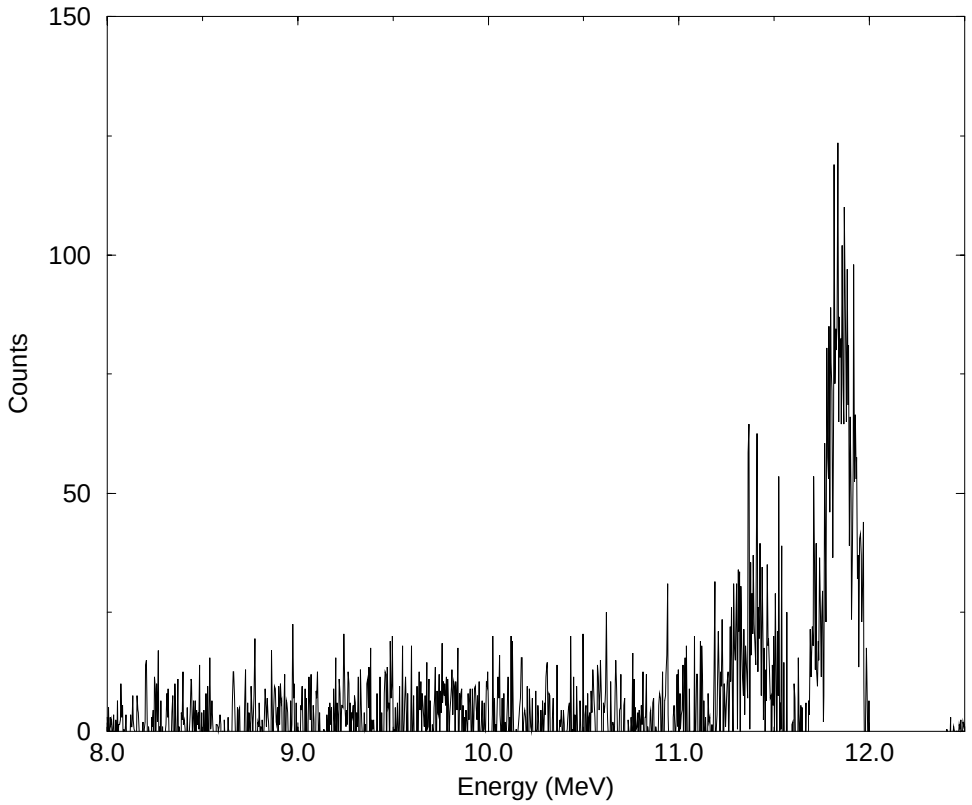

Figure 3.8: First escape peak spectrum for 12.2 MeV γ-rays.

3.2.5 Polarization Measurement

Because the OK-4 has a planar undulator, the FEL photons will always be 100% linearly polarized with the electric field vector parallel with the floor of the FEL facility. The Klein-Nishina formula can show that, for small angles, the backscattered γ-rays will maintain the degree and direction of polarization of the incident FEL photons (see Section 2.3.3).

The polarization of the FEL photons was measured using a polarizing film. The

ratio of light intensities when the polarization axis of the film was parallel and perpendicular to the floor confirmed that the FEL light was 100% linearly polarized in the horizontal plane. Compton scattered γ-rays are expected to have the same polarization qualities, but unfortunately this can not be measured with a simple polarizing film. Instead, the polarization of the γ-ray beam was inferred from the neutron scattering asymmetry in the $^2\mathrm{H}(\vec{\gamma},\mathrm{n})\mathrm{p}$ reaction. Previous measurements undertaken at a similar facility [Bia81] indicated that neutrons produced at a center of mass angle of 90° by 100% linearly polarized γ-rays would have an asymmetry of 0.95 ± 0.02.

Detector Apparatus

The polarization measurement was taken using a scintillating C_6D_{12} target and two BC501 neutron detectors. The active target was a 4 cm×6 cm cylinder with its symmetry axis perpendicular to the beam axis. A "good" photodisintegration event would result in a neutron leaving the target and a proton depositing its recoil energy in the scintillator, providing a signal with which to "tag" good events in the neutron detectors. The neutron detectors had active areas of 132.7 cm^2 and were placed 23 cm from the center of the scintillating target. One detector was placed in the horizontal plane, and the other was placed in the vertical plane directly above the active target, as shown in Figure 3.9. The two detectors spent equal time in the horizontal and vertical positions to keep small differences in detector response and efficiency from affecting the asymmetry measurement. Pulse shape discrimination techniques were used to separate neutron events in the detector from γ-ray events (pulse shape discrimination is discussed in detail in Section 5.1). Neutron events were further separated by measuring the time of flight of the neutrons by recording the time between the proton recoil signal in the active target and the neutron signal

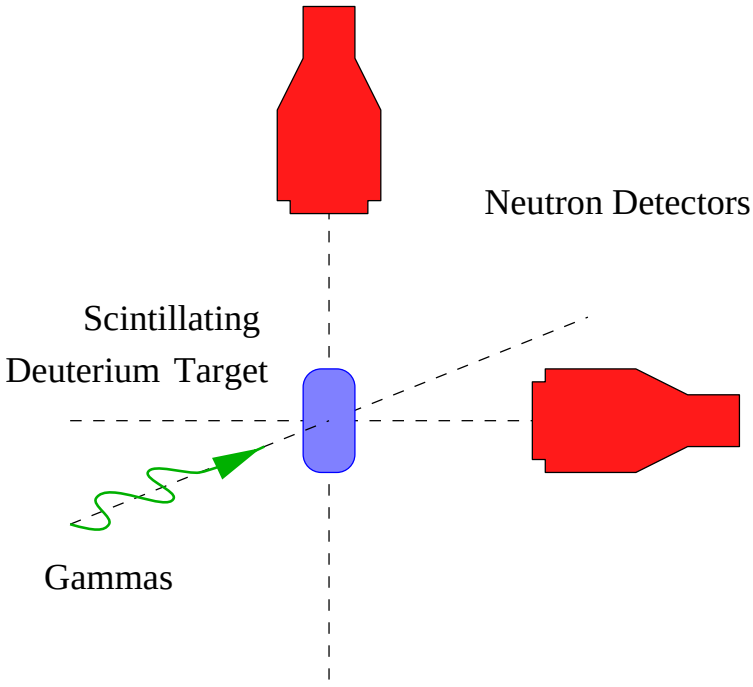

Figure 3.9: Detector setup for γ-ray polarization measurement.

in the BC501 detectors. The 5 MeV neutrons produced in this measurement have an average time of flight of 7.4 ns, which can be easily distinguished from the γ-ray events, all of which have a time of flight of less than 1 ns. Finally, software gates set in the active target energy spectrum selected signals of energy consistent with proton recoil, reducing possible background events from Compton scattering.

Measurement Results

A typical neutron time of flight spectrum is shown in Figure 3.10. These spectra were combined with pulse-height spectra to form two-dimensional distributions in which the neutron counts are well separated from the scattered γ-rays. This measurement indicates a neutron asymmetry of 0.82 ± 0.05. Because the detectors cover a

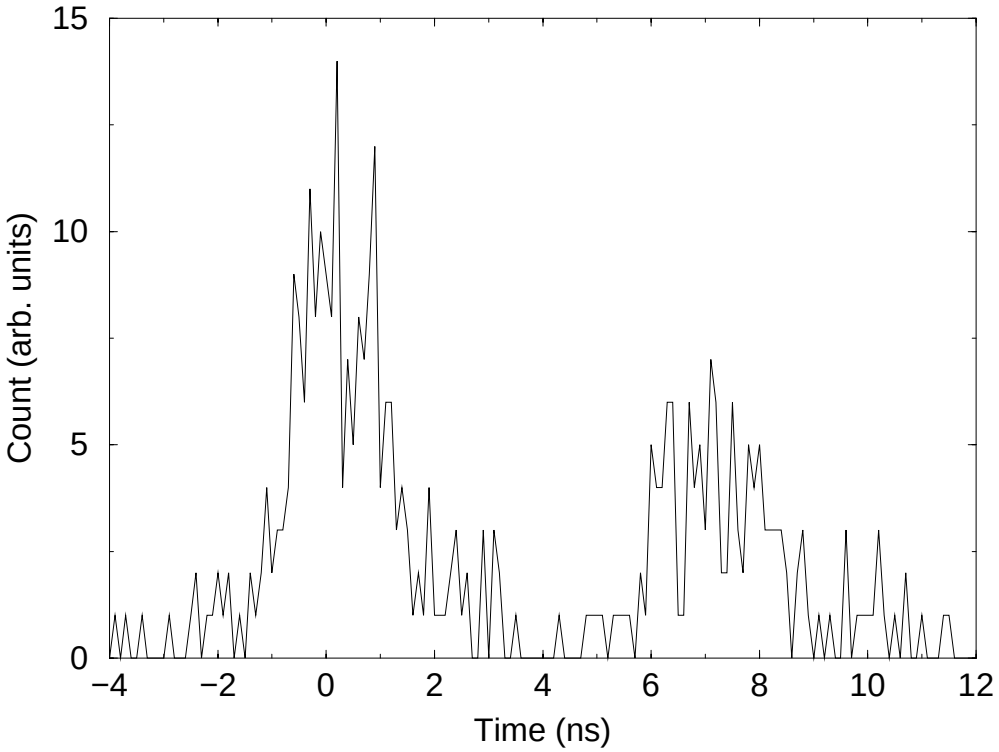

Figure 3.10: Time of flight spectrum from polarization measurement. This spectrum represents a single detector in the horizontal plane. Time runs from left to right, so the neutron peak is the right peak. The time scale has been shifted to define zero as the center of the γ-ray peak.

large solid angle around $\theta = 90°$, the measured asymmetry was lower than we would expect from point detectors placed at 90°. Correcting for this finite geometry by integrating over the detector geometry provides an asymmetry of 0.88 ± 0.05 [How96]. Multiple scattering of neutrons within the C_6D_{12} target can also make the asymmetry appear lower than it is. A first-order correction for the effect of multiple scattering gives a final result of 0.93 ± 0.06 [How96]. A more precise calculation of corrections for finite geometry and multiple scattering is discussed in Section 6.2. The result of these preliminary calculations is in good agreement with previously measured value of 0.95 ± 0.02 [Bia81], and is consistent with a γ-ray linear polarization of 100%.

Quantity	Expected	Observed
Flux	$2.0 \times 10^5 \gamma/s$	$2.6 \times 10^5 \gamma/sec$
Energy Resolution	1.2%	$\sim 1.25\%$
Polarization Asymmetry in Deuteron Polarimeter	0.95 ± 0.02	0.93 ± 0.06

Table 3.2: Comparison of predicted and measured γ-ray characteristics

3.2.6 Summary of Initial Measurements

The measurements reported in this section indicate that the performance of the HIGS facility is in good agreement with expectations calculated using the techniques described in Chapter 2. A comparison of calculated and measured γ-ray properties is shown in Table 3.2.

3.3 Subsequent γ-ray Measurements

Additional measurements of the properties of γ-rays produced by this facility were made in the Fall of 1998. These measurements demonstrated an extended range of operation, using higher energy electron beams and different FEL photon energies made possible by the installation of a new optical cavity. These γ-ray properties were observed using the detector systems mentioned previously, as well as an electron-positron pair spectrometer.

3.3.1 Extended Range of Operation

Low γ-ray energies were achieved by operating the storage ring at energies below 500 MeV. One consequence of a lower electron energy is a wider angular distribution

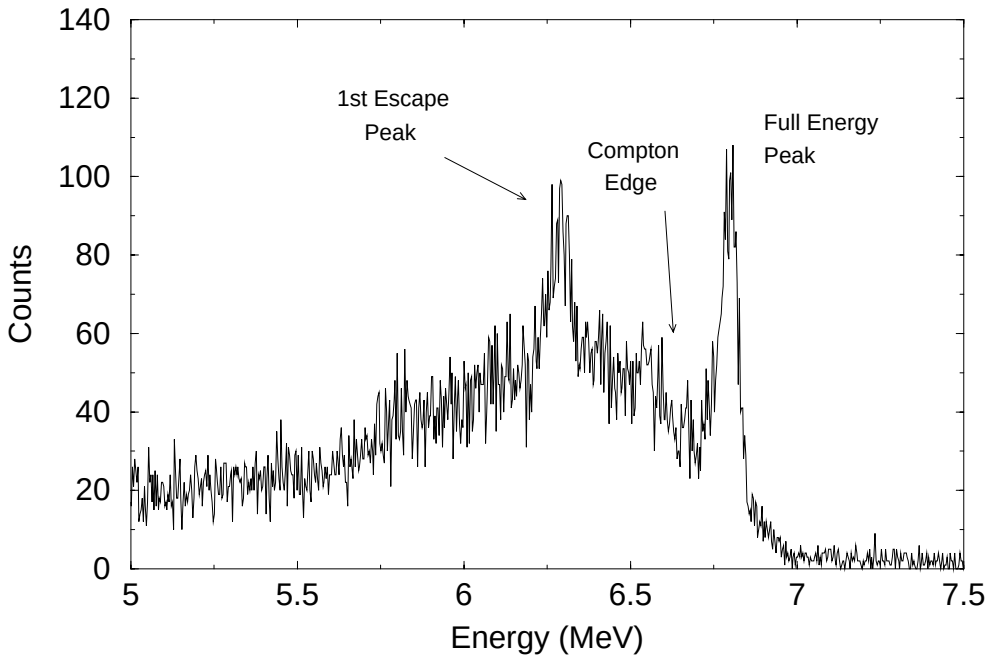

Figure 3.11: Low-energy γ-ray spectrum. This distribution was generated by scattering 243 nm (5.10 eV) FEL photons off of 300 MeV electrons. The distribution, viewed through a 3 mm diameter collimator, has a FWHM of 0.78%.

for the γ-rays, since most of the γ-rays are projected into a cone with a divergence angle of $\sim 1/\gamma$. Because a wider angular distribution implies a larger change in γ-ray energy for a given angular change, a given collimator will allow a smaller range of γ-ray energies through at lower electron energies. The lowest energy resolution observed during these measurements came from 6.58 MeV γ-rays passing through a 3 mm diameter collimator. The resulting spectrum, taken with a HPGe detector, showed a full-width half-max (FWHM) energy resolution of $\Delta E/E = 0.78\%$ for the full energy peak in the detector response function. This spectra is shown in Figure 3.11. More recently, energy resolutions as low as 0.46% have been observed [Par00].

Further lowering of the electron energy allows the production of even lower γ-ray energies. The lowest observed γ-ray energy was generated by scattering 380 nm FEL photons from 240 MeV electrons, producing a γ-ray energy of 2.85 MeV. Because 240

MeV is at the bottom of the operating range for the Duke facility, instabilities in the beam made operations difficult, and fluxes at this energy were limited to 50 Hz. This flux was generated with 7.5 mA of current in the storage ring.

The beam was more stable at a slightly higher energy. The $^2\mathrm{H}(\vec{\gamma},\mathrm{n})\mathrm{p}$ measurement in Chapter 5 used 3.58 MeV γ-rays generated by scattering 382.5 nm light off of 270 MeV electrons. Although the $^2\mathrm{H}(\vec{\gamma},\mathrm{n})\mathrm{p}$ experiment used a large aperture collimator, a high-resolution measurement of this beam was taken by using a 3 mm diameter collimator. The resulting energy distribution, shown in Figure 3.12, shows a FWHM of 1.2%, or 43 keV. Because the energy width of the photopeak is smaller than the minimum energy of a Compton scattered γ-ray in the HPGe detector, the photopeak is well separated from the Compton edge. This allows a direct observation of part of the expected low energy tail of the γ-ray distribution.

Fluxes as high as $1.2 \times 10^4 \gamma$'s/sec were observed with approximately 10 mA of electron beam in the storage ring. Operating the storage ring at 270 MeV removed the necessity of injecting electrons into the ring at a lower energy and slowly ramping the energy to the value desired for a given experiment. Because the linac can inject electrons into the ring at 270 MeV, the ring could be continuously filled during γ-ray operation. This allowed the replacement of electrons scattered from the beam, and could therefore maintain the current in the ring indefinitely. The γ-ray flux listed above was maintained for several hours at a time without a significant drop in count rate.

Operating at higher electron beam energies allows the creation of γ-rays with energies up to 55 MeV. Gamma-rays having maximum energies of 35 MeV (by scattering 249 nm (4.98 eV) FEL photons off of 700 MeV electrons) and 58 MeV (by scattering 193 nm (6.42 eV) FEL photons off of 800 MeV electrons) were observed

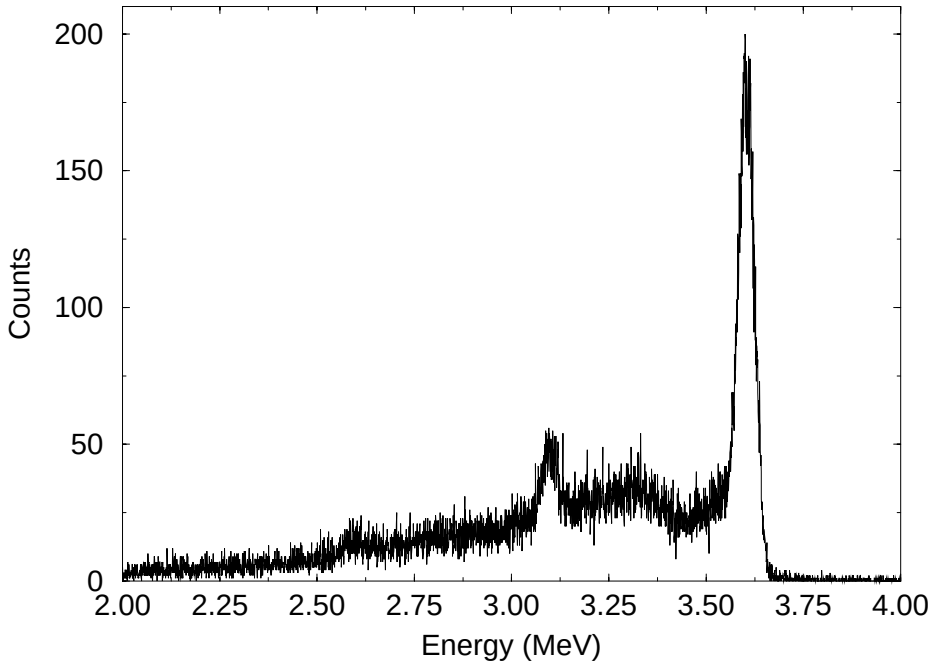

Figure 3.12: Low-energy γ-rays generated from 382 nm (3.2 eV) FEL photons and 270 MeV electrons using a 3 mm diameter collimator. The low energy tail of the γ-ray distribution is visible through the detector response.

during this set of measurements.

3.3.2 Pair Spectrometer

All the γ-ray measurements documented in this chapter were made by utilizing the same technique: stopping the γ-ray beam in a detector and recording spectra of the deposited energy. This technique has several limitations. One limitation arises from the characteristics of the available detectors themselves. A second limitation is that placing the detectors in the beam path stops the beam, so experiments can not be run while simultaneously monitoring the γ-ray beam. A third difficulty arises from the fact that neither NaI nor HPGe detectors can successfully count at rates higher than $10^4\gamma$'s/sec.

To address these difficulties, an electron-positron pair spectrometer was developed. A pair spectrometer consists of three basic parts: a converter foil to convert some percentage of incident γ-rays into electron-positron pairs, a magnetic field region to separate the electrons and positrons and bend them along curved paths, and a position sensitive detector array to detect the degree of bending experienced by the charged particles. Because the degree of bending is proportional to the momenta of the particles, the electron and positron energies can be determined and summed to determine the energy of the initial γ-ray. In addition, if a converter foil of known composition and thickness is used, then the percentage of incident γ-rays that will produce electron-positron pairs can be calculated, and the incident flux of γ-rays can be determined.

The simplest configuration for a pair spectrometer would be to have the converter foil and detector arrays along a line all inside a large uniform magnetic field region. The charged particles would then follow a semicircular trajectory, and their energies could be easily computed by measuring the distance between the point of impact with the detector plane and the converter foil. For most applications, however, this configuration is problematic. The high cost of producing a large enough uniform magnetic field and getting detectors to operate reliably within that field make spectrometers of this design impractical. Additionally, this configuration only works for charged particle trajectories that are perpendicular to the line defined by the converter and the detector array.

A circular dipole magnet can also be used for this purpose [Bro56]. Using a circular magnetic field region has the advantage that the curved entry and exit regions of the field have a focusing effect on the charged particles. This means that charged particles that are created at the same position with the same energy but with different

initial trajectories with respect to the direction of γ-ray propagation will be focused to a single spot. The location of the image formed by this magnetic lens effect can be determined from geometrical arguments. Barber's Rule [Bar33] states that, for a uniform circular field, the object point, the center of curvature, and the image point lie in a straight line if the object point is located at a distance equal to two radii of the field region from the center of the field. The radius of curvature can be simply determined from the Lorentz Force Law, giving $r = |p|/qB$, where p is the particle momentum, q is the charge, and B is the magnetic field strength. Because particles with different momenta will have a different center of curvature, they will also have different image locations. The locus of image locations as a function of particle momenta forms a hyperbola. For a limited range of particle momenta, this hyperbola can be approximated by a line, often used to define the focal plane of the magnet. The relations between particle momenta and focal plane position are derived in Appendix A.

A dipole magnet for which the pole separation is much less than the pole radius produces an extremely uniform field between the poles. However, outside this region, the field gradually drops to zero with increasing radius. These fringe fields deflect the charged particles along a trajectory inconsistent with the uniform field assumptions made above. However, a circular dipole field can be treated as a completely uniform field region with some effective field radius (EFR) with no field amplitude outside this radius. This EFR is always larger than the radius of the poles themselves. It has been shown [Liv69] that this approximation is valid if the EFR is defined as shown in Figure 3.13.

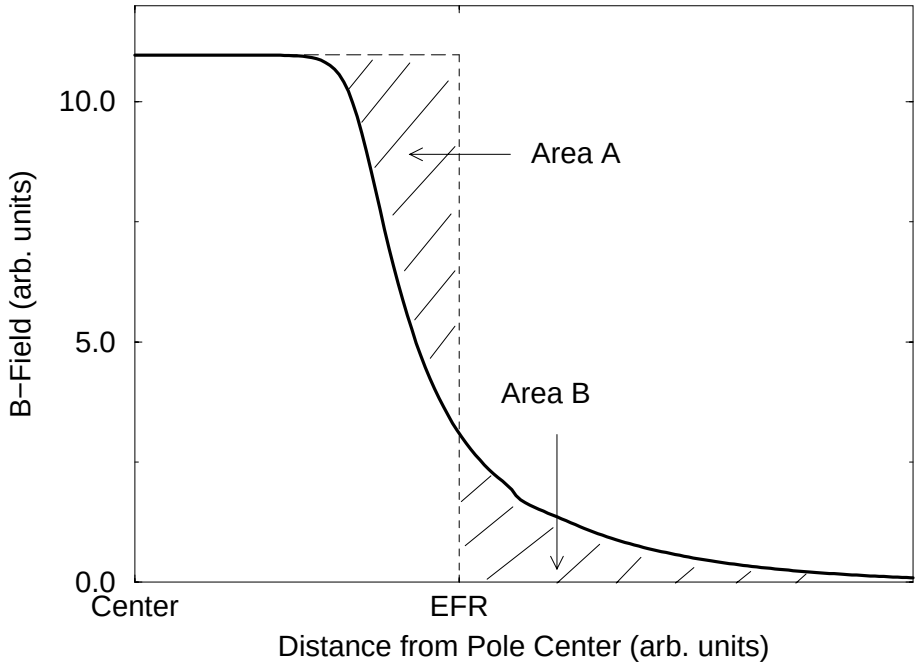

Figure 3.13: Definition of effective field radius (EFR). The EFR is defined as that distance from the center of the magnetic field region for which Area A=Area B.

Apparatus

The pair spectrometer used in these measurements was acquired from the Saskatchewan Accelerator Laboratory (SAL) [Sig94]. The properties of the magnet are shown in Table 3.3, and the apparatus is shown in Figure 3.14. The upstream edges of the triangular vacuum chamber define the position of the detectors in the focal plane. The position-sensitive detector array consists of two sets of 16 NE110 plastic scintillators. The detectors are 25 mm×50 mm×3.2 mm in size, and are mounted side by side to form two 50 mm×400 mm detector planes. Each detector is connected to a Hamamatsu R1450 photomultiplier tube (PMT).

The signals from the PMTs are analyzed in the electronics setup shown in Figure 3.15. The linear signals from right and left side detector arrays are sent into constant

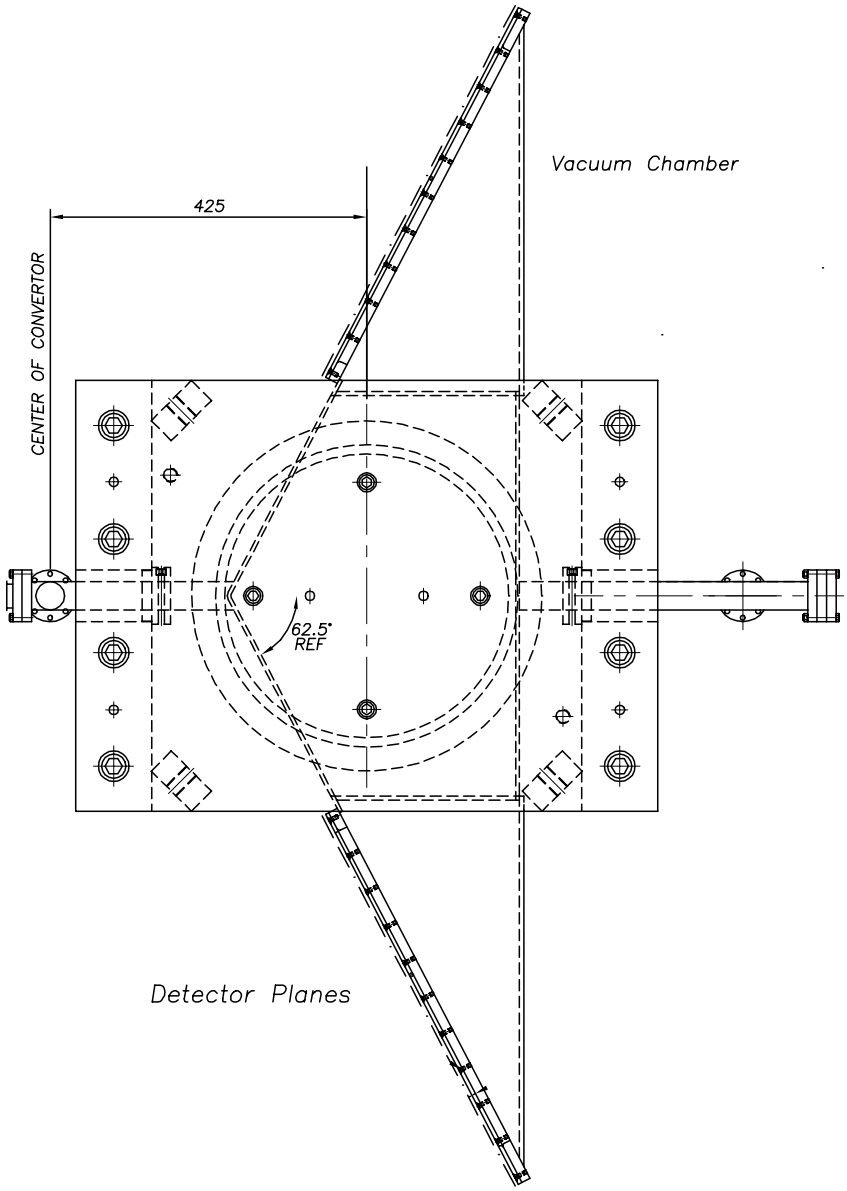

Figure 3.14: The SAL Pair Spectrometer. The yoke is 78×58 cm. The pole tips have a radius of 20 cm.

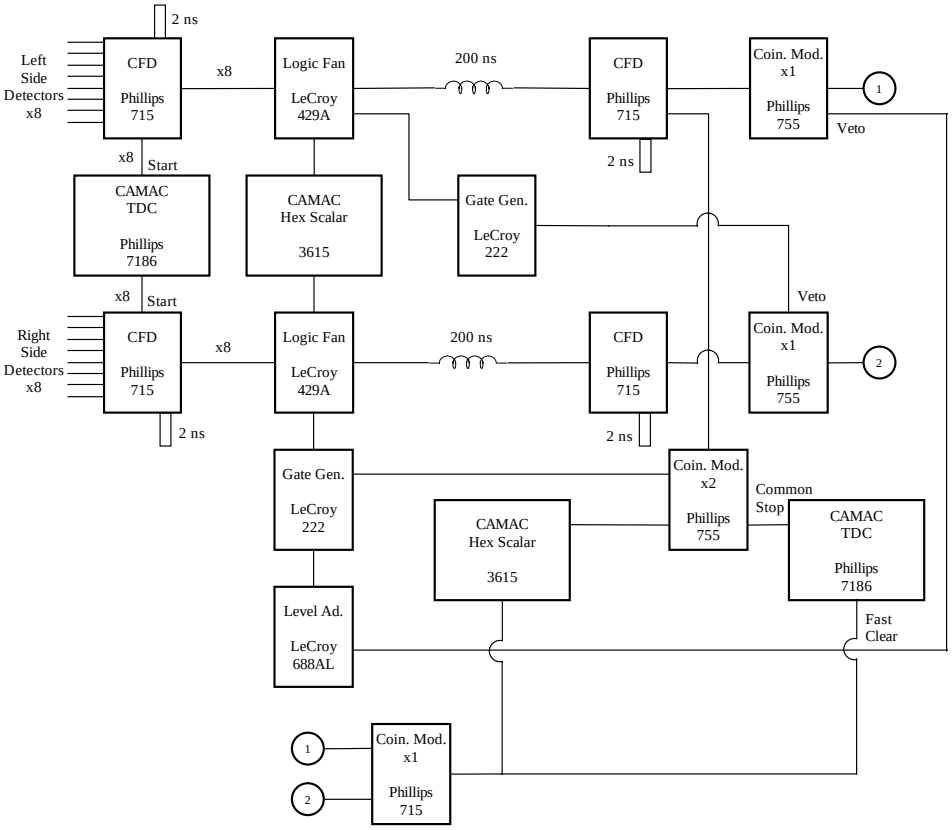

Figure 3.15: Electronics setup for the pair spectrometer.

Magnet	Value
Pole Radius	20 cm
Effective Field Radius	22 cm
Pole Gap	5 cm
Maximum Current	350 A
Resistance of Coils	0.11 Ω
Maximum B-Field	1.2 T

Table 3.3: Characteristics of the SAL pair spectrometer magnet. These values are taken from [Sig94].

fraction discriminators (CFD). The NIM output from each CFD is sent as a start signal to one channel of the 16 channel Phillips 7186 CAMAC time-to-digital converter (TDC). The NIM signals are then sent through LeCroy 429A logic fans that act as a logical AND for the signals, producing one NIM signal for each side of the detector. The signals are then checked to make certain that charged particles were detected in both the right and left side detector arrays. This coincidence is checked in a Phillips 755 logic module. If both signals are present, the NIM output from the logic module is sent to the TDC as a stop for all channels. Only the TDC channels corresponding to detectors that were hit by a charged particle will register any value. If there is no coincidence in the logic module, then no stop signal will be sent, and the TDC will time out after 400 ns, recording no signals. If the system is running with large count rates, this 400 ns delay and further reset time is undesirable, so a fast clear circuit is set up to quickly reset the TDC in the event of a failed coincidence. In this circuit, each logic signal, corresponding to the left and right side detector arrays, is delayed and sent through a Phillips 755 logic module that acts as a logic gate. This gate is vetoed by a long logic signal originating from the detector array on the opposite side. Thus, a signal will only get though the logic module if no detectors in the other array fired. These gate signals are sent through another logic module acting as a logical

Detector	Kinetic Energy (MeV)	Acceptance(MeV)
1	16.571	±0.150
2	16.862	±0.140
3	17.132	±0.130
4	17.387	±0.124
5	17.625	±0.115
6	17.847	±0.107
7	18.056	±0.101
8	18.252	±0.095

Table 3.4: Kinetic energy range for each detector in the PS array during the Fall 1998 run. Detector 1 is the innermost detector in the active portion of the array. These values correspond to a magnetic field strength of 0.2297 T.

OR, and the resulting NIM signal is sent to the TDC as a fast clear. A CAMAC hex scalar module records the number of events in the left and right detector arrays, the number of coincidences, and the number of fast clears sent by the electronics. All of this information is analyzed using the TUNL XSYS data acquisition system.

Preliminary Measurements

Preliminary tests of the SAL pair spectrometer were performed in Fall 1998. The pair spectrometer was used to detect a γ-ray distribution having a peak energy of 35.5 MeV. Limitations in the available electronics allowed only eight detectors from each array to be used. To maximize the energy acceptance of the array, the outer eight detectors of each detector array were chosen. Using the equations derived in Appendix A, the energy acceptance for each detector assuming a magnetic field strength of 0.2297 T is given in Table 3.4. The energy of the initial γ-ray is determined by summing the kinetic energies measured by each detector pair of the array and adding the result to the combined rest masses of the electron and the positron (m_e+m_p=1.022 MeV).

The energy of the incident γ-ray is not necessarily evenly distributed between the electron and the positron. The theoretical expression for the differential cross section with respect to energy can be found in [Bet53]. For γ-ray energies near 35 MeV, the probability of the electron having a given percentage of the available energy is roughly constant between 15% and 85% of the total energy, with the probability gradually dropping to zero for $E_e = 0\%$ or 100%. Most of the electrons will therefore be distributed roughly evenly between 5 and 30 MeV. Because the detector arrays only cover a range of 1.93 MeV, only a small percentage of the electron-positron pairs would be produced within the energy acceptance of the detectors.

This limitation requires that a relatively thick converter be used to produce as many electron-positron pairs per incident γ-ray as possible. A 0.1 mm thick tantalum foil was therefore selected as the converter. Approximately 1% of the incident 35.5 MeV γ-rays will be converted using this foil. Using a thick converter has the disadvantage of scattering the electrons and positrons as they pass through the remainder of the foil. A numerical calculation of the radiative and collision losses of the electrons and positrons was performed using the formulae for electron bremsstrahlung and the Bethe-Bloch formula for electrons and positrons [Leo94] (See Appendix B). The calculation indicated that 17 MeV charged particles generated near the beginning of the foil would lose 400 keV and 240 keV from radiative and collision losses, respectively. Particles generated in the middle or near the exit of the foil will lose less energy, indicating that the final energy distribution of the charged particles could be shifted downwards by anywhere from zero to 640 keV. Because this range is a significant fraction of the energy acceptance of the spectrometer, a high resolution measurement of the γ-ray distribution would be difficult. This problem can eventually be overcome by increasing the γ-ray flux, allowing the use of a much thinner converter foil.

8	46	30	33	30	17	16	8	6
7	30	27	28	24	15	16	10	6
6	28	30	31	24	12	13	13	13
5	38	44	35	40	29	25	19	21
4	31	30	30	21	34	30	22	15
3	44	45	32	40	34	39	33	31
2	33	38	30	34	33	41	28	28
1	32	29	34	43	23	37	24	31
Detectors	1	2	3	4	5	6	7	8

Table 3.5: Data set from a sample pair spectrometer run.

A sample data set for $B = 0.2297$ T is shown in Table 3.5. These data were collected during a 43 minute experiment with an initial beam current of 7.12 mA in the storage ring. The numbers in Table 3.5 represent the total number of coincidence events between specific detectors on the right and left side. Because a coincidence event between detectors 4 and 5 corresponds to approximately the same γ-ray energy as a coincidence between detectors 3 and 6 or detectors 2 and 7, the data in Table 3.5 can be rewritten in terms of 15 discrete energies, each corresponding to a set of detector coincidences that lie along a diagonal on the data table (for example, one diagonal contains the detector pairs 4 and 1, 3 and 2, 2 and 3, and 1 and 4, which corresponds to a γ-ray energy range of 33.98 ± 0.39 MeV.) Each of these diagonals can be represented as a Gaussian distribution with the standard deviation equal to the energy range.

Because of the wide range of possible energy distributions between the electron and the positron, all diagonals do not subtend the same amount of the available energy acceptance. The diagonal corresponding to the coincidence between detectors 1 and 1, for example, will only occur when the electron and positron from a 33.14 MeV γ-ray have energies with 1.8% of the centroid energy, whereas coincidences in

the diagonal corresponding to detectors 1 and 2 and detectors 2 and 1 will occur when the charged particles from a 33.43 MeV γ-ray have energies within 3.5% of the centroid. The Gaussian for each diagonal therefore have to be normalized to account for this difference in available energy acceptance.

Performing this normalization and adding the 15 Gaussian together produces the energy spectrum shown in Figure 3.16. The energy resolution is in rough agreement ($\sim$ 10%) with a spectrum taken with a NaI detector, although the exact width is difficult to determine, because the width of the distribution is larger than the energy acceptance of the spectrometer. The gradual slope of the high-energy fall-off of the spectrum is a consequence of the electron-positron energy straggling in the tantalum foil.

By tuning the magnetic field strength, the spectrometer energy acceptance varied to cover different parts of the γ-ray energy distribution. Low statistics prevented these different spectra from being combined into a full energy distribution.

Future Directions

The spectra described above represent an initial test of the SAL pair spectrometer at the HIGS facility. The spectrum shown in Figure 3.16 does not provide a good description of the real γ-ray distribution. The performance of the pair spectrometer can be improved in several ways. First, a higher γ-ray flux would provide better statistics, as well as allow the use of a thinner converter foil which reduces the spread in electron-positron energies. Second, the effectiveness of the pair spectrometer increases for higher energy γ-rays because the cross section for pair production increases with γ-ray energy. This allows the use of a thinner converter foil, and also projects the charged particles into a more narrow distribution[Bet53]. Finally, the inclusion of

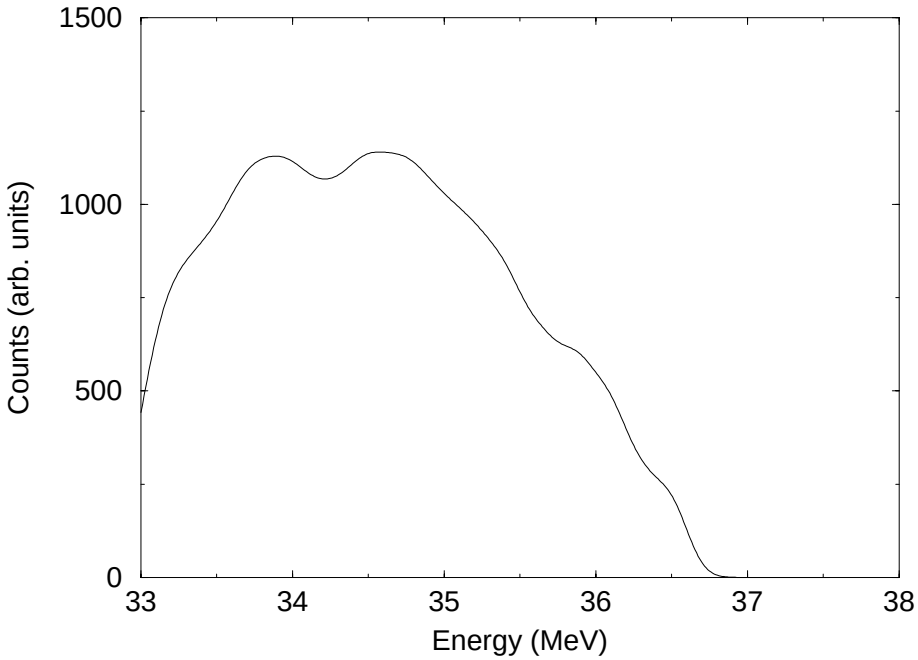

Figure 3.16: Data from Table 3.5 represented as a series of overlapping Gaussians. The distribution is not valid below about 33.5 MeV, since γ-rays with less energy are outside the energy acceptance of the spectrometer.

all 32 detectors would give the spectrometer a larger energy acceptance and allow an entire γ-ray distribution to be viewed. Additionally, the efficiency for detecting a single γ-ray energy would increase, because the available electron-positron energy phase space corresponding to a given γ-ray energy would approximately double.

A planned improvement to the detector arrays involves replacing the plastic scintillators with a series of position-sensitive silicon detectors. These detectors will measure position with a resolution of better than 1 mm, which is a substantial improvement over the 25 mm resolution of the plastic scintillators. This improvement will allow a much finer resolution of Gaussians to be added together, and will reduce the "lumpiness" seen in Figure 3.16.

Chapter 4

$^2\mathrm{H}(\vec{\gamma},\mathrm{n})\mathrm{p}$ at $\mathbf{E_\gamma}$=3.58 MeV : Theory

The first theoretical treatment of deuteron photodisintegration [Bet35] was published within a year of Chadwick and Goldhaber's initial $d(\gamma, n)$ measurement [Cha34]. Since then, there have been numerous theoretical treatments of the n-p system, and the comparison of these theories with experimental results has provided a great deal of insight into nucleon-nucleon interactions, which have played a major role in the construction of several realistic models of the nuclear strong force. The lack of experimental data in the energy region of interest to this dissertation, as described in Section 1.5.1, makes it difficult to test the different methods of calculating the $^2\mathrm{H}(\vec{\gamma},\mathrm{n})\mathrm{p}$ cross section against one another. Many of these calculations involve a direct solution of the two-body Schrödinger equation [Are99, Sat95]. Other recent calculations [Che99b, Rup99] use effective-field theory techniques to perturbatively calculate the electric and magnetic contributions to the cross section in this energy region.

4.1 Direct Calculation

The Schrödinger equation can be solved exactly for two-body systems. For the n-p system, exact calculations for both bound and continuum states are possible. Many theoretical studies of deuteron photodisintegration and n-p radiative capture have used this method to determine the properties of the n-p system. We focus on two such studies below [Are99, Sat95].

The differential cross section for deuteron photodisintegration in the center of mass (CM) frame can be expressed as [Are91]

$$\frac{d\sigma}{d\Omega} = \frac{(2\pi)^{10}}{(4W)^2}\frac{k}{\omega}\left|T_{fi}\right|^2, \tag{4.1}$$

where W is the total CM energy, k is the outgoing nucleon momentum (in the CM frame, the other nucleon has a momentum of $-k$), and ω is the momentum of the incident photon. The physics of the interaction is described by the transition matrix elements (TMEs) contained in the T-matrix, which is defined as $T_{fi} = \langle \Psi_f \left| H_\gamma \right| \Psi_i \rangle$. The wavefunctions Ψ_i and Ψ_f describe the initial and final states of the reaction, and the transition between the states is defined by the interaction Hamiltonian H_γ.

For deuteron photodisintegration, the interaction Hamiltonian is just the electromagnetic current operator given in Equation 1.2. This operator is most easily considered by expanding it in terms of electric and magnetic multipole operators. These operators can be written as [Are91]

$$T^{[L]}_{e/m} = \int d^3x \boldsymbol{j}(\boldsymbol{x}) \cdot \boldsymbol{A}^{[L]}(e/m), \tag{4.2}$$

where L is the order of the particular multipole, $\boldsymbol{j}(\boldsymbol{x})$ is the current density, and $\boldsymbol{A}(e/m)$ represent the electric (e) and magnetic (m) multipole fields. The multipole

fields can be expressed in terms of spherical harmonics and current densities:

$$\boldsymbol{A}^{[L]}(m) = -\frac{i^{L+1}}{\sqrt{L(L+1)}}\left(\boldsymbol{r}\times\nabla\right) j_L(\omega r) Y^{[L]}, \tag{4.3}$$

$$\boldsymbol{A}^{[L]}(e) = \frac{i}{\omega}\nabla\times\boldsymbol{A}^{[L]}(m). \tag{4.4}$$

The T-matrix can therefore be completely determined by calculating the current densities corresponding to a given multipole field. The current density is defined by the principle of current conservation, which states

$$\nabla\cdot\boldsymbol{j}(\boldsymbol{x}) + i\left[H_N, \rho(\boldsymbol{x})\right] = 0. \tag{4.5}$$

The nuclear interaction Hamiltonian H_N can be separated into kinetic and potential operators such that $H_N = T_N + V_N$. Separating Equation 4.5 into one- and two-body components gives

$$\nabla\cdot\boldsymbol{j}_{(1)}(\boldsymbol{x}) + i\left[T_N, \rho_{(1)}(\boldsymbol{x})\right] = 0 \tag{4.6}$$

$$\nabla\cdot\boldsymbol{j}_{(2)}(\boldsymbol{x}) + i\left[T_N, \hat{\rho}_{(2)}(\boldsymbol{x})\right] + i\left[V_N, \rho_{(1)}(\boldsymbol{x})\right] = 0 \tag{4.7}$$

The form of the nuclear current densities therefore depends on the specific model used for the nucleon-nucleon interaction.

For low energy ($E_\gamma < 10 - 20$ MeV) processes in which the electric dipole (E1) amplitude dominates, the calculation of the TME is simplified by noting that the interaction between the outgoing proton and neutron is described by p-wave interaction. Because the p-wave part of the NN force is relatively weak, the final-state wavefunction Ψ_f can be treated as a plane wave [But68]. For processes involving other electromagnetic multipoles, a more complicated form for Ψ_f is required.

4.1.1 Nucleon-Nucleon Potentials

Nucleon-nucleon (NN) interactions are governed by the strong force. The strong force has a complicated structure, and consequently the various interaction models can differ significantly. All potential models, however, share some basic characteristics. At short ranges (< 0.5 fm), the potential is repulsive. Long range interactions (> 2 fm) are attractive and are governed by the exchange of a single pion. The intermediate region is more complicated, and can be modeled by the exchange of multiple pions and heavier particles such as ρ and ω mesons. This intermediate range is the least well understood of the three, and is where the various NN potential models differ.

A given potential model is generated by selecting the physical processes to be included in the interaction. These processes are characterized by free parameters such as interaction coupling constants and particle masses. The free parameters are varied until the predictions of the NN potential match the available *np* and *pp* scattering data. The large body of *np* and *pp* scattering data that has been accumulated over the last half century provides very strong constraints for any potential model [Car98]. In some potentials, particle masses are treated as free parameters even for particles for which the mass is well known. This leads to potentials that reproduce two-body scattering data extremely well and demonstrate good predictive abilities, but have a questionable physical basis.

Bonn-OBEPR

Recent calculations by Arenhövel [Are91, Are99] have used the Bonn-OBEPR potential to determine the $^2\mathrm{H}(\vec{\gamma},\mathrm{n})\mathrm{p}$ cross section in the near-threshold energy region. The Bonn-OBEPR (One Boson Exchange Potential in position (R) space)

potential is an adaptation of the "full" Bonn potential [Mac87] in which processes involving energy dependence and multiple meson exchange are excluded. Restricting the calculation to single meson exchange processes greatly simplifies the application of the potential. The nucleons are allowed to interact through the exchange of single π, η, ρ, ω, and δ mesons, in order of increasing mass and decreasing effective range. However, because the contributions of 2π and $\pi\rho$ exchange interactions were found to make significant contributions to the "full" Bonn potential, these interactions are represented by including the exchange of a fictitious σ boson.

Several additional processes are included with the Bonn-OBEPR potential. The exchange of charged mesons between nucleons are referred to as Meson Exchange Currents (MECs). In the ^{2}H$(\vec{\gamma}, \mathrm{n})$p reaction, this process effectively exchanges the relative positions of the proton and the neutron. The critical role of MECs was first discovered when the inclusion of MECs in the theory successfully accounted for large discrepancies between theory and experiment in the the thermal neutron capture cross section of the $p(n, \gamma)d$ reaction [Ris72]. The explicit addition of MECs to the magnetic dipole (M1) terms of the cross section was sufficient to increase the total cross section by the observed 10%. For low energies, MECs have a minimal effect on electric dipole (E1) contribution to the cross section. This can be seen by invoking Siegert's theorem in the low-energy limit [Sie37], which allows the operator for electric multipole fields to be separated into a charge density term and a current density term. At low energies, the charge density term is dominant [Are91], minimizing the contribution of the current density term which contains the MEC effects. Siegert's theorem can not be applied to M1 radiation, however, so MEC effects must be explicitly added to the M1 operator. Because the ^{2}H$(\vec{\gamma}, \mathrm{n})$p reaction has a significant M1 contribution at the energy of interest to this dissertation, as described in Section 1.5.1, the inclusion of

MECs can significantly affect the total cross section.

The contributions of isobar configurations have also been explicitly added to the potential for these calculations. The inclusion of isobar configurations reflects the contribution of the internal nucleon degrees of freedom. This can affect the NN interaction when some of the energy of the exchange meson excites a resonance in one or both of the nucleons. Because the lowest-lying πN resonance, the Δ isobar, has a mass of 1232 MeV (approximately 300 MeV greater than the rest mass of the original nucleon), these configurations are only possible for higher energy π-mesons. The isobar configurations therefore most directly affect the NN interaction in intermediate and short ranges. Although the Δ resonance is centered at an energy much higher than that considered in the present experiment, the tail of the Δ resonance can have an effect on the cross section at low energies. This merits the inclusion of these effects in the present calculation.

The final adjustment to Arenhövel's calculation is the inclusion of relativistic effects. Historically, relativistic effects have been considered unimportant for reactions below pion threshold (135 MeV) [Are91]. More recently, the importance of relativistic corrections to the spin-orbit interaction in $^2\mathrm{H}(\vec{\gamma},\mathrm{n})\mathrm{p}$ has been demonstrated at energies as low as 20 MeV [Cam82]. These effects therefore merit inclusion in calculations for lower energies. Relativistic corrections take several forms. The nucleon wave functions need to be modified to account for relativistic effects in the internal dynamics of the nucleon. The wave function must also be boosted to a moving frame, which can affect spin degrees of freedom and internal structure through Lorentz contraction. Finally, the current operator must be supplemented with extra terms to account for relativistic effects [Are91].

All of the above extra processes were included in Arenhövel's calculation. The

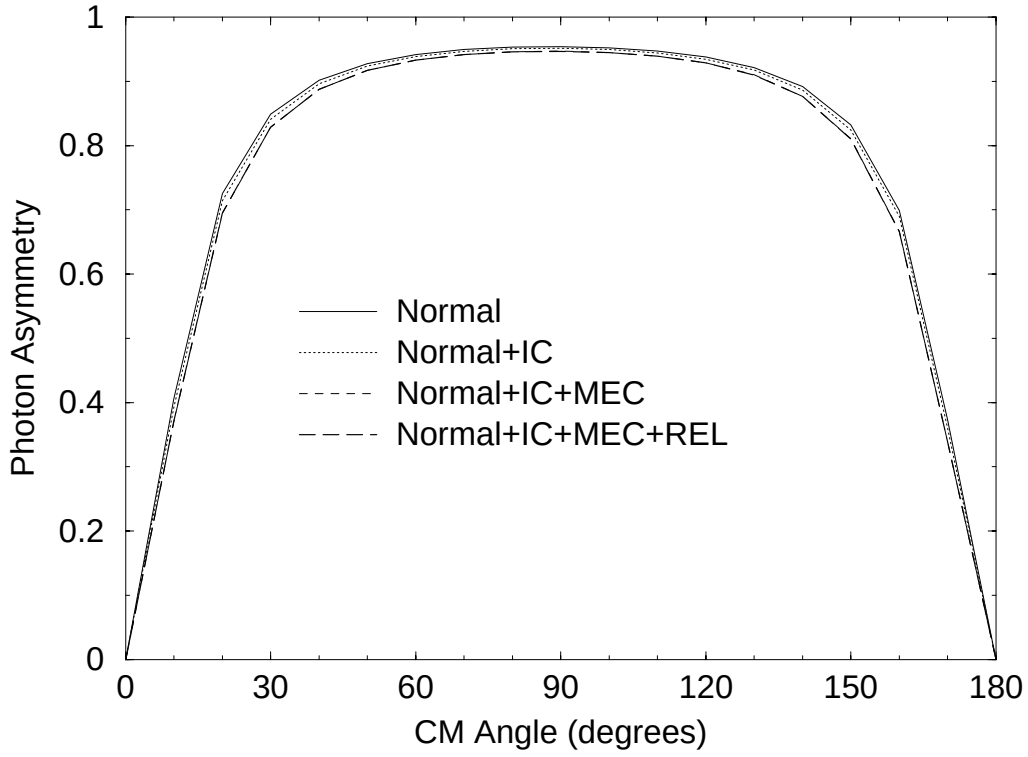

Figure 4.1: Photon asymmetry for deuteron photodisintegration with 3.58 MeV γ-rays. Normal refers to a simple non-relativistic approach, IC includes isobar configurations, MEC includes meson-exchange currents, and REL includes relativistic effects. Calculations taken from [Are99].

calculation was performed for the ^{2}H$(\vec{\gamma}, \mathrm{n})$p reaction assuming 3.58 MeV γ-rays. The results were found to be insensitive to the inclusion of these extra processes. The total cross section was found to vary less than 0.5% when these effects were included. The analyzing power for the reaction is equally insensitive to these effects, as shown in Figure 4.1. The results of the calculation will be further discussed and compared with experimental results in Section 6.3.

Argonne ν18

A separate set of calculations have been performed by Sato [Sat95]. These calculations used the Argonne ν18 (AV18) potential [Wir95] to calculate the $p(n,\gamma)d$ capture cross section in terms of the electric and magnetic dipole strengths. The n-p capture cross section can be related to the ^{2}H$(\vec{\gamma},\mathrm{n})$p cross section by the principle of detailed balance, as expressed in Equation 1.6.

AV18 is a state-of-the-art nonrelativistic potential that is fit to np, pp, and low energy nn scattering data, where nn scattering data is obtained by scattering low energy neutrons from deuterium. This is in contrast to most older potentials which are generally fit to either np data (such as Argonne ν14, Urbana ν14, and most Bonn Potentials) or pp data (such as Reid and Paris) [Wir95], usually leading to a poor description of the unfit data set. This discrepancy is the result of charge-independence breaking in the strong force, in which the np and pp interactions differ slightly. The AV18 potential is expressed in a 14 operator charge-independent part, as is the case for the Argonne ν14 potential, and charge-independence breaking part consisting of three charge dependent operators and one charge asymmetric operator [Wir95]. This allows the AV18 potential to be fit with excellent accuracy to both np and pp scattering data to 4301 data points between 0-350 MeV. The fit has a χ^2 of 1.09 per datum [Wir95]. The resulting potential does an excellent job of predicting physical parameters of the deuteron. Most of these predictions are similar to those calculated with the AV14 potential, with the most notable exception being that AV18 predicts a D-state percentage of the deuteron ground state that is 5% smaller than that predicted by AV14, indicating a weaker tensor component to the strong force [Wir95].

In addition to the basic AV18 potential, Sato's calculation included MECs, isobaric currents, and pair currents [Nag97]. The results of Sato's calculation are shown in Figure 4.2, along with several experimental data points measured in the region [Nag97]. For comparison, Sato repeated the calculation with a slightly modified version of the much older Reid potential [Rei68]. The resulting cross section calculation was almost identical to that calculated with AV18.

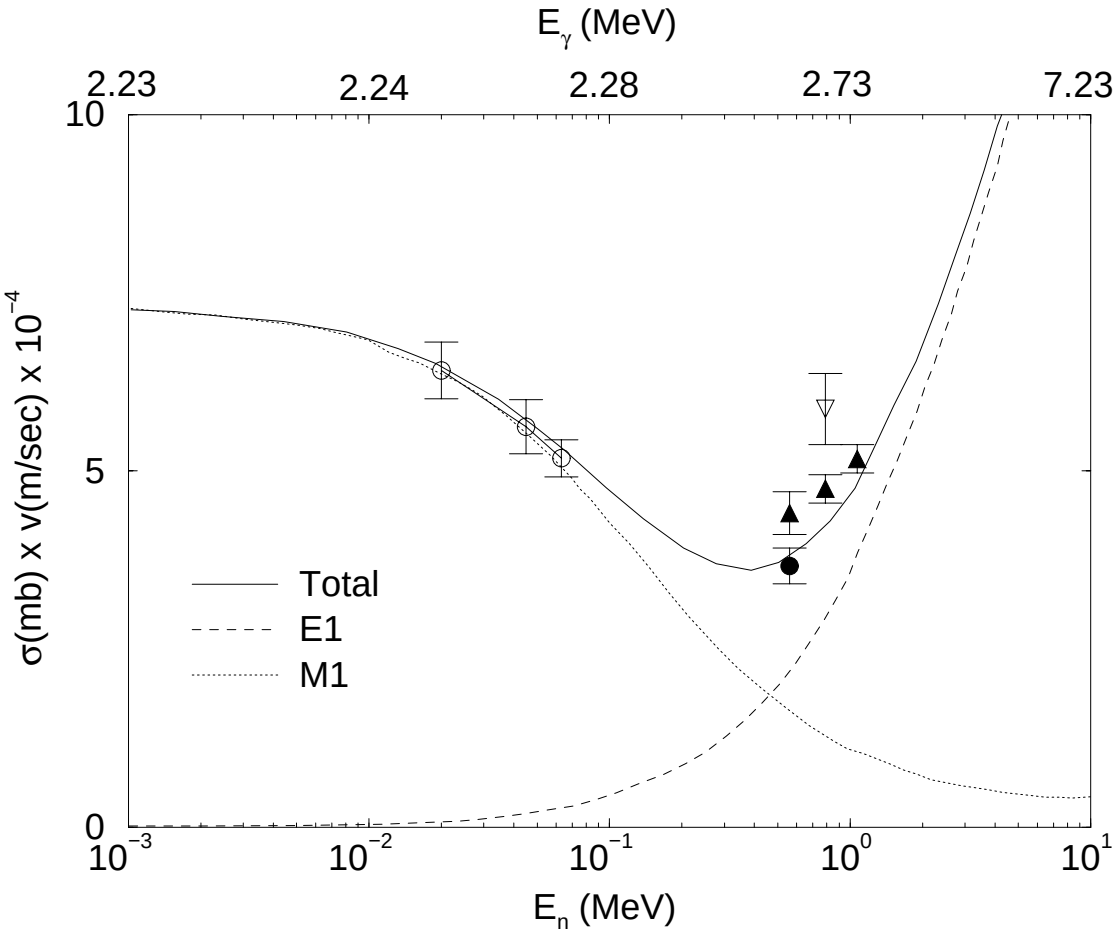

Figure 4.2: Cross-sectional dependence on relative E1 and M1 strengths in n-p capture. The lower energy scale is incident neutron energy in the laboratory frame. The upper energy scale is the photon energy in the corresponding photodisintegration reaction. The experimental data is from [Bis50]. Figure taken from [Nag97]

4.2 Effective Field Theory Calculations

As an alternative to calculating the ^{2}H($\vec{\gamma}$, n)p cross section using various potential models, recent theoretical efforts have made the same calculation using effective field theory techniques [Che99b, Rup99]. In place of the potential models, these calculations rely on the symmetries of Quantum Chromodynamics (QCD), which is currently the most fundamental theory of the strong force.

An effective field theory is a theory that does not explicitly account for all degrees of freedom of the system [Hol95]. Instead, the aggregate effects of all the components of the complete system are parameterized as effective interactions between the principle particles in the reaction. One example of an effective field theory is the treatment of electrons in a superconductor [Hol95]. The full set of degrees of freedom in this system consist of the free electrons and the lattice of ions. The interaction of an electron with the lattice changes the form of the lattice, which in turn has an effect on other electrons. A Lagrangian density exactly representing this interaction would reflect the degrees of freedom of the electrons and all the ions in the lattice. By integrating the lattice out of the Lagrangian, however, one is left with a theory expressed entirely in terms of the effective interaction between electrons in a given pair state. The role of the effective field theory is to account for unknowable or unmanageable degrees of freedom and express their impact as an effective interaction.

In QCD, the nucleon-nucleon (NN) interaction can be constructed out of the interaction of quark-antiquark pairs with color gluons. The individual degrees of freedom of the quarks and gluons can be removed from the Lagrangian density by integrating over interactions in the high-energy regime where quarks and gluons can be treated independently. The resulting effective Lagrangian is written in terms

of nucleon and pion fields. The effects of the QCD elements integrated out of the Lagrangian in short-range NN interactions are contained in the derivative expansion of local operators [Kap98b]. This is in contrast with the direct calculations described in Section 4.1, in which the NN interactions are described by a theoretical framework with many free parameters fit to scattering data.

At low energies (E$\ll$1 GeV), the effects of QCD are expressed in an effective field theory in terms of Chiral Perturbation Theory (ChPT). ChPT can be considered the low-energy EFT of the Standard Model, since it contains all of the symmetries of the underlying theory [Mei94]. ChPT contains the additional assumption that the light quarks (up and down) have masses that are sufficiently small compared to the typical hadronic scale of Λ_H=1 GeV that they can be treated perturbatively [Mei94]. The effective chiral Lagrangian is written as an expansion in energy-momentum, and is considered at up to four orders in momentum, with terms of higher order becoming negligible compared to the chiral scale for energies less than 500 MeV [Hol95]. The most general fourth-order effective chiral Lagrangian for mesons has ten free parameters, the values of which are determined by experiment to renormalize the Lagrangian to correspond to quantitative physical observations [Gas85].

ChPT is defined by the breaking of chiral symmetries in the QCD Lagrangian ($\mathcal{L}_{QCD}$). A symmetry in a Lagrangian is associated with some conserved quantity. If a symmetry of a system is spontaneously broken by some process, and that symmetry is not a symmetry of the vacuum, then a massless particle is generated having the same quantum state that was "broken" in the system [Don92]. Goldstone's theorem [Gol62] states that the spontaneous breaking of a symmetry is characterized by the generation of a massless pseudoscalar ($J^\pi = 0^-$) boson [Hol95]. The complete theory of NN interactions has eight Goldstone bosons: the various pions, kaons, and eta

particles. For NN calculations in which "strangeness" effects (i.e. strange quark) are not included, the role of the Goldstone boson is approximately filled by the pion alone. Because an exact symmetry would require a massless boson, and the pion has been experimentally verified to have mass, the effective chiral Lagrangian can not be written exactly, but rather as an expansion in terms of the order of symmetry breaking [Hol95].

Because the nucleon momentum in the calculation by [Che99b] is well below the pion mass, an effective field theory was developed in which the pion itself does not appear as an explicit degree of freedom [Che99a]. Quark, gluon, and pion effects all appear in the effective Lagrangian as part of a derivative expansion of local nucleon-nucleon operators. A perturbative expansion of the Lagrangian density is constructed using the ratio of the nucleon momentum to the pion mass as a small expansion parameter. A power counting scheme is used to identify the order of momentum of any given Feynman diagram, ensuring that all relevant processes at the appropriate order can be included in the original Lagrangian [Kap98a]. This allows estimates of the overall uncertainty in the calculation to be determined by the order of terms omitted [Kap98b]. This effective field theory technique has been used to calculate the NN scattering phase shifts [Kap98b] and the electromagnetic form factors of the deuteron [Kap99] to next-to-leading order (NLO) in the expansion parameter. In both cases, an NLO expansion of the Lagrangian was sufficient to match experimental data within the predicted theoretical uncertainty of $\sim 10\%$. In the present calculation [Che99b], the Lagrangian is expanded to next-to-next-to-next-to-leading order (N^3LO) in both the E1 and M1 contributions to the $^2H(\vec{\gamma}, n)p$ cross section, leading to an estimated uncertainty of approximately 3%. The results of the calculation are shown in Figure 4.3.

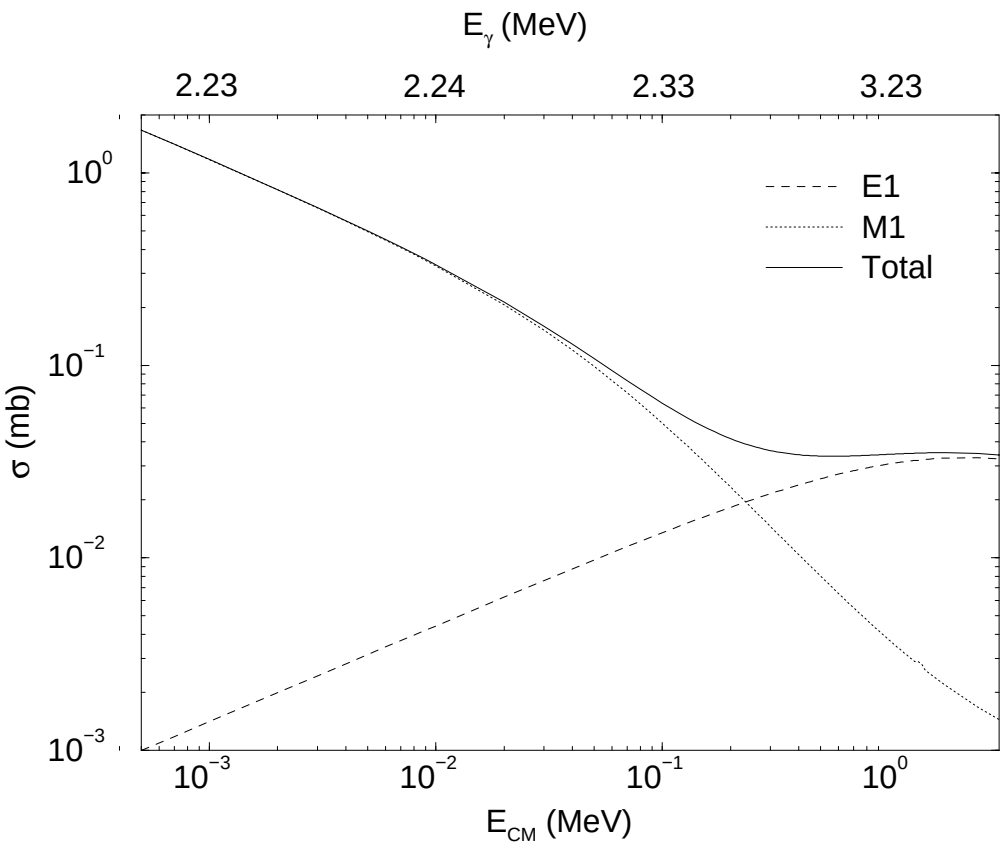

Figure 4.3: Effective-field theory calculations for the n-p capture cross section as a function of the total center-of-mass nucleon kinetic energy [Che99b]. The dashed line indicates the E1 contribution to the cross section. The dotted line indicates the M1 contribution. The solid line represents their sum. The upper energy scale is the photon energy in the corresponding photodisintegration reaction.

4.3 Transition Matrix Element Analysis

While a specific NN potential model or effective field theory is necessary to calculate the amplitudes of the E1 and M1 contributions to the cross section, the angular dependence of the cross section and analyzing power is determined by the amplitude and phases of the participating transition amplitudes. This means that, independent of any specific theory, the cross section and analyzing power for electromagnetic

nuclear reactions can be used to determine the complex Transition Matrix Elements (TMEs) by fitting them to the appropriate expansions in terms of Legendre functions, the coefficients of which are related to the complex TMEs. The formalism for this expansion for reactions of the form $(\vec{\gamma}, X)$ is published in [Wel92]. The TMEs can be written in the form $R_t = |R_t|e^{i\phi}$, where $|R_t|$ is the TME amplitude and ϕ is the phase. Each matrix element in the expansion of a given reaction is identified with an initial state specified by L, S, and J, a particular electromagnetic multipole, and a set of quantum numbers t corresponding to a possible final state of the reaction ,including the channel spin s, the orbital angular momentum ℓ, and the total angular momentum j. For short, we can just use the continuum quantum numbers to label the TMEs because they are unique in the present case. The differential cross section can then be written in terms of these TMEs, according to

$$\sigma(\theta,\phi) = \frac{\lambda\!\!\!^{-2}}{6}\sum_{tt'k'}\left[\left(B_{00}^{k'0} + \frac{1}{\sqrt{10}}B_{20}^{k'0}\right)R_t R_t^{'}P_{k'}(\cos\theta) - \right.$$
$$\left. - f\sqrt{\frac{3}{5}}\cos(2\phi)B_{22}^{k'2}R_t R_t^{'}P_{k'}^{2}(\cos\theta)\right] \quad (4.8)$$

where $B_{kq}^{k'q'}$ are coefficients corresponding to each combination of TMEs, f is the percent linear polarization of the incident γ-ray, and $\lambda\!\!\!^{-}$ is the wavelength of the incident γ-ray divided by 2π. The analyzing power can be defined in terms of Equation 4.8 as

$$\Sigma(\theta) = \frac{1}{f}\frac{\sigma(\theta,0) - \sigma(\theta,\pi/2)}{\sigma(\theta,0) + \sigma(\theta,\pi/2)}. \quad (4.9)$$

4.3.1 Transition Matrix Elements for ^{2}H$(\vec{\gamma}, \mathrm{n})$p

The rules of angular momentum coupling determine what TMEs are present in the ^{2}H$(\vec{\gamma}, \mathrm{n})$p reaction. A ground-state deuteron with $J^\pi = 1^+$ and a γ-ray with arbitrary multipolarity L combine to form a variety of continuum states. These

Initial State S L J	Transition Operator Mode and Multipolarity	Final State s	ℓ	j
$\left\{ \begin{array}{cccc} 1 & 0 & 1 \\ 1 & 2 & 1 \end{array} \right\}$	M1	0	0	0
	M1	1	0	1
	E1	0	1	1
	E1	1	1	0
	E1	1	1	1
	E1	1	1	2

Table 4.1: The quantum numbers for all possible s-wave and p-wave TMEs in the ^{2}H$(\vec{\gamma}, \mathrm{n})$p reaction. The two initial states correspond to the S- and D- state, repsectively, of the deuteron ground state.

states must be allowed in a coupling of a proton and a neutron, both having $J^\pi = \frac{1}{2}^+$. Given the low energy of our reaction, we will only allow $\ell = 0$ and $\ell = 1$ angular momentum coupling between the proton and the neutron. The assignment of γ-ray mode (electric (E) or magnetic (M)) and multipolarity (L) for a given TME is determined by finding which EL and ML multipoles can satisfy both parity and angular momentum conservation for the reaction. The parity of an electric multipole (EL) is given by $(-1)^L$, while the parity for a magnetic multipole (ML) is defined as $(-1)^{L+1}$. The parity of the continuum states are given by $P = \pi_p \pi_n (-1)^\ell$, where π_p and π_n represent the intrinsic parity of the proton and neutron respectively (both having positive parity), and the $(-1)^\ell$ term represents the parity arising from the relative angular momentum of the proton and neutron. Because the parity of the deuteron is known to be positive, we can apply conservation of parity to determine the multipolarity of the γ-ray corresponding to each continuum state. The quantum numbers for each possible continuum state and the corresponding γ-ray mode and multipolarity is shown in Table 4.1.

Including all these TMEs in our expansion would yield six amplitudes and five phases, giving 11 free parameters in all. This difficulty can be overcome by making

some simplifying assumptions. First, we can eliminate one of our E1 terms by noting that electric dipole operator is spin independent. The ground state of the deuteron has a $J^\pi = 1^+$ and has an orbital angular momentum of $\ell = 0$ (with a small admixture of $\ell = 2$). This requires that the ground state of the deuteron have a spin s=1. Because the spin independence of the E1 operator allows only $\Delta s = 0$ transitions, we can eliminate the s=0 E1 TME from the list of possible transitions. We can also eliminate the $j = 1$ M1 term by noting that, because this state has the same quantum numbers as the ground state of the deuteron, an M1 transition between these states would be suppressed due to orthogonality. This leaves us with 4 possible continuum states.

We make the further assumption that the E1 amplitudes are spin independent and can therefore be combined into a single amplitude. Previous calculations and measurements of few-body systems in this energy region support this assumption [Sch97]. In addition, significant differences between the amplitudes and phases of the various E1 TMEs would imply deviations from the angular distribution given by Equation 1.8. These deviations have not been observed in numerous measurements of the ^{2}H(γ,n) angular distribution at energies near those used in the present experiment [Are91]. This leaves us with only two TME amplitudes (hereafter referred to as S and P, for the M1 ($\ell = 0$) and E1 ($\ell = 1$) continuum states, respectively) and one relative phase for our four allowed continuum states. The transitions we will include in our calculations are shown in Table 4.2.

Using the formalism from [Wel92], we can determine the $B_{kq}^{k'q'}$ coefficients for our cross section as defined in Equation 4.8. We note that all the terms corresponding to E1-M1 mixing sum to zero, eliminating the S-P phase from our equations for the cross section and analyzing power. Completing the summation from Equation 4.8,

s	ℓ	j	Multipolarity
0	0	0	S
1	1	0	P
1	1	1	P
1	1	2	P

Table 4.2: The TMEs used in the analysis of the ^{2}H$(\vec{\gamma}, \mathrm{n})$p reaction.

the cross section turns out to be

$$\sigma(\theta, \phi) = \frac{\lambda\!\!\!^{-2}}{6}\left[\frac{1}{4}|S|^2 + \frac{27}{8}|P|^2 \sin^2\theta\,(1 + \cos(2\phi))\right] \tag{4.10}$$

with a corresponding analyzing power given by

$$A(\theta) = \frac{\frac{27}{8}|P|^2 \sin^2\theta}{\frac{1}{4}|S|^2 + \frac{27}{8}|P|^2\,(1 - \cos^2\theta)}. \tag{4.11}$$

Integrating the differential cross section over all angles provides a total cross section given by

$$\sigma_{tot} = \pi\lambda\!\!\!^{-2}\left[\frac{1}{6}|S|^2 + \frac{3}{2}|P|^2\right]. \tag{4.12}$$

We can check the above cross section by noting that the relative contributions of the multipole amplitudes to the total cross section are weighted by [Hay70]

$$\sum_J \frac{2J+1}{(2I+1)(2i+1)}, \tag{4.13}$$

where J is the total angular momentum of the outgoing channel, I is the total angular momentum for the deuteron ($I = 1 \Rightarrow (2I+1) = 3$), and i is the total angular momentum for the incident particle (for photons, $(2i+1) \equiv 2$). Summing over the angular momenta given in Table 4.2, we find that the M1 contribution is weighted by a factor of $\frac{1}{6}$, and the E1 contribution is weighted by a factor of $\frac{9}{6}$. This gives the same expression found in Equation 4.12.

Chapter 5

^{2}H($\vec{\gamma}$, n)p at E_γ=3.58 MeV : Instrumentation and Methods

5.1 Experimental Setup

The relative E1 and M1 amplitudes for the ^{2}H($\vec{\gamma}$, n)p reaction are more easily determined by measuring an analyzing power than by measuring the cross section. This is because a measurement of the analyzing power is a relative rather than absolute measurement, and therefore requires a less exact determination of many experimental parameters. Differences in detector efficiencies, for example, can be ignored if each detector spends the same amount of time in and out of the plane of γ-ray polarization.

The experiment was set up in the southeast optics shack of the DFELL facility. The primary equipment consisted of four neutron detectors placed near a scintillating deuterium target at a lab angle of 150° with respect to the γ-ray beam direction.

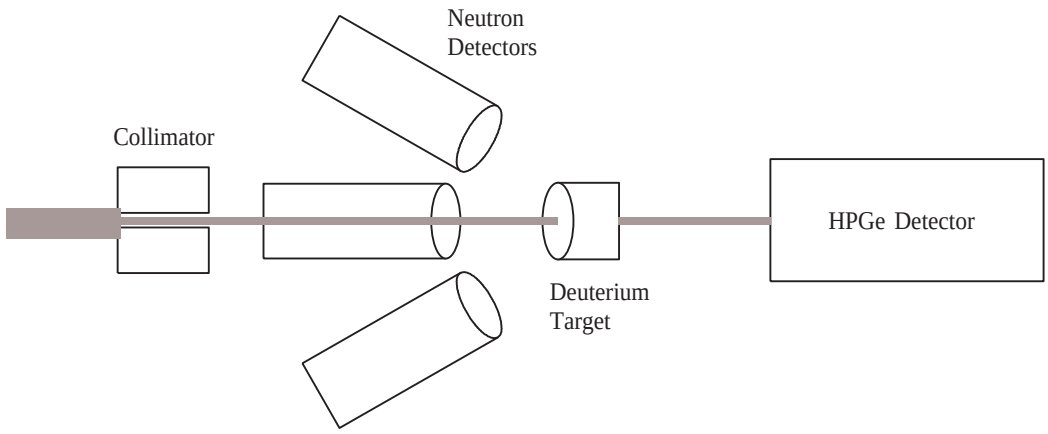

Figure 5.1: Setup for ^{2}H($\vec{\gamma}$, n)p measurement. The detectors were positioned at 150° with respect to the γ-ray beam axis.

Although the same analyzing power was expected for detectors placed at 30°, as shown in Figure 4.1, the back-angle configuration was chosen to minimize the likelihood of γ-rays which are Compton scattered from the deuterium target from hitting the neutron detectors. The neutron detectors were placed in the up, down, left, and right positions, and were attached to a rotating detector mount so that detectors could be rotated in and out of the plane of γ-ray polarization without unmounting them and possibly changing their relative positions. A HPGe detector was placed downstream of the deuterium target to monitor the γ-ray beam. As an additional beam monitor during test runs, a thin plastic scintillator was placed immediately downstream of the collimator. A general schematic of the experimental apparatus is shown in Figure 5.1.

5.2 Beam Characteristics

The ^{2}H($\vec{\gamma}$, n)p analyzing power measurement is most useful as close to threshold as possible, so the γ-ray energy was chosen to have the lowest practical value above 2.2 MeV. For all energies used, the FEL was configured to produce photons near 379 nm (3.27 eV), since this wavelength corresponded to the maximum reflectivity of the cavity mirrors, and therefore the maximum intracavity flux. Initial attempts to measure the recoiling neutrons produced by 2.86 MeV γ-rays (from 240 MeV electrons) and 3.1 MeV γ-rays (from 250 MeV electrons) were unsuccessful due to the inability of the four neutron detectors to detect neutrons of so low an energy. The first successful measurements were made using 3.58 MeV γ-rays produced by scattering 382.5 nm (3.24 eV) photons from 270 MeV electrons.

Because the electron energy used in this measurement is below the maximum operating energy for the linear accelerator, electrons could be continually injected into the storage ring without the need to ramp the electrons to the appropriate energy. This allowed electrons ejected from the beam during normal operation to be replaced while the experiment was being run, allowing storage ring currents above 10 mA to be maintained throughout the experiment. Because these beam parameters are near the bottom of the operating range of the DFELL facility, the γ-ray flux was limited to approximately $10^4\gamma$'s/sec.

The initially limited available γ-ray flux necessitated the use of a large aperture collimator to provide as much beam on target as possible. A lead collimator with a 1.5 cm diameter aperture was therefore chosen. This provided a γ-ray distribution with a FWHM of 80 keV, giving a measured energy resolution of $\Delta E/E = 2.5\%$. A sample spectrum measured by a downstream HPGe detector is shown in Figure

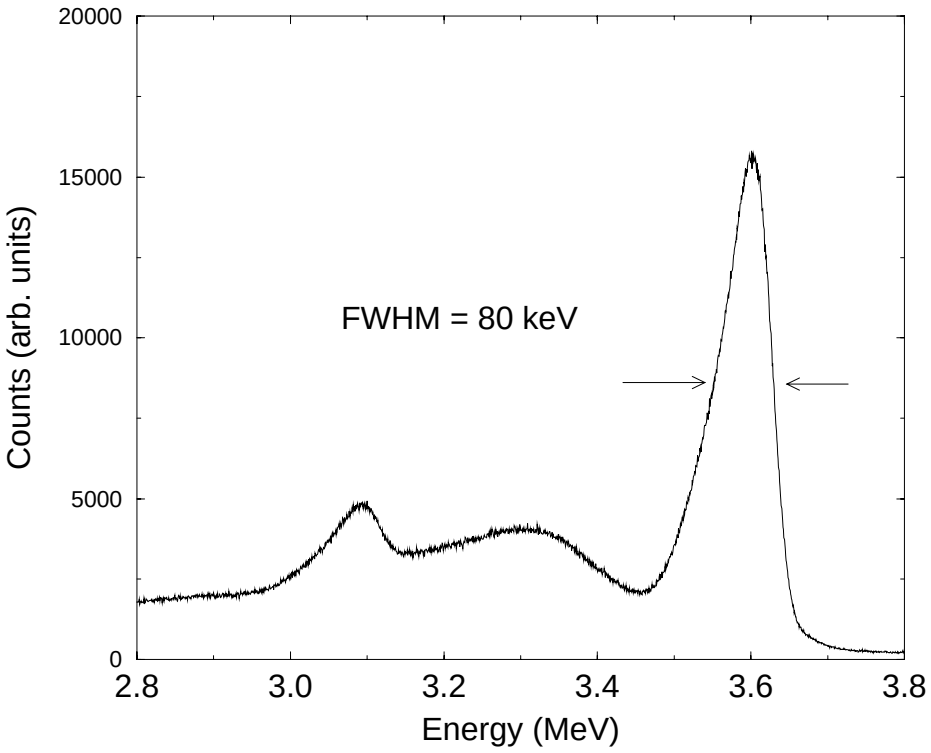

Figure 5.2: Gamma-ray distribution used for ^{2}H($\vec{\gamma}$, n)p measurement. The full energy peak, which represents the actual γ-ray energy distribution, has a FWHM of 80 keV.

5.2. The detector system used for this measurement is identical to that described in Section 3.2.4.

5.3 Deuterium Target and Detectors

In any time-of-flight measurement, background can be considerably reduced by using an active target. A deuterated NE232 scintillator was therefore chosen as our deuterium target. The C_6D_{12} fluid has a density of 0.89 g/cm^3, and was contained

Detector	Composition	Diameter (cm)	Length (cm)	Positions
1	NE-213	5.08	5.08	RU
2	NE-213 (deuterated)	4.0	4.0	UL
3	BC-501A	5.08	5.08	DR
4	BC-501A	5.08	7.62	LD

Table 5.1: Properties of detectors used in the ^{2}H($\vec{\gamma}$,n)p measurement. Position refers to the two positions the detector was rotated between, with U referring to up, D down, L beam left and R beam right.

in a 3.7 cm diameter $\times$ 4.18 cm long cylinder. The target has a deuterium-to-carbon ratio of 1.96, giving it a deuterium number density of 6.68×10^{22} D/cm^3, slightly higher than that of heavy water. The scintillator was attached to a piece of light pipe and mounted on a RCA 8675 photomultiplier tube so that the scintillation signals from recoiling protons and electrons could be detected.

The neutron detector set consisted of two NE-213 detectors (one of which was deuterated) and two BC-501A detectors. Each neutron detector was mounted on a Hamamatsu H-1161 photomultiplier tube and base. The deuterated NE-213 detector was found to have insufficient PSD qualities to be useful for our measurement, and will therefore no longer be considered. The remaining NE-213 detector and the two BC-501A detectors have virtually identical properties, each having a density of 0.874 g/cm^3 and a hydrogen-to-carbon ratio of approximately 1.212. The dimensions and positions of each detector is given in Table 5.1.

The low γ-ray flux required that the detectors be placed as close as possible to the deuterium target to maximize the solid angle and hence the count rate. The detectors were therefore situated such that the center axis from each detector intersected with the γ-ray beam axis at the same position, with the face of each detector being 5.08 cm from this intersection point. The deuterium target was situated with its center

axis in the plane of the γ-ray polarization, the horizontal plane, and making an angle of 27.5° with the γ-ray beam axis. The target was then centered at the central point at which all the neutron detectors were aimed.

The detectors were placed on a movable mount that allowed them to be rotated in and out of the plane of γ-ray polarization without having to unmount them and possibly change their relative positions. Because the detectors are liquid scintillators, there existed the possibility that a given detector might have a slightly different efficiency when in the horizontal and vertical positions, respectively. This possible difference in efficiency was tested by fixing a ^{22}Na γ-ray source to the surface of each detector and rotating the detector between its two assigned positions. ^{22}Na has a half life of approximately 2.6 years, so could be considered to produce 511 keV γ-rays at a constant rate over the period of the measurement. For all detectors, variations in efficiency between the horizontal and vertical positions were found to be less than 1%.

5.4 Electronics

A measurement of the analyzing power of ^{2}H$(\vec{\gamma}, \mathrm{n})$p requires a careful separation of neutron and γ-ray events in the detectors. Detector signals from γ-rays and neutrons differ both in the shape of the signal and in the flight time from the target to the detector. The anode signal from each detector is therefore copied by a LeCroy 428F Linear Fan and sent through two circuits: one for pulse-shape discrimination (PSD) and one for time-of-flight (TOF). The complete electronics setup for one detector is shown in Figure 5.3.

Gamma-ray and neutron events create differently shaped signals in detectors.

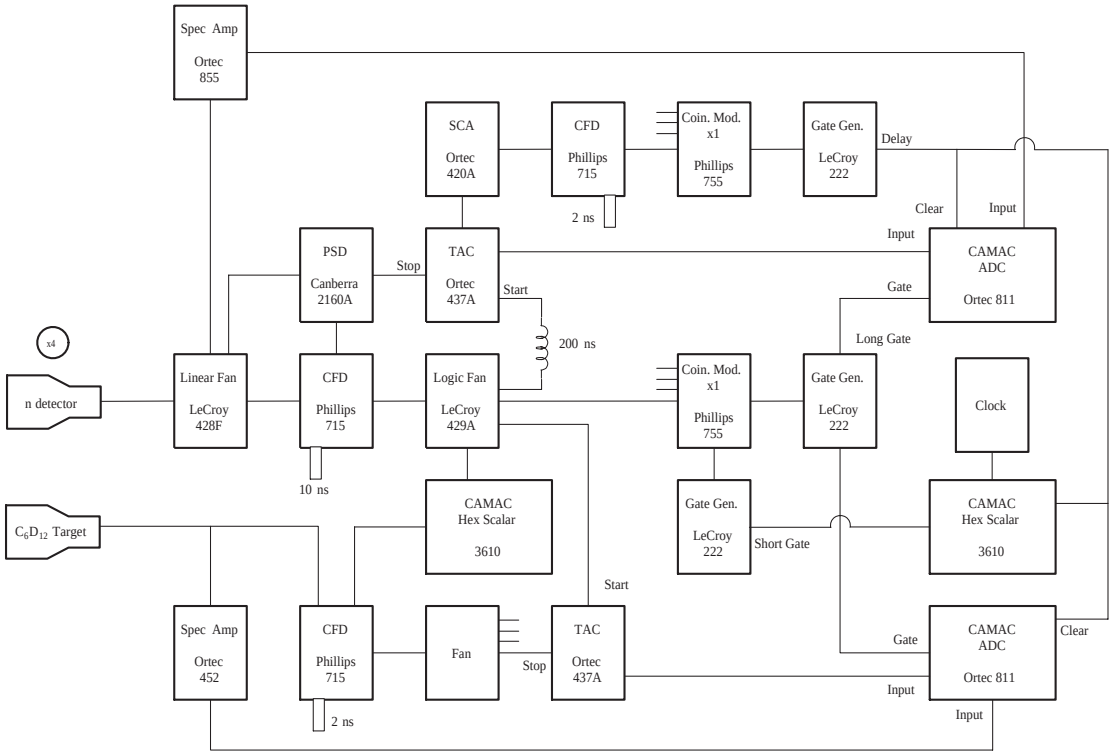

Figure 5.3: Electronics setup for $^2\mathrm{H}(\vec{\gamma},\mathrm{n})\mathrm{p}$ measurement. The above diagram represents the electronics for one of four neutron detectors. All coincidence modules act as an OR between identical signals from each of the four neutron detectors.

Photons interact with detector materials electromagnetically, whereas neutrons only interact through the strong force. Neutrons therefore deposit their energy more gradually, as shown in Figure 5.4, leading to a longer pulse duration. This pulse duration is measured by sending one copy of the anode signal into a Phillips 715 Constant Fraction Discriminator (CFD) and another into a Canberra 2160A PSD module. The logic output from the CFD is delayed and sent as a start signal to an Ortec 437A Time-to-Amplitude Converter (TAC). The PSD module integrates the anode signal, producing a pulse shape whose rise time depends on the decay time of the initial signal. The integrated signal is then doubly differentiated, producing a bipolar pulse whose zero crossing is determined by the rise time of the integrated signal [Leo94, Can83]. This process is illustrated in Figure 5.5. The resulting bipolar signal has a zero crossing that occurs later for longer neutron pulses than for shorter γ-ray signals. A logic signal is generated at this zero crossing, which becomes the stop signal for the TAC, producing a spectrum with a narrow γ-ray peak and a broader neutron peak. This spectrum is read into the computer by an Ortec 811 Analog-to-Digital Converter (ADC).Because of limitations in both detector and electronics response, very high energy γ-rays can produce a saturated signal that appears as a neutron signal in the PSD spectrum. To separate these high energy γ-rays events from neutron events, the PSD signal was combined with a pulse-height signal to make a two-dimensional PSD spectrum. This pulse height spectrum was generated by putting the detector anode signal through an Ortec 855 Spectroscopy Amplifier and reading the resulting signal into the computer through the same ADC as the PSD signal.

Because the (γ, γ) cross section is several orders of magnitude higher than the (γ, n) cross sections, the vast majority of events in the neutron detectors will be photons. To keep these signals from occupying the computer unnecessarily, a veto

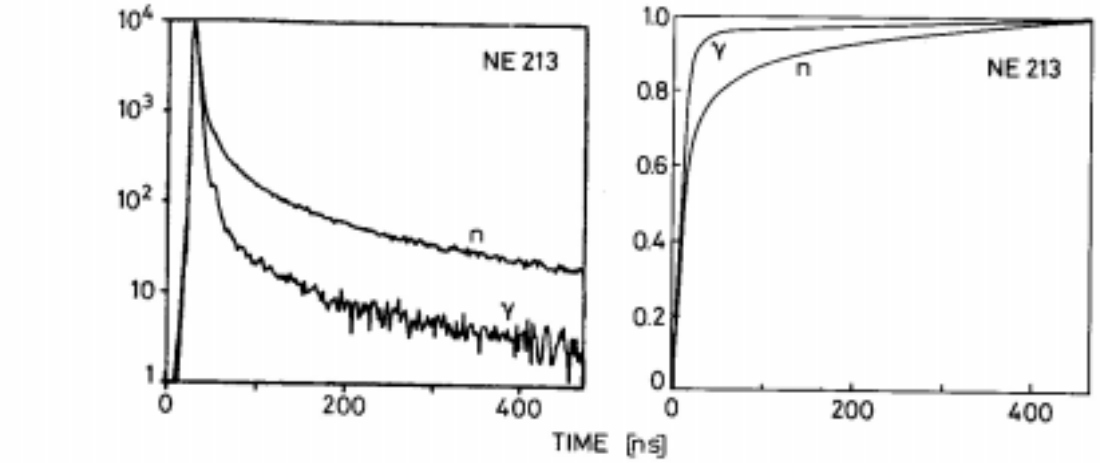

Figure 5.4: The behavior of neutron and γ-ray interactions in an NE213 detector. The left figure shows scintillator light output vs. time. The right figure shows the time integral of the light pulses. Figure taken from [Leo94].

circuit was set up for each detector. A copy of the PSD TAC signal was sent to an Ortec 420A Single Channel Analyzer (SCA). The acceptance window of the SCA was set around the γ-ray portion of the PSD spectrum. The output of the SCA was sent through a CFD and a LeCroy 222 Gate and Delay module, which delayed the signal to make it coincide with the the gate for the ADC. The SCA signal could then be used to clear the ADC, reducing the number of γ-ray events read into the ADC and therefore greatly reducing computer dead time. The resulting one and two-dimensional PSD spectra are shown in Figure 5.6 and Figure 5.7, respectively.

The time-of-flight for each event in a given detector was also recorded to achieve further separation of photon and neutron events, as well as determine the energy of the detected neutrons. The time-of-flight for each detector was determined using an Ortec 437A time-to-amplitude converter (TAC). The linear signal from each detector

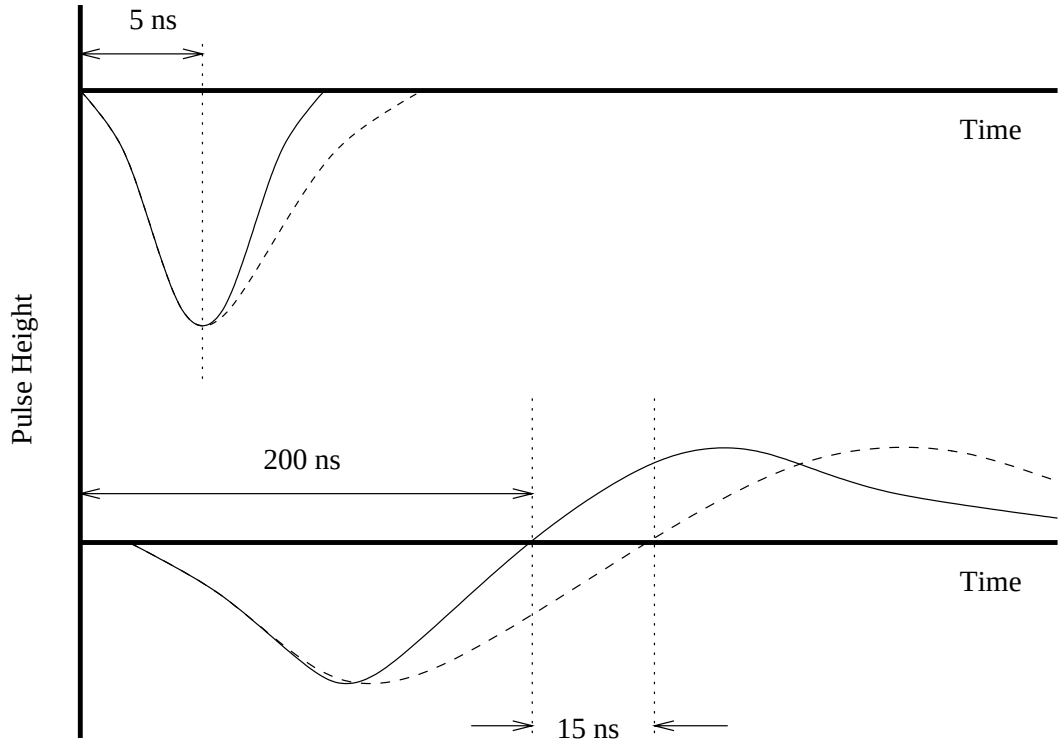

Figure 5.5: Schematic representation of the pulse shaping in a Canberra 2160A PSD module. The top graph represents the anode signal from the detector, and the bottom graph represents the shaped signal with a zero crossing proportional to the decay time of the anode signal. The time scales are approximate and correspond to typical photon (solid line) and neutron (dashed line) signals in an NE213 detector [Can83].

was sent through a CFD, which produces a logic pulse that starts the detector's TAC. The linear signal from the deuterium target was sent into a CFD and fanned to provide a stop signal for the four TACs. Because the signals from recoiling protons are so small, the threshold of the target CFD was set as low as possible to ensure that no signals were lost. A copy of the CFD output was also sent to a scalar module, allowing the total number of γ-ray-target interactions (either (γ, n) or (γ, γ)) to be used as a normalization between runs.

A copy of the linear signal from the deuterium target was amplified using an

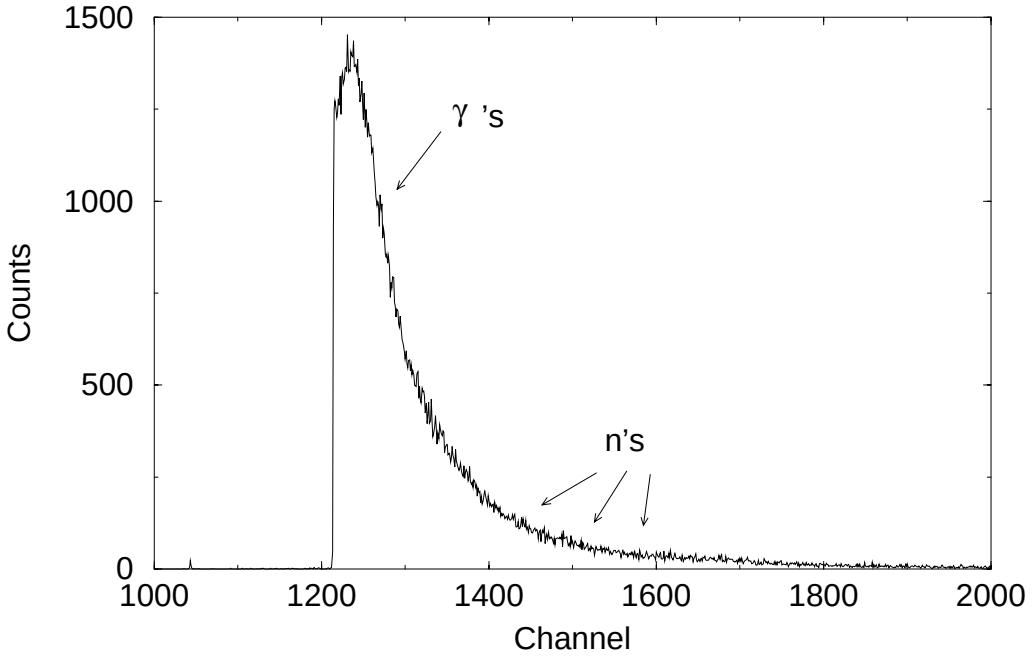

Figure 5.6: PSD spectrum from a single detector. The cutoff at channel 1210 is determined in hardware by an SCA, and is designed to keep excess γ-ray events from being read into the ADC. The neutrons in this spectrum are not visible over the photon background. The location of the neutrons can be determined from the two-dimensional spectrum shown in Figure 5.7.

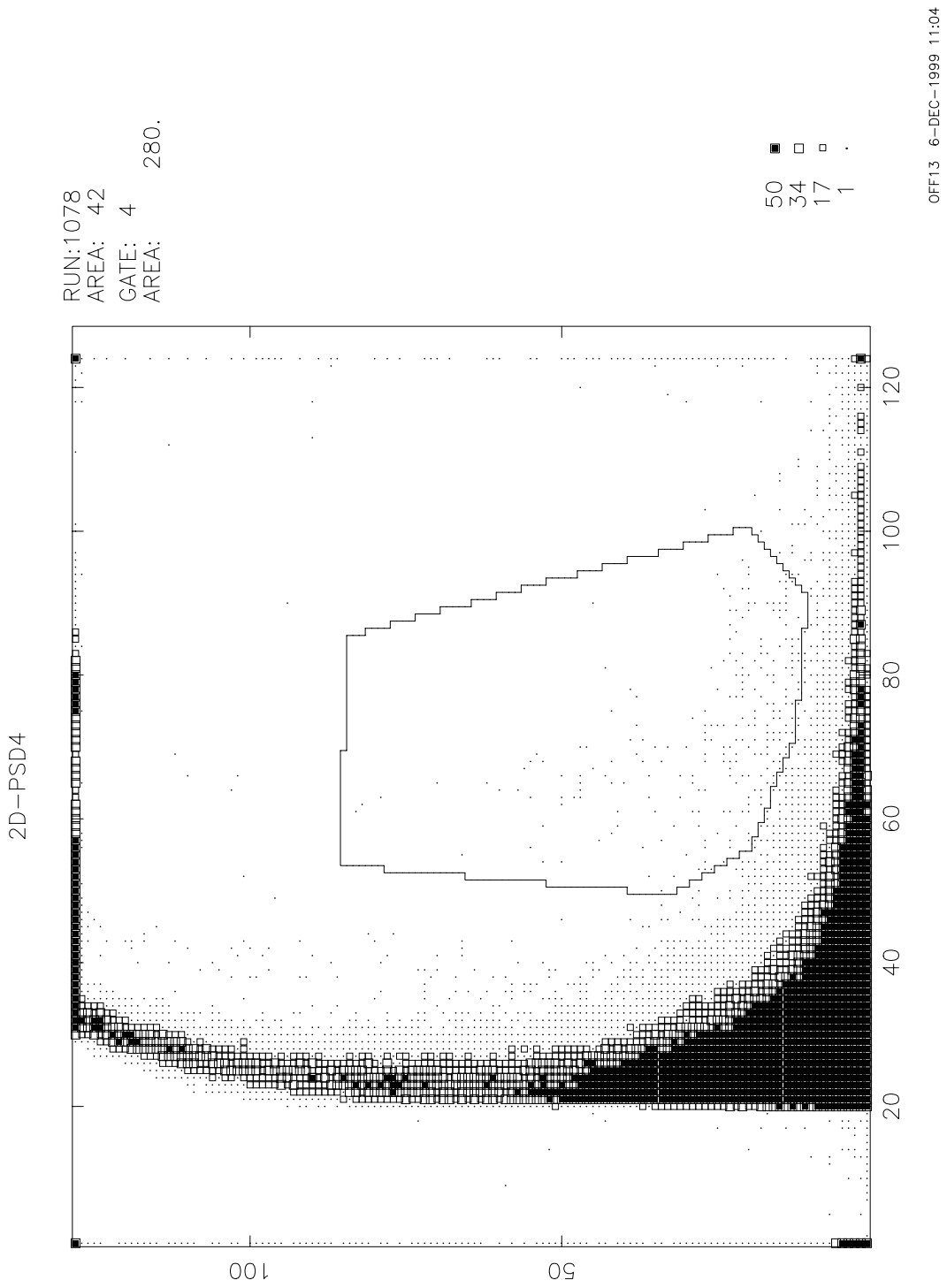

Figure 5.7: XSYS display of two-dimensional PSD vs. pulse height spectrum. The gate surrounds the region containing neutrons. Figure 5.6 is the projection of this spectrum on the x-axis.

Ortec 452 Spectroscopy Amplifier and read into the computer by the ADC. A sample spectrum from this target is shown in Figure 5.8. This energy spectrum can be used to make an additional software cut to help separate photodisintegration events from background. Because a scattered electron from a Compton scattering event deposits more energy than a recoiling proton from a photodisintegration event, a software gate set around the probable region of photodisintegration events allows a better separation of γ-ray and neutron events in the four neutron detectors. The energy range covered by this gate was optimized during offline analysis to maximize the neutron to γ-ray ratio in each detector spectrum.

The HPGe detector used in this measurement was set up using the standard electronics shown in Figure 3.1, with the exception that the second gate and delay generator was removed, being made unnecessary by the long signal duration of HPGe. For the thin plastic scintillator, the anode signal was put through a CFD to produce a logic signal. Because very few γ-rays would leave all of their energy in the detector, the threshold on the CFD was set barely above the voltage corresponding to room background to maximize the count rate in the detector. The resulting logic signal was sent to a scalar module to record the total number of interactions for a given measurement.

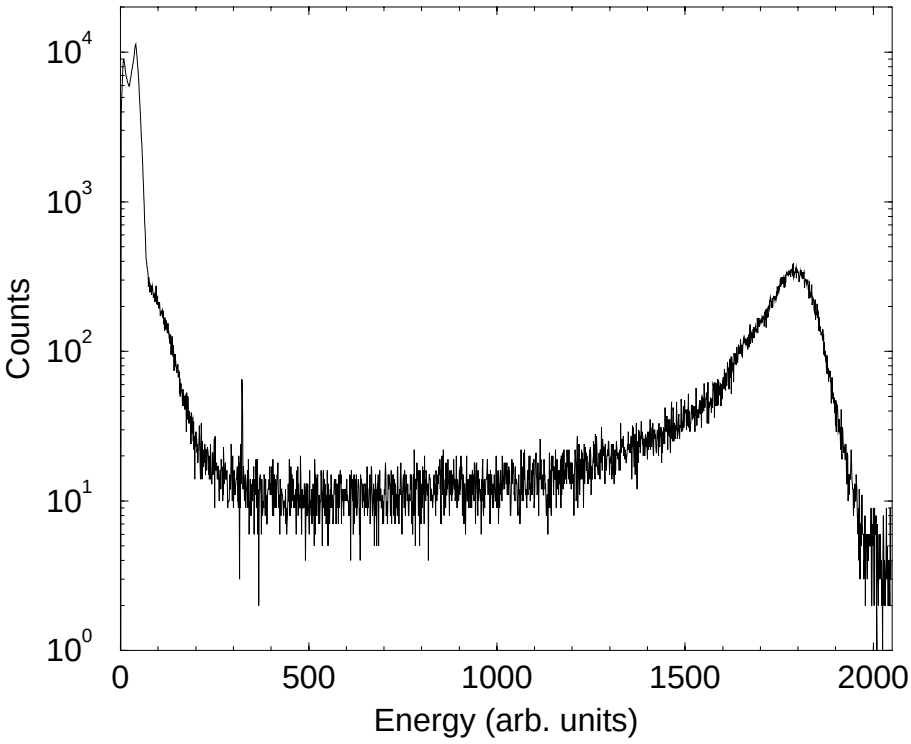

Figure 5.8: Energy signal from C_6D_{12} target. The full scale of the spectrum is set such that the detector response to 662 keV γ-rays from a ^{137}Cs source would occupy the entire spectrum. The right peak contains Compton scattered events.

Chapter 6

$^2\mathrm{H}(\vec{\gamma},\mathrm{n})\mathrm{p}$ at $\mathbf{E_\gamma}$=3.58 MeV: Analysis and Results

The experimental apparatus described in Chapter 5 was successful in measuring a statistically significant number of photoneutrons in approximately eighteen hours of γ-ray beam time. This chapter documents the analysis of the observed neutron asymmetry and the extraction of the relative E1 and M1 strengths in the $^2\mathrm{H}(\vec{\gamma},\mathrm{n})\mathrm{p}$ reaction.

6.1 Experimental Results and Offline Analysis

As was mentioned in Section 5.3, the deuterated neutron detector (specified as Detector 2) had insufficient PSD qualities to discriminate between neutron and γ-ray events, and therefore did not produce usable results. Similarly, offline analysis after the experiment was completed revealed the presence of irregularities in the spectra

for Detector 3 that contaminated the measurement. The irregularities were most likely the result of faulty electronics modules used in processing Detector 3's signals, and contributed to an overall decrease in the measured analyzing power. In portions of the spectra where the irregularities could be isolated, the analyzing power was found to be near zero. However, because the irregularities could not be reliably and completely extracted from the "good" counts detected by Detector 3, the results from this detector were also excluded from the analysis. The data from the remaining detectors (designated Detector 1 and Detector 4) were included in the analysis.

Using the two-dimensional PSD cut shown in Figure 5.7, the remaining detectors produced spectra with an easily identifiable neutron analyzing power. Accumulated spectra for a single detector both in and out of the plane of γ-ray polarization are shown in Figure 6.1 and Figure 6.2. In these "raw" spectra obtained during the experiment, the γ-ray and neutron portions of the TOF spectra are easily identifiable. However, because of the compact geometry of the detector apparatus, the separation of the neutron and γ-ray peaks was not sufficient to reliably extract the neutron counts from these spectra.

Offline analysis of the data included several additional cuts designed to both reliably extract the neutron data from the γ-ray data and to produce a result that could be accurately simulated during later analysis. The first additional cut involved setting a gate around the energy spectrum from the C_6D_{12} target. The majority of the γ-ray events are contained in the right-most peak shown in Figure 5.8, so the gate would be set to avoid that region. However, because no clear neutron peak exists, the ideal gate position was determined empirically by repeating offline analysis with a variety of gates until the neutron analyzing power was maximized. This maximization scheme is valid because γ-ray contamination in the neutron spectrum would exhibit

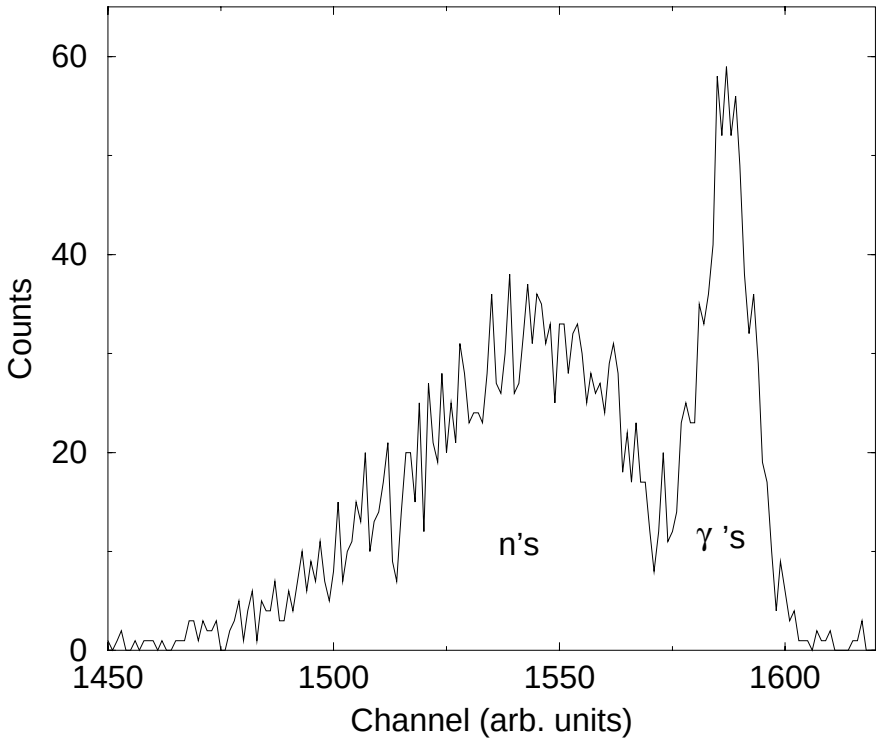

Figure 6.1: Accumulated neutron data from a single detector in the plane of the γ-ray polarization. This spectrum is generated from the PSD cut shown in Figure 5.7. Time increases from right to left, so the photon peak is the narrow peak on the right, and the neutrons are the broad peak on the left.

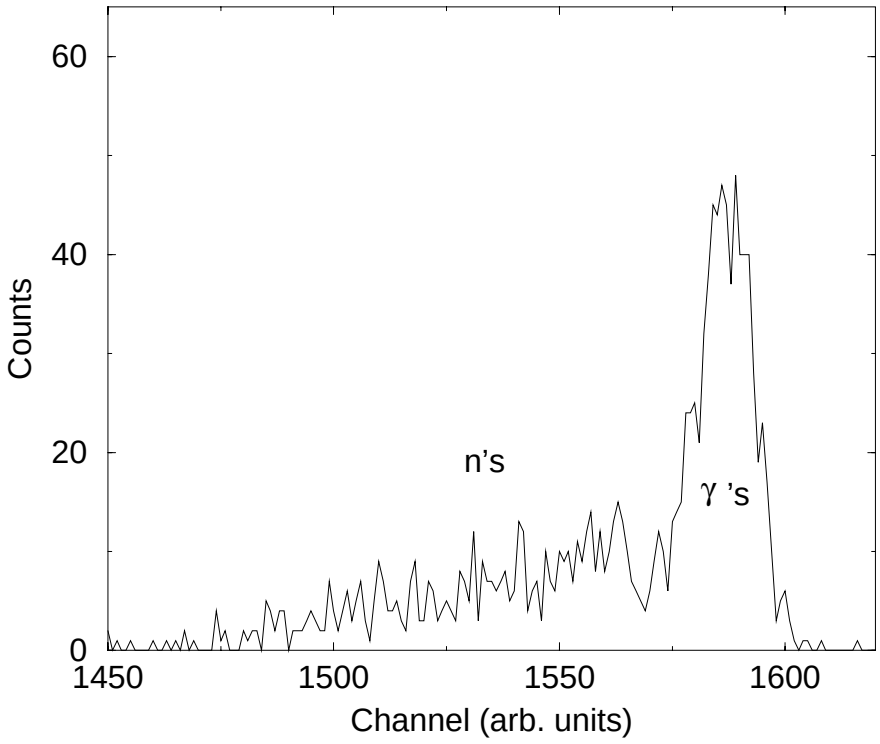

Figure 6.2: Accumulated neutron data from a single detector perpendicular to the plane of γ-ray polarization. This spectrum is generated from the PSD cut shown in Figure 5.7. Time increases from right to left, so the photon peak is the narrow peak on the right, and the neutrons are in the broad peak on the left.

a small negative analyzing power. The γ-ray analyzing power is defined by the Klein-Nishina equation, which can be written as

$$\frac{d\sigma}{d\Omega} = \frac{r_e^2}{2}\left(\frac{E'}{E}\right)^2\left[\frac{E}{E'} + \frac{E'}{E} - 2\sin^2\theta\cos^2\phi\right], \tag{6.1}$$

where E and E' are the incident and scattered γ-ray energies, r_e is the classical electron radius, θ is the scattering angle with respect to the γ-ray beam axis, and ϕ is the azimuthal scattering angle with respect to the plane of γ-ray polarization. For 3.58 MeV γ-rays scattering at a lab angle of 150°, the photon analyzing power is found to be -0.018, where the analyzing power is defined in terms of the cross section according to Equation 4.9. Because Compton scattered polarized γ-rays exhibit a small negative analyzing power, the maximization of the neutron analyzing power is indicative of a minimization of photon contamination in the spectrum.

A second adaptation made during the offline analysis involved resetting the two-dimensional gate used in the PSD cut. While the gate shown in Figure 5.7 may be considered to reliably contain the majority of the neutron counts, the cut represents a lower pulse height threshold that changes with position in the PSD spectrum. This means that neutron events that are binned into a "larger" PSD value would have a lower energy threshold as a condition for being counted than those binned into a "smaller" PSD value. Because the pulse height of a neutron signal is not perfectly correlated with the pulse width and corresponding PSD value, this varying threshold could not be accurately accounted for in later analysis. The two-dimensional gates were therefore reset with a corresponding constant lower threshold. A typical gate is shown in Figure 6.3. The pulse height spectra for each detector had been calibrated using a ^{137}Cs source, so the neutron energy corresponding to the lower cutoff could be determined. The value for the cutoff varied according to the properties of the individual detectors, but was generally set near 400 keV.

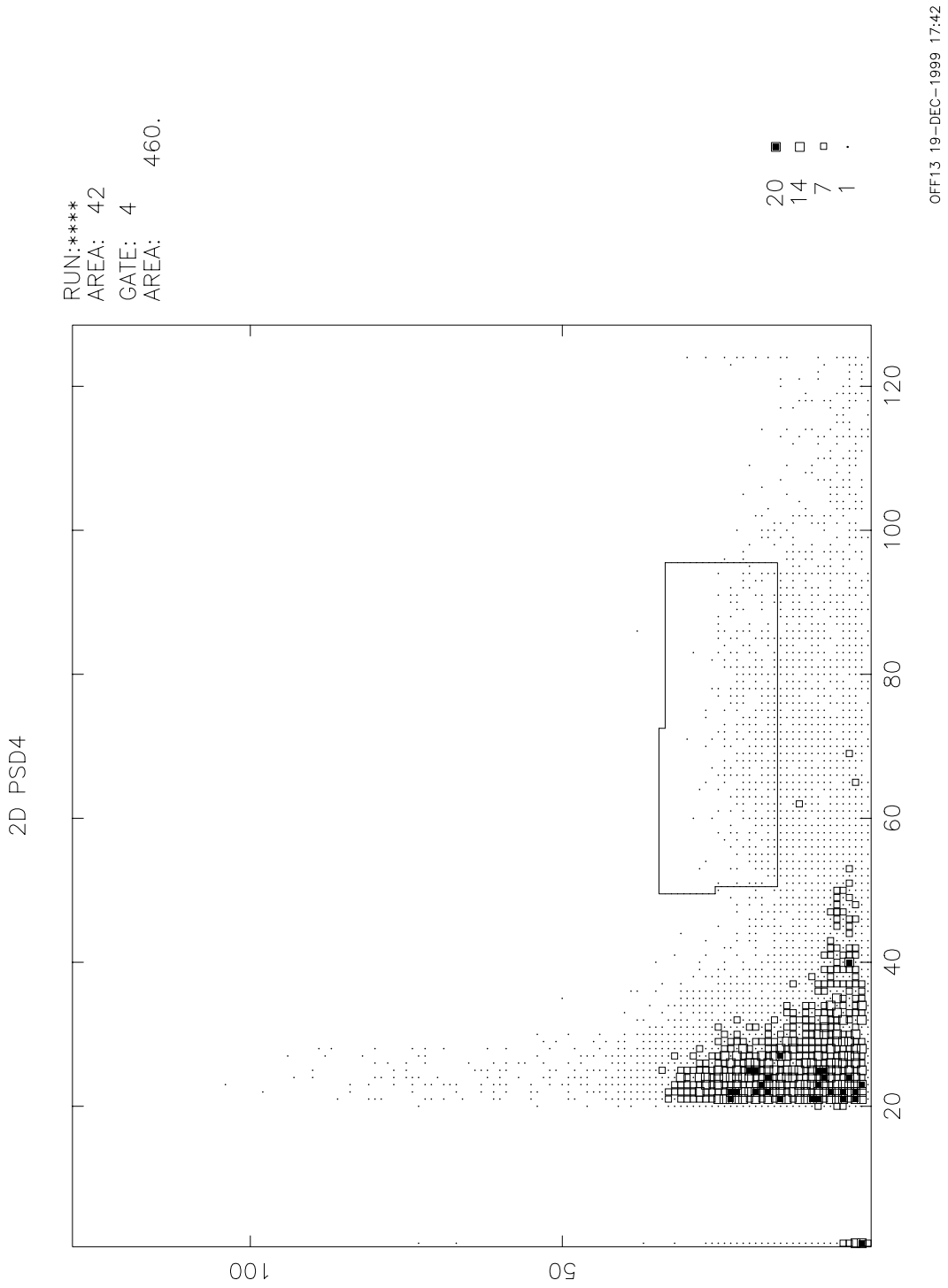

Figure 6.3: XSYS display of two-dimensional PSD vs. pulse height spectrum after a software cut has been made in the neutron region of the target energy spectrum. The displayed gate has been set to have a constant lower threshold of 360 keV.

Detector	Parallel	Perpendicular	Asymmetry
1	453	106	0.621 ± .03
4	460	102	0.637 ± .03

Table 6.1: Total counts and asymmetry measured by each neutron detector. The counts have been normalized to account for unequal beam time spent in each detector position. The error is statistical only.

A final offline cut was made on the raw TOF spectrum. Simple kinematic calculations indicate that a neutron produced in the target will require at least 3 ns to reach any of the neutron detectors. A gate was therefore set on the raw TOF spectra excluding any detector events occurring within 3 ns of the center of the γ-ray peak. The spectra resulting from these offline cuts are shown in Figure 6.4 and Figure 6.5.

The data accumulated from each detector could not be combined to determine an overall asymmetry without a precise knowledge of possible differences in detector efficiency. The close proximity of the detectors to the target and the extremely low thresholds set on the detectors made the precise efficiency of each detector difficult to determine. Accordingly, each detector was treated as a separate measurement of the neutron asymmetry. The total number of counts in each detector had to be normalized to account for the different amount of beam time spent in each position. This normalization was determined by comparing the total number of γ-rays measured by the HPGe detector in each of the two detector positions. This comparison indicated that an 8.0% increase was required for one detector configuration to normalize the two detector positions to the same total incident γ-ray flux. The results of this renormalization and the resulting analyzing powers are given in Table 6.1. The errors assigned to each asymmetry are statistical, and are calculated according to [Leo94]

$$\sigma_A = 2\sqrt{\frac{N_{||}N_{\perp}}{N_{tot}^3}}, \tag{6.2}$$

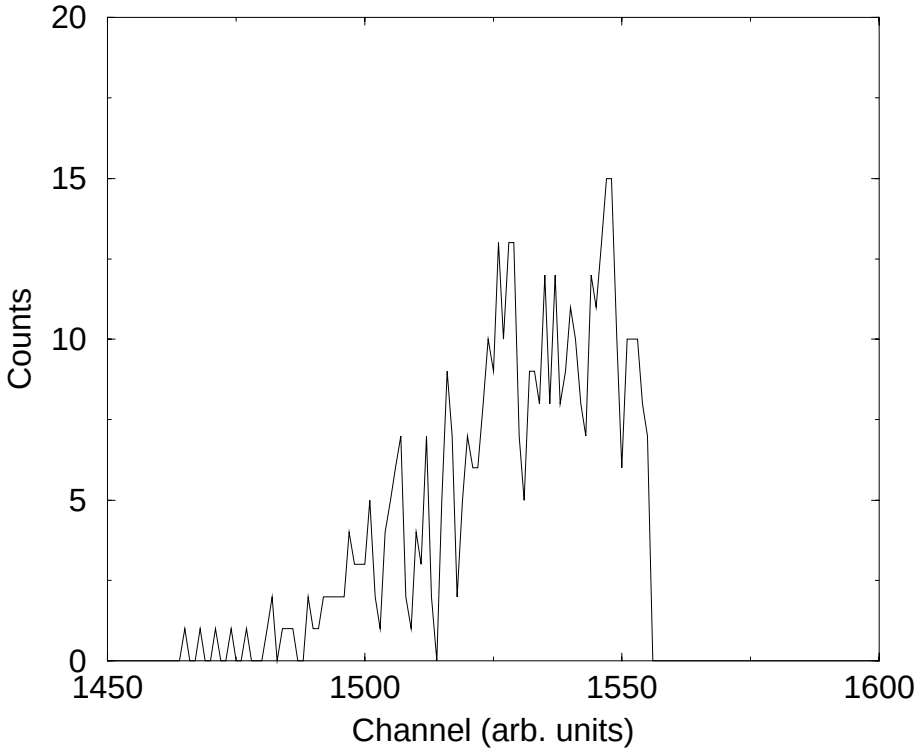

Figure 6.4: Accumulated neutron data from a single detector in the plane of the γ-ray polarization. This spectra is generated from the PSD shown in Figure 6.3 and the TOF cuts.

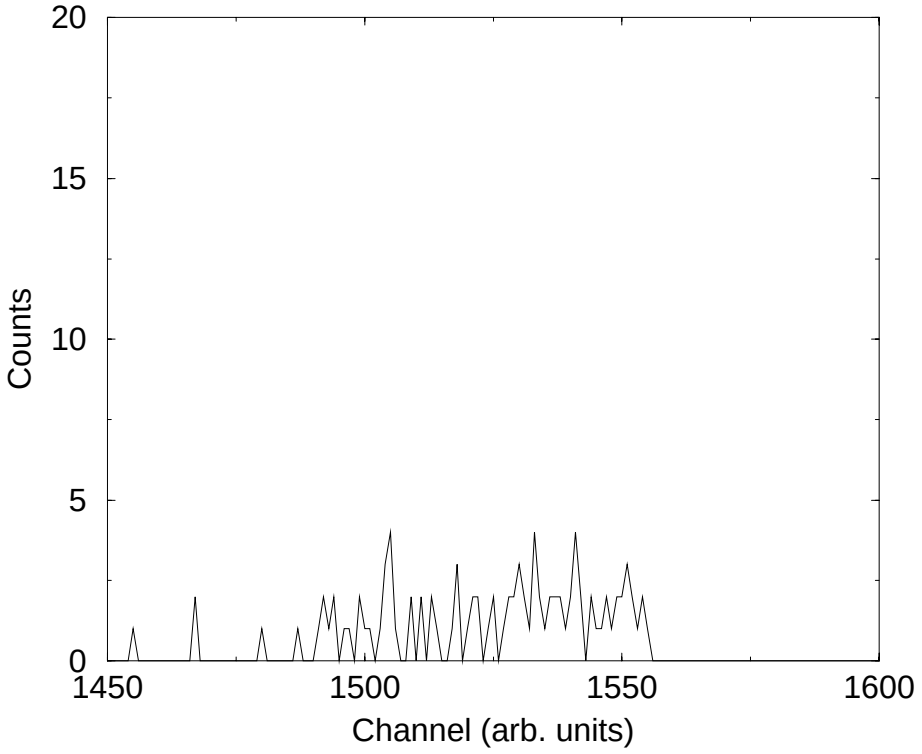

Figure 6.5: Accumulated neutron data from a single detector perpendicular to the plane of the γ-ray polarization. This spectra is generated from the PSD cut shown in Figure 6.3 and the TOF cuts.

where $N_{||}$ is the number of counts measured by the detector in the plane of γ-ray polarization, $N_{\perp}$ is the number of counts measured in the perpendicular position, and $N_{tot} = N_{||} + N_{\perp}$.

6.2 Monte Carlo Simulation

The asymmetry measured by the detector apparatus is not a direct measurement of the ^{2}H$(\vec{\gamma}, \mathrm{n})$p analyzing power at 150°. The finite size of the deuterated target and the detectors allows neutrons ejected from the target at angles differing from 150° to interact with one of the neutron detectors. Because the detectors and target were placed extremely close together during this experiment, the angular acceptance around 150° is considerable. In addition, a neutron produced by a photodisintegration event can elastically or inelastically scatter off of other nuclei in the apparatus, changing its trajectory and energy. This process of multiple scattering can cause a neutron that was emitted at 150° to be scattered away from a detector with which it otherwise would have interacted. Similarly, neutrons with initial trajectories in any direction can be scattered into one of the detectors and be counted as "good" events.

In order to extract the "true" asymmetry for ^{2}H$(\vec{\gamma}, \mathrm{n})$p at 150°, the contribution of these finite geometry and multiple scattering effects need to be known. A Monte Carlo simulation, NCOR, was written to make these corrections for this experiment.

6.2.1 Simulation Overview

The program NCOR attempts to simulate all relevant physical processes involved in the detection of neutrons resulting from the ^{2}H$(\vec{\gamma}, \mathrm{n})$p reaction. Rather than taking the measured asymmetry and trying to extract an initial angular distribution that

would lead to such a measurement, NCOR assumes an initial angular distribution for ^{2}H($\vec{\gamma}$, n)p and determines what the measured asymmetry would be for such a distribution. The user can then vary the initial ^{2}H($\vec{\gamma}$, n)p angular distribution until NCOR reproduces the measured asymmetry. The solution can be considered unique because the initial angular distribution can be completely determined by varying a single parameter. From the analysis in Section 4.3.1, it was determined that the ^{2}H($\vec{\gamma}$, n)p differential cross section could be expressed in terms of two parameters, the s-wave and p-wave strengths, as shown in Equation 4.10. Because the asymmetry measurement is a relative measurement, only the angular dependence of the ^{2}H($\vec{\gamma}$, n)p cross section is required. This shape can then be determined by a single parameter R by assuming the cross section can be written as

$$\sigma(\theta, \phi) = R + \sin^2\theta\,(1 + \cos 2\phi)\,, \tag{6.3}$$

which can be related to Equation 4.10 by defining the constant R as

$$\frac{2}{27}\,|S|^2 = R\,|P|^2\,. \tag{6.4}$$

Once the shape of the initial distribution is determined, the initial position of the neutron within the target is assigned by picking a random location in the intersection of the γ-ray beam and the cylindrical deuterium target. The initial neutron trajectory is chosen according to the distribution determined by Equation 6.3. The neutron energy is determined by randomly selecting a γ-ray energy from a Gaussian fit to the measured spectrum shown in Figure 5.2. The neutron energy is then adjusted to account for the kinematics associated with the recoiling proton and the incident γ-ray momentum.

NCOR then determines the path length out of the target along the initial trajectory, and calculates the probability of elastically scattering from carbon or deuterium

nuclei in the target. The interaction cross sections are obtained from ENDF tables [END]. Elastic and inelastic total cross sections are included, although inelastic cross sections were negligible at the energies used in this experiment. If no scattering occurs, the neutron escapes the target. If a scattering event occurs, the new energy and angle of the neutron is determined according to angular distributions obtained from ENDF and JENDL [JEN90]. The angular distributions for ^{2}H(n,n) and ^{12}C(n,n) are fit with Legendre polynomials, and the coefficients of these fits are imported into NCOR. The scattering location is chosen randomly along the initial neutron trajectory, and the new neutron energy, location and direction are assigned. This process repeats until the neutron either escapes the target or drops below some energy cutoff. Almost any number of multiple scattering events is therefore possible.

Once a neutron escapes the target, NCOR checks to see if it intersects any of the detectors. Generally, two detector positions are defined, corresponding to the positions of a single detector in and out of the γ-ray plane of polarization. If the neutron does intersect one of these detector positions, the probability of detecting the neutron is calculated. A neutron is considered "detected" if it scatters elastically from a hydrogen nucleus in the detector. Scattering from a carbon nucleus is not considered "detected", because the recoil of the carbon nucleus produces insufficient scintillation to be detected by the photomultiplier tube. The detection probability is therefore determined by the H(n,n) cross section and the distance the neutron travels through the detector volume. If the neutron interacts in the detector, NCOR determines whether enough energy was deposited in the detector to overcome the hardware and software detector thresholds. Because a given neutron can deposit anywhere from its full energy to almost zero energy in the detector, the probability of registering a "good" event is determined by estimating the detector response function.

The response function is determined by assuming that the neutron will deposit any fraction of its total energy with approximately equal probability. The probability of detecting the event is therefore proportional to the ratio of the area of the response function above the detector threshold to the area of the entire response function. This approximation for detector response, illustrated in Figure 6.6, is only accurate to first order, as an actual detector response is more complicated. The effect of these differences will be minimized in the present calculation, however, because the differences will apply equally to all the detectors used in this relative measurement. If NCOR determined that the neutron is detected, the counter corresponding to the appropriate detector is incremented, and the total time of flight of the neutron from photodisintegration to detection is recorded. NCOR repeats this process for additional neutrons until sufficient statistics are gathered to determine the measured asymmetry corresponding to the user-defined initial angular distribution.

To test the reliability of the simulation, NCOR was used to reanalyze the results of the 1996 ^{2}H($\vec{\gamma}$, n)p measurement described in Section 3.2.5. Using the geometry and materials previously described, NCOR was run assuming an initial neutron angular distribution given by

$$\sigma(\theta, \phi) = 0.0565 + \sin^2\theta\,(1 + \cos 2\phi)\,, \tag{6.5}$$

which, when used with the asymmetry expression given in Equation 4.9, gives an asymmetry of 0.95, in agreement with previous measurements made by [Bia81]. For the angular distribution of Equation 6.5, NCOR calculated that the analyzing power measured in the laboratory should be 0.836. This is in excellent agreement with the measured value of 0.82 ± 0.05.

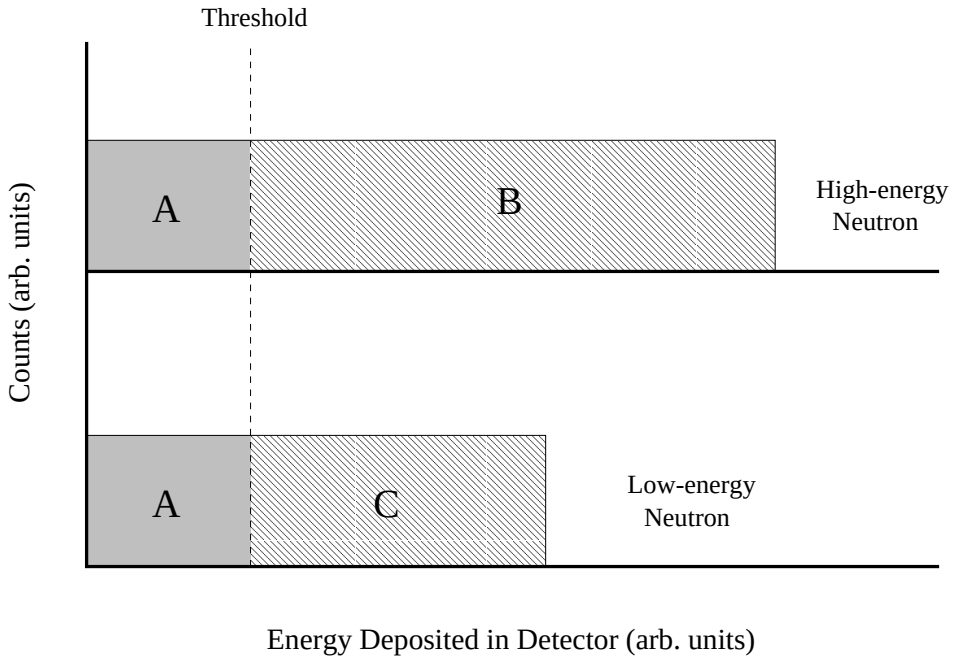

Figure 6.6: Estimation of detector response used in NCOR. Assuming that a neutron will deposit any fraction of its incident energy into the detector with equal probability produces the rectangular response function shown above. The probability of the high-energy neutron depositing enough energy to overcome the threshold is B/(A+B). The probability for the low-energy neutron depositing sufficient energy is C/(A+C).

6.2.2 Simulation Results

NCOR was run repeatedly for each detector configuration until the simulated asymmetry matched the experimental results found in Table 6.1. The resulting values for the parameter R from the initial distribution described in Equation 6.3 were found to be 0.0655 for detector one and 0.0705 for detector four. Time of flight spectra were generated for each detector position, producing the spectra shown in Figure 6.7 and Figure 6.8. These spectra are in good agreement with the measured spectra shown in Figure 6.4 and Figure 6.5, respectively.

These values for R correspond to "pure" asymmetries of 79.4% and 78.0% for

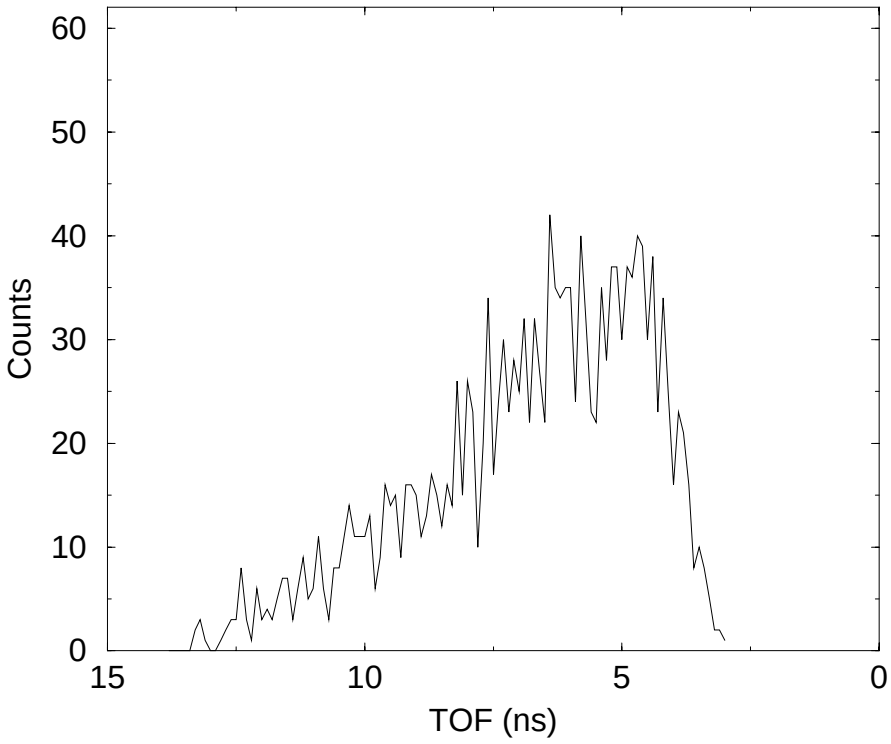

Figure 6.7: Simulated TOF spectra for a detector in the plane of γ-ray polarization.

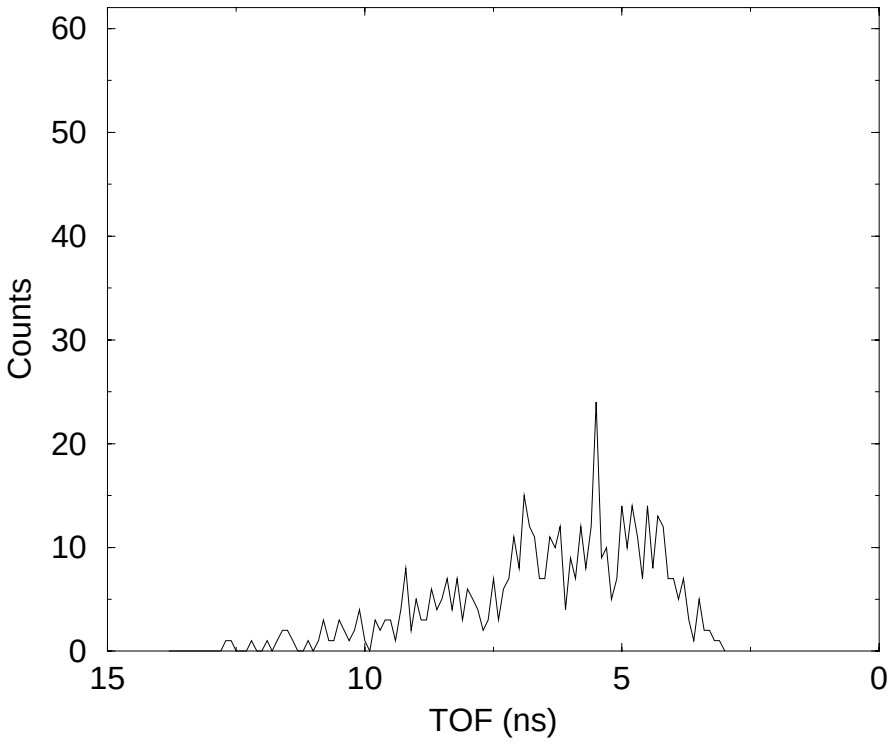

Figure 6.8: Simulated TOF spectra for a detector perpendicular to the plane of γ-ray polarization.

Detector	R	Asymmetry	$\%S$ Contribution (M1)
1	0.0655 ± 0.02	0.794 ± 0.05	$8.95\% \pm 2.5\%$
4	0.0705 ± 0.02	0.780 ± 0.05	$9.56\% \pm 2.5\%$
TOTAL		0.787 ± 0.035	$9.21\% \pm 1.8\%$

Table 6.2: Simulation results for asymmetry and s-wave (M1) contribution.

detector one and detector four, respectively. The relative s-wave contributions can be extracted from the R values by noting the relative contributions of the s-wave and p-wave components to the total cross section, as shown in Equation 4.12. This gives

$$\%S = \frac{\frac{9}{4}R}{\frac{9}{4}R + \frac{3}{2}}. \tag{6.6}$$

The resulting s-wave (M1) contributions are given in Table 6.2. The errors reported in the table are statistical only, and are based on the experimental errors of the measured asymmetries reported in Table 6.1. The error was determined by noting that

$$\sigma_R^2 = \left(\frac{\partial R(A)}{\partial A}\right)^2 \sigma_A^2 = \left(-\frac{\sin^2\theta\sigma_A}{A^2}\right)^2 \simeq \left(\frac{\sigma_A}{4A^2}\right)^2, \tag{6.7}$$

where R is expressed in terms of the measured asymmetry A by writing Equation 6.3 as an asymmetry, and $\sin^2\theta$=1/4 for θ=150°. The error in the s-wave contribution is similarly determined by noting

$$\sigma_S^2 = \left(\frac{\partial S(R)}{\partial R}\right)^2 \sigma_R^2 = \left(\frac{6\sigma_R}{(2+3R)^2}\right)^2, \tag{6.8}$$

where $S(R)$ is taken from Equation 6.6.

6.2.3 Simulation Sensitivity and Systematic Errors

The errors on the s-wave contribution reported above are purely statistical. To obtain the total error on the measurement, the possible uncertainties in the Monte

Carlo simulation and the physical apparatus must also be considered. The uncertainties intrinsic to the Monte Carlo code arise from the physical assumptions made. Because the majority of the code consists of straightforward kinematics and geometry, these uncertainties are small when compared to the statistical uncertainties associated with the data. One physical assumption is that the distribution of outgoing neutrons can be accurately represented by Equation 6.3. This assumption is only correct if contributions from higher-order multipoles are negligible when compared to the electric and magnetic dipole contributions. Calculations by Arenhövel [Are99] have indicated that the next higher-order multipole strengths, E2 and M2, are three orders of magnitude weaker than the E1 and M1 strengths, implying that these terms would make only a negligible contribution to the cross section. A second possible uncertainty arises form the treatment of detector efficiency in the program. Although the approximations used are certainly only accurate to several percent, these uncertainties will contribute very little to the overall error because the asymmetry measurement only deals with the relative count rate in each detector. The approximation applies with equal accuracy both in and out of the γ-ray polarization plane, and will therefore not significantly effect the final result.

An additional set of physical assumptions made by NCOR are the values for the neutron scattering cross sections obtained from ENDF. The cross sections reported in ENDF represent a combination of measurements, calculations, and extrapolations, and can therefore only be considered accurate to a certain degree. Furthermore, NCOR interpolates between these ENDF values for neutrons having energies between those listed in the tables. The simulation was therefore tested to see how sensitive the results are to the specific values in the tables. Varying the cross sections by $\pm 5\%$ was found to alter the simulation result by less than 3%, which again is much smaller

	Detector 1	Detector 2
Statistical	8.95% + 2.50% - 2.50%	9.56% + 2.50% - 2.50%
Cross section	8.95% + 0.23% - 0.13%	9.56% + 0.22% - 0.32%
Detector position	8.95% + 1.15% - 1.45%	9.56% + 0.79% - 1.35%
Detector angle	8.95% + 2.25% - 2.19%	9.56% + 2.34% - 2.46%
Target angle	8.95% + 0.92% - 0.54%	9.56% + 1.09% - 0.95%
Total	8.95% + 3.68% - 3.67%	9.56% + 3.69% - 3.89%
FINAL RESULT	9.26% + 2.6% - 2.7%	

Table 6.3: Error analysis for the s-wave contribution to the ^{2}H($\vec{\gamma}$, n)p cross section for E_γ=3.58 MeV. The five largest sources of error are listed. Negligible contributions are not listed.

than the statistical uncertainty. The results of this variation are presented with the effects of other uncertainties in Table 6.3. Overall the uncertainties arising from the Monte Carlo simulation make only a minor contribution to the overall error on the measurement.

The remaining systematic errors arise from uncertainties in the position of the physical apparatus. The apparatus was set up very carefully, but the accuracy of the positions and angles can not be assumed to be better than 5%. Because the separation of the target and detectors is comparable to the target and detector sizes, small changes in relative orientation can have a considerable effect on the neutron distributions viewed by a given detector. Each detector covers a relatively broad angular range, so the neutron intensity can not be assumed to be constant throughout the detector volume. Because of this, the uncertainties in the detector and target positions can not be treated simply as uncertainties in solid angle.

To account for these uncertainties, the parameters defining the location and orientation of the apparatus were independently varied within NCOR, and the effect on the final result was calculated. The largest effect came from varying the position of

Calculation	Type	%M1 contribution	$\Sigma(150^\circ)$
Arenhövel [Are99]	Direct	7.31%	0.810
Chen *et al.* [Che99b]	EFT	7.85%	0.810
Rupak [Rup00]	EFT	7.51%	
Experiment		9.26+2.6-2.7%	0.786±0.052

Table 6.4: Comparison of theoretical and experimental results. The errors reported with the experimental results include statistical and systematic uncertainties.

the detectors with respect the the target. This is because the detectors are placed at an angle at which the analyzing power changes rapidly with angle, as shown in Figure 4.1. This allows a 5% uncertainty in detector orientation to create as much as a 25% uncertainty in the final s-wave contributions. The errors arising from the orientation of the target, while considerable, were less dramatic.

The contributions of all the statistical and systematic errors are shown in Table 6.3. Combining the results of the two detectors gives an overall s-wave contribution of $9.26\% + 2.6\% - 2.7\%$. The corresponding asymmetry to this s-wave contribution is 0.786 ± 0.052, where the uncertainty includes statistical and systematic errors.

6.3 Comparison with Theory

The theoretical methods discussed in Chapter 4 have been used to calculate the relative E1 and M1 contributions to the ^{2}H$(\vec{\gamma}, \mathrm{n})$p cross section. The results from one direct calculation and two effective field theory calculations are presented in Table 6.4. All three calculations for the percentage M1 contribution are in reasonable agreement with each other. Because the contributions to the cross section are calculated under different assumptions in each theoretical treatment, as described in Chapter 4, the correspondence of M1 strength to asymmetry results differs for each theory, allowing

different M1 contributions to correspond to the same asymmetry.

The experimental results are in reasonable agreement with the theoretical predictions, and are presented in Table 6.4. The uncertainties associated with the measurement do not allow the experimental results to discern between the predictions of the different theoretical methods. The experimental results are plotted against the potential model and effective field theory calculations in Figure 6.9 and Figure 6.10, respectively. In both cases, the experimental data supports the theoretical predictions, and lends credibility to the extrapolation of the M1 strength down to lower energies, eventually connecting with well-determined M1 dominated cross sections at thermal energies.

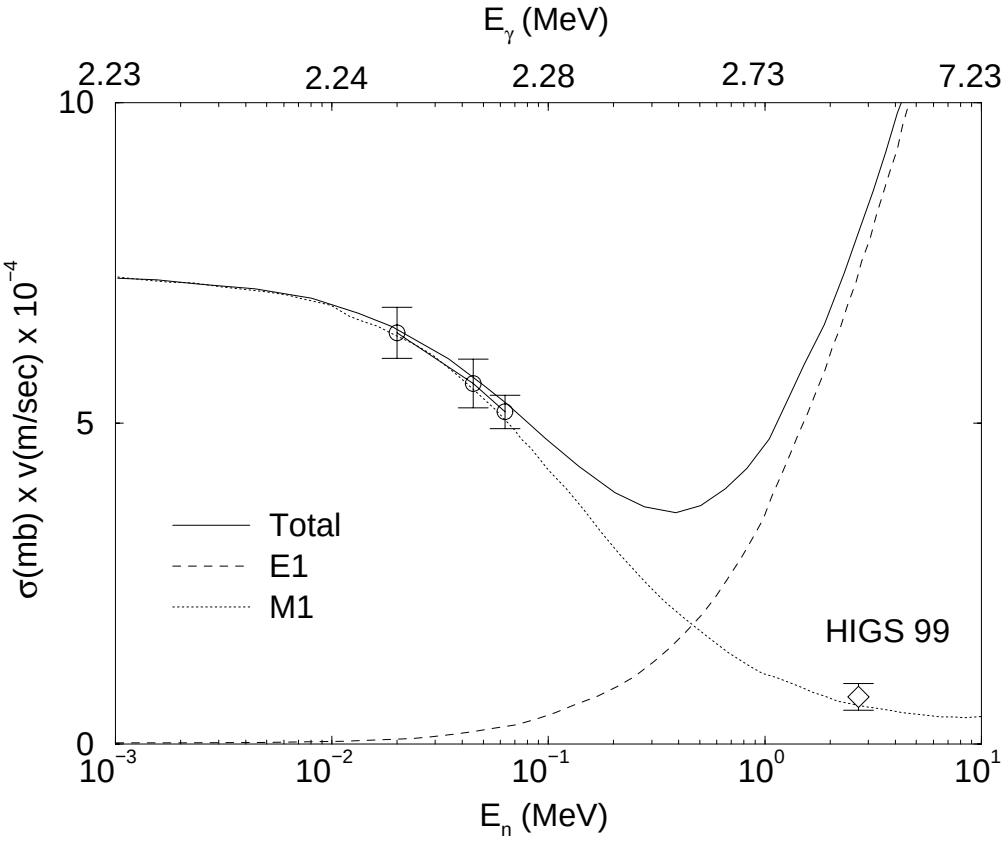

Figure 6.9: Comparison of HIGS data with the AV18 potential model calculation by Sato *et al.* [Sat95]. The HIGS data (diamond) represents the M1 contribution to the total cross section. The previous measurements (circles) represent a total cross section measurements in an energy region dominated by the M1 transition [Nag97].

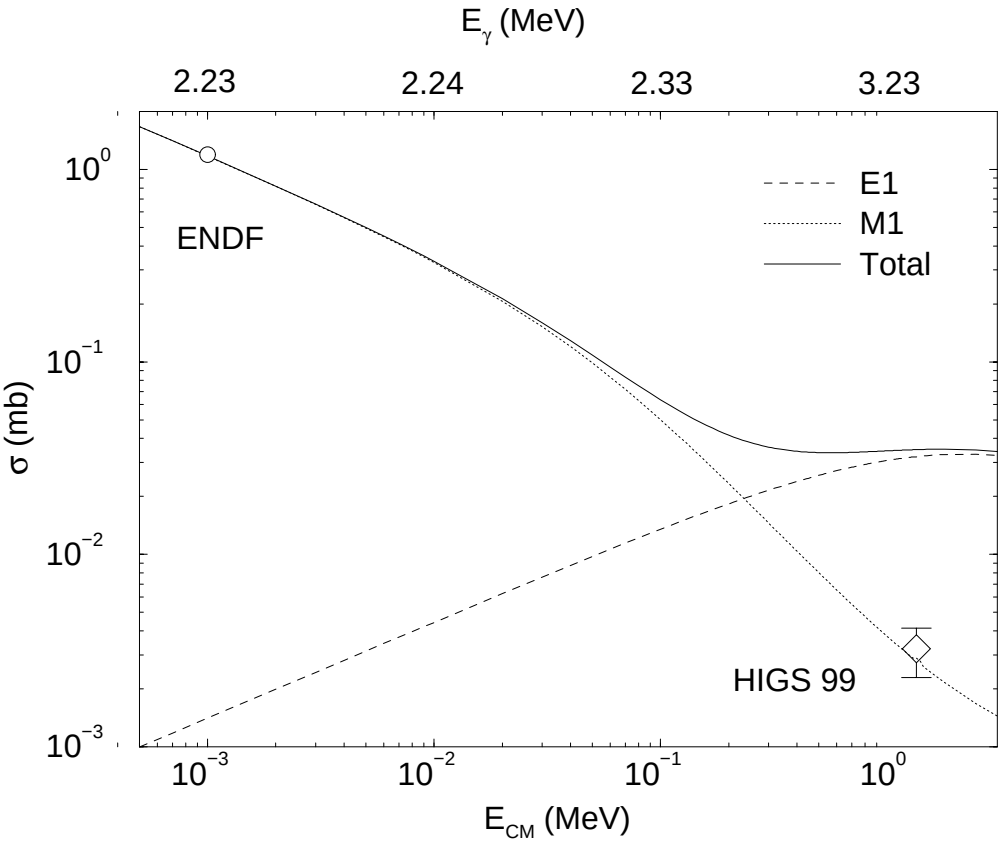

Figure 6.10: Comparison of HIGS data with EFT calculation by Chen *et al.* [Che99b]. The HIGS data (diamond) represents the M1 contribution to the total cross section. The previous measurement (circle) represents a total cross section measurement at an energy dominated by the M1 transition [END]. The free parameters in the calculation are defined to reproduce the cross section at thermal energies.

Chapter 7

Conclusions and Prospects

7.1 HIGS Facility

The measurement of the M1 contribution to the ^{2}H$(\vec{\gamma}, \mathrm{n})$p cross section was the first nuclear physics experiment performed at HIGS, and represents the first step in the wide-ranging nuclear physics program planned for HIGS and briefly described in Section 1.4. The measurements of the γ-ray beam described in Chapter 3 demonstrate that the HIGS facility is performing according to expectations and is generating γ-ray beams with a unique set of properties unavailable at any other nuclear physics facility. Gamma-rays have been generated and measured having energies ranging from 2.8 to 55.0 MeV with energy resolutions as low as $\Delta E/E = 0.76\%$ and at fluxes as high as $10^6\gamma$'s/sec. Measurements of the polarization of the γ-rays are consistent with the 100% linear polarization predicted by theory and simulations.

These presently available beam parameters, already shown to be useful for early nuclear physics studies, represent a minimum set of capabilities that will be greatly

expanded upon when the facility is fully developed. Several improvements scheduled for the near future will help realize this expanded potential. Modifications made to the electron beam optics in the storage ring will extend the operating parameters to the design limits, allowing electron energies up to 1.1 GeV and average currents ultimately as high as one Ampere. This will allow γ-ray operation at the full energies and intensities discussed in Chapter 2. The installation of a booster injector ring [Lab98] will allow the continuous injection of electrons into the storage ring at full beam energy, allowing continuous operation without the need to halt an experiment to replenish the stored electrons. Finally, a helical undulator is being developed that, when installed, will provide increased laser and γ-ray intensities, as well as allow different polarization states.

Ultimately, the HIGS facility will be able to produce γ-ray beams having energies ranging from 2 to 200 MeV having fluxes of up to $10^{11}\gamma$'s/sec over all energies. Gamma-rays with horizontal, vertical, and left and right circular polarization states will be available, and energy resolutions as low as $\Delta E/E = 0.1\%$ will be achievable. These γ-ray beams make a diverse and interesting body of experiments possible. The unique capabilities of the HIGS facility will hopefully allow the Duke Free-Electron Laser Laboratory, Triangle Universities Nuclear Laboratory, and the greater nuclear physics community to continue to collaborate and make important contributions in the field of photonuclear physics.

7.2 $^2\mathrm{H}(\vec{\gamma},\mathrm{n})\mathrm{p}$

The M1 contribution to the $^2\mathrm{H}(\vec{\gamma},\mathrm{n})\mathrm{p}$ cross section for 3.58 MeV γ-rays has been successfully measured at the HIGS facility. This measurement represents one of the

few experimental studies of the n-p system in the energy region where the E1 and M1 contributions to the cross section are dominant and believed to be of comparable magnitude, as shown in Figure 4.2. This experiment also represents the first time polarization observables have been used to determine the multipole properties of the cross section in this energy region. Previous measurements with polarized beam have only been performed in an energy region dominated by E1 and higher order transitions [Lik98].

As stated in Section 1.5.2, the p(n,γ)^{2}H cross section most relevant to big-bang nucleosynthesis (BBN) calculations involves a neutron center of mass energy between 25 and 200 keV [Bur99]. In the reverse reaction, this corresponds to photodisintegration using γ-rays having energies between 2.28 and 2.63 MeV. The measurement reported in this dissertation is therefore not directly applicable to current BBN calculations. However, the agreement with theory at E_γ =3.58 MeV lends credibility to the theoretical extrapolation down to the energies of interest, eventually connecting with the well-determined M1 dominated cross sections at thermal neutron energies [Cox65]. In addition, the method used for this measurement can easily be re-applied with lower γ-ray energies. The HIGS facility is designed to produce γ-rays with energies down to 2 MeV and below, so the entire energy range of interest to BBN calculations will be accessible. Because the γ-ray energy is continuously tunable throughout this energy region, the shape of the M1 contribution to the cross section can be determined to almost any desired energy resolution.

A central challenge of extending this program to lower energies involves the reduction of the uncertainties associated with the present measurement. Further development of the HIGS facility, discussed above in Section 7.1, will allow for higher γ-ray fluxes that will reduce the statistical uncertainties considerably. Given that the

fully developed HIGS facility is expected to produce γ-rays in the relevant energy region at fluxes at least five orders of magnitude greater than those achieved during the present experiment, the statistical uncertainties of future $^2\mathrm{H}(\vec{\gamma},\mathrm{n})\mathrm{p}$ measurements can quickly become negligible. A higher γ-ray flux will also allow a greater separation between the deuterium target and the detectors, relaxing the tight geometry that was responsible for much of the systematic error in the present measurement. The systematic errors can be further reduced by measuring the analyzing power at a laboratory angle of 90°, rather than the present measurement at 150°. As is shown in Figure 4.1, the analyzing power changes very little with angle between 60° and 120°. Small uncertainties in the detector position will therefore have very little effect on the observed neutron asymmetry, and will therefore contribute less to the overall systematic uncertainty. A 90° measurement was not possible in the present experiment, because the expected uncertainties would have made it difficult to distinguish the predicted analyzing power of 0.95 for $E_\gamma = 3.58$ MeV [Are99] from an analyzing power of 1.0 that would correspond to a $^2\mathrm{H}(\vec{\gamma},\mathrm{n})\mathrm{p}$ cross section with no M1 contribution. The higher statistics available in future experiments, combined with a greater M1 contribution to the cross section at lower energies leading to a reduced analyzing power at 90°, will remove the necessity of conducting the measurement at an angle at which the analyzing power varies quickly with angle. Ultimately, the use of additional detectors will allow us to measure a wide range of angles simultaneously. Given these improvements to the current experiment, we believe that a combined statistical and systematic uncertainty of 1% is ultimately achievable.

In addition to measurements of the relative M1 contribution to the cross section, the $^2\mathrm{H}(\vec{\gamma},\mathrm{n})\mathrm{p}$ total cross section can be measured directly. This would allow both the E1 and M1 contributions to the cross section to be determined absolutely, as opposed

to relatively as presented in this dissertation. If the measurements are made with small but achievable uncertainties, these experiments will provide a basis of comparison for the various theoretical methods used to calculate the $^2\mathrm{H}(\vec{\gamma},\mathrm{n})\mathrm{p}$ cross section, and will contribute to a better understanding of the n-p system in this understudied energy regime.

7.2.1 Summary of Results

The analyzing power at 150° for the $^2\mathrm{H}(\vec{\gamma},\mathrm{n})\mathrm{p}$ reaction using 3.58 MeV linearly polarized γ-rays has been measured at the HIGS facility. A raw analyzing power of 0.629 ± 0.021 was observed. Corrections for multiple scattering and finite geometry calculated a corrected analyzing power of 0.786 ± 0.052, where this error contains contributions from statistics, the uncertainties in the physical apparatus, and the Monte Carlo code. The M1 contribution to the $^2\mathrm{H}(\vec{\gamma},\mathrm{n})\mathrm{p}$ cross section at this energy was determined to be $9.26 + 2.6 - 2.7\%$. This result is in good agreement with both potential model and effective field theory calculations, which predict an average M1 contribution of 7.31% and 7.68%, respectively.

Appendix A

Pair Spectrometer Focal Plane

The relationship between the a charged particle's position on the focal plane ad the particle's momentum is described in Figure A.1. We define the origin of our coordinate system to be at the center of the magnetic field region. The point of exit of the particle from the magnetic field region of effective field radius (EFR) r must obey

$$x_m^2 + y_m^2 = r^2. \tag{A.1}$$

A particle that enters a circular field region at an angle perpendicular to the field boundary will exit the field along a trajectory normal to the field boundary. The location of the image (defined by x_f and y_f) can be related to the exit points by noting

$$\tan\psi = \frac{y_m}{x_m} = \frac{y_f}{x_m} \Rightarrow y_m = \frac{x_m y_m}{x_f} \tag{A.2}$$

Combining Equation A.1 and Equation A.2 gives

$$(x_m)^2 = \frac{r^2}{1 + \left(\frac{y_f}{x_f}\right)^2} \;;\; y_m = \frac{y_f}{x_f}\frac{r}{\sqrt{1 + \left(\frac{y_f}{x_f}\right)^2}} \tag{A.3}$$

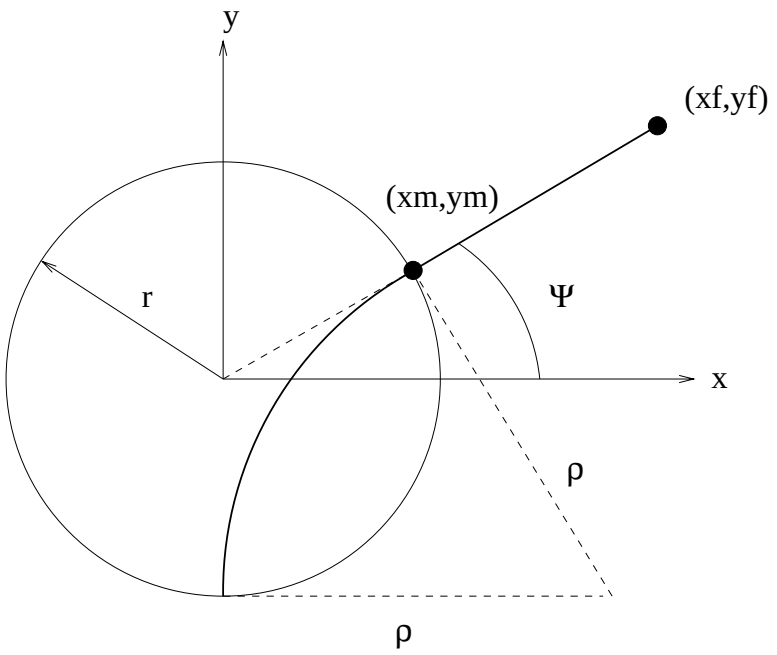

Figure A.1: Geometry for pair spectrometer used to obtain the focal plane equations. ρ is the radius of curvature for the particle through the field region of effective field radius r, (xm,ym) is the point of exit from the field, and (xf,yf) is the location of the image.

The above assumes an origin at point O. We now consider a new origin O" located at the center of curvature such that $x'' = x - \rho$ and $y'' = y + r$. By setting $x''^2 + y''^2 = \rho^2$, we get

$$\rho = \frac{x_m^2 + y_m^2 + 2y_m r + r^2}{2x_m} \tag{A.4}$$

Substituting the values from Eq. A.3, we get

$$\rho = r\left(\sqrt{1 + \left(\frac{y_f}{x_f}\right)^2} + \frac{y_f}{x_f}\right). \tag{A.5}$$

We can therefore determine the momentum of an electron or positron as a function of its intersection with the focal plane.

$$|p| = 2.998\ B[T]\ \rho[cm] \tag{A.6}$$

The inverse process can be used to determine the position on the focal plane corresponding to a given particle momentum. Because the resulting equations are more complicated, these values were calculated using a raytracing program.

Appendix B

Energy Loss for Charged Particles

Reconstucting the energy of an incident γ-ray with the SAL pair spectrometer described in Section 3.3.2 requires that the energies of the produced electrons and positrons are as well determined as possible. A calculation of the energy losses of the charged particles in the converter foil is therefore necessary. Following [Leo94], the energy loss can be described as

$$\left(\frac{dE}{dx}\right)_{tot} = \left(\frac{dE}{dx}\right)_{rad} + \left(\frac{dE}{dx}\right)_{coll}, \tag{B.1}$$

where "rad" refers to radiative losses through bremsstrahlung and "coll" refers to losses through collision with other electrons.

Radiative losses are only significant for electron and positron energies above a few MeV. At these energies, the bremsstrahlung cross section is given by

$$d\sigma = 4Z^2 r_e^2 \alpha \frac{d\nu}{\nu} \left\{ \left(1+\varepsilon^2\right) \left[\frac{phi_1(\xi)}{4} - \frac{1}{3}\ln Z - f(Z)\right] - \frac{2}{3}\varepsilon \left[\frac{\phi_2(\xi)}{4} - \frac{1}{3}\ln Z - f(Z)\right] \right\}, \tag{B.2}$$

where Z is the atomic number of the material, through which the particle is passing, r_e is the classical electron radius, and $\alpha = 1/137$ is the fine structure constant. ν is

the frequency of the emitted photon, and ε is E/E_o, where E and E_o are the final and initial energies of the electron, respectively.

The effect of electron screening is determined by the quantity ξ, which is given by

$$\xi = \frac{100 m_e c^2 h\nu}{E_o E Z^{1/3}}, \tag{B.3}$$

and the screening functions ϕ_1 and ϕ_2, where $m_e c^2$ is the electron rest mass and h is Plank's constant. For elements with $Z \geq 5$, the screening functions are empirically given by

$$\begin{gathered}\phi_1(\xi) = 20.863 - 2\ln\left[1 + (0.55846\xi)^2\right] - 4\left[1 - 0.6\exp(-0.9\xi) - 0.4\exp(-1.5\xi)\right]; \\ \phi_2(\xi) = \phi_1(\xi) - \tfrac{2}{3}\left(1 + 6.5\xi + 6\xi^2\right)^{-1}.\end{gathered} \tag{B.4}$$

Finally, the function $f(Z)$ corrects the Born approximation to include the interaction of the electron or positron in the electric field of the nucleus, and is given by

$$f(Z) \simeq a^2\left[\left(1 + a^2\right)^{-1} + 0.20206 - 0.0369a^2 + 0.0083a^4 - 0.002a^6\right], \tag{B.5}$$

where $a = Z/137$.

The total energy loss due to radiation can be calculated by integrating the cross section times the photon energy over all possible photon energies, giving

$$-\left(\frac{dE}{dx}\right)_{rad} = N\int_0^{\nu_0} h\nu \frac{d\sigma}{d\nu}(E_0, \nu)\, d\nu \tag{B.6}$$

where N is the number of atoms/cm^3 and $\nu_o = E_o/h$. This expression was integrated numerically to determine the radiation contribution to the energy losses reported in Section 3.3.2.

The energy lost through collisions with electrons is calculated with a slightly modified Bethe-Bloch formula. Because the original formula dealt with the collision

losses of heavy charged particles instead of electrons, corrections were made to account for the indistinguishability of the scattering particles, and for the possible deflection of the electrons, which would not be experienced by heavier particles. The expression for collisional energy losses becomes

$$-\left(\frac{dE}{dx}\right)_{coll} = 2\pi N_a r_e^2 m_e c^2 \rho \frac{Z}{A}\frac{1}{\beta^2}\left[\ln\frac{\tau^2(\tau+2)}{2\,(I/m_e c^2)\,2} + F(\tau)\right], \tag{B.7}$$

where τ is the kinetic energy of the electron in units of $m_e c^2$, and $\beta = v/c$. The mean excitation potential I can be approximated by

$$\begin{aligned} I/Z &= 12 + 7/Z \text{ eV} && \text{for} \quad Z < 13 \\ I/Z &= 9.76 + 58.8 Z^{-1.19} \text{ eV} && \text{for} \quad Z \geq 13. \end{aligned} \tag{B.8}$$

The energy losses for electrons and positrons is slightly different, with

$$\begin{aligned} F(\tau)_{electron} &= 1 - \beta^2 + \frac{\frac{\tau^2}{8} - (2\tau+1)\ln 2}{(\tau+1)^2} \\ F(\tau)_{positron} &= 2\ln 2 - \frac{\beta^2}{12}\left(23 + \frac{14}{\tau+2} + \frac{10}{(\tau+2)^2} + \frac{4}{(\tau+2)^3}\right). \end{aligned} \tag{B.9}$$

Bibliography

[Are91] H. Arenhövel and M. Sanzone. *Photodisintegration of the Deuteron*. Number 3 in Few-Body Systems. Springer-Verlag, 1991.

[Are99] H. Arenhövel, 1999. Private Communication.

[Aru64] F. R. Arutyunian, I. I. Goldman, V. A. Tumanian, and Z. Eksperim. Soviet Physics, **JETP 18**(1964).

[Bal92] Mark J. Balbes. Ph.D. thesis, Duke University, 1992.

[Bar33] N. F. Barber. Proc. Leeds Phil. Lit. Soc. Sci. Sect., **2**(1933) 427.

[Ber71] V. B. Berestetskii, E. M. Lifshitz, and L. P. Pitaevskii. *Relativistic Quantum Theory*, volume 4 of *Course of Theoretical Physics*. Pergammon Press, 1971.

[Ber94] J. C. Bergstrom et al. Phys. Rev. C, **50**(1994) 2979.

[Ber97] J. C. Bergstrom, R. Igarashi, and J. M. Vogt. Phys. Rev. C, **55**(1997) 2023.

[Bet34] H. A. Bethe and W. Heitler. Proc. Roy. Soc., **A146**(1934) 83.

[Bet35] H. A. Bethe and C. Longmire. Proc. Roy. Soc., **A148**(1935) 146.

[Bet53] H. A. Bethe and J. Ashkin. In E. Segrè, editor, *Experimental Nuclear Physics*, volume 1. John Wiley and Sons, 1953.

[Bia81] W. Del Bianco, L. Federici, G.Giordano, G. Matone, G. Pasquariello, P. Picozza, R.Caloi, L. Casano, M. P. De Pascale, L. Ingrosso, M. Mattioli, E. Polidi, C. Scaerf, P. Pelfer, D. Prosperi, S. Frullani, B. Girolami, and H. Jeremie. Phys. Rev. Lett., **47**(1981) 1118.

[Bis50] G. R. Bishop. Phys. Rev., **80**(1950) 211.

[Bra90] C. A. Brau. *Free-Electron Lasers.* Academic Press, 1990.

[Bro56] C. Browne and W. Buechner. The Review of Scientific Instruments, **27**(1956).

[Bur99] S. Burles, K. M. Nollette, J. W. Truran, and M. .S. Turner. Phys. Rev. Lett., **82**(1999) 4176.

[But68] H. Von Buttlar. *Nuclear Physics: An Introduction.* Academic Press, 1968.

[Cam82] A. Cambi, B. Mosconi, and P. Ricci. Phys. Rev. Lett., **48**(1982) 462.

[Can83] Canberra Industries, Inc., One State Street, Meriden, CT 06450. *Pulse Shape Discriminator Model 2160A Operator's Manual*, 1983.

[Car96] T. Scott Carman, Vladimir Litvinenko, John Madey, Charles Neuman, Patrick G. O'Shea, N. Russell Roberson, Carol Y. Scarlett, Eric Schreiber, and Henry R. Weller. NIM A, **378**(1996) 1.

[Car98] J. Carlson and R. Schiavilla. Rev. Mod. Phys., **70**(1998) 743.

[Cha34] J. Chadwick and M. Goldhaber. Nature, **134**(1934) 237.

[Che99a] J. Chen, G. Rupak, and M. J. Savage. *Nucleon-Nucleon Effective Field Theory Without Pions*, 1999. nucl-th/9902056.

[Che99b] J. Chen and M. J. Savage. Phys. Rev. C, **60**(1999).

[Cox65] A. E. Cox, S. A. R. Wynchank, and C. H. Collie. Nucl. Phys., **74**(1965) 497.

[DeB64] S. DeBenedetti. *Nuclear Interactions.* John Wiley & Sons, 1964.

[Don92] J. F. Donoghue, E. Golowich, and B. R. Holstein. *Dynamics of the Standard Model.* Cambridge University Press, 1992.

[END] *Data Formats and Procedures Manual for Evaluated Nuclear Data File, ENDF-6.* BNL-NCS-44945.

[Fuc96] M. Fuchs et al. Phys. Letts. B, **368**(1996) 20.

[Gas85] J. Gasser and H. Leutwyler. Nucl. Phys., **B250**(1985) 465.

[Gol62] J. Goldstone, A. Salam, and S. Weinberg. Phys. Rev., **127**(1962) 965.

[Gro93] F. Gross. *Relativistic Quantum Mechanics and Field Theory.* John Wiley and Sons, Inc., 1993.

[Hay70] E. Hayward. *Photonuclear Reactions.* National Bureau of Standards Mongraph 118, August 1970.

[Hol95] B. R. Holstein. *Chiral Perturbation Theory: A Primer.* In G. Kilcup, S. Sharpe, W. C. Haxton, and E. M. Henley, editors, *Proceedings of the 1993 Uehling Summer School, Phenomenology and Lattice QCD*, page 1. World Scientific, 1995. hep-ph/9510344.

[How96] C. R. Howell, 1996. Private Communication.

[Jac75] J. D. Jackson. *Classical Electrodynamics.* John Wiley and Sons, Inc., 1975.

[JEN90] *Japanese Evaluated Nuclear Data Library, Version 3*, 1990. JAERI-1319.

[Ji90] X. Ji et al. Phys. Rev. C, **41**(1990) 1736. and references contained therein.

[Kap98a] D. B. Kaplan, M. J. Savage, and M. B. Wise. Nucl. Phys., **B424**(1998) 390.

[Kap98b] D. B. Kaplan, M. J. Savage, and M. B. Wise. Nucl. Phys. B, **534**(1998) 329.

[Kap99] D. B. Kaplan, M. J. Savage, and M. B. Wise. Phys. Rev. C, **59**(1999) 617.

[Kle30] O. Klein and Y. Nishina. I. E. Tamm, (1930).

[Kra88] K. S. Krane. *Introductory Nuclear Physics.* John Wiley and Sons, 1988.

[Lab98] Triangle Universities Nuclear Laboratory. *A Free-Electron Laser Generated γ-ray Beam for Nuclear Physics.* Submitted to the U. S. Department of Energy, October 1998.

[Leo94] W. R. Leo. *Techniques for Nuclear and Particle Physics Experiments.* Springer-Verlag, 1994.

[Lik98] V. P. Likachev et al. Nucl. Phys. A, **628**(1998) 597.

[Lit93] V. N. Litvinenko, J. M. J. Madey, and N. A. Vinokurov. *UV-VUV FEL Program at Duke Storage Ring with OK-4 optical klystron.* In *Proc. of 1993 IEEE Particle Accelerator Conference, Washington D. C.*, page 1442, 1993.

[Lit95] V. N. Litvinenko et al. *Comissioning of the Duke Storage Ring.* In *Proc. Particle Accelerator Conf.*, pages 213–215, 1995.

[Lit96a] V. N. Litvinenko, 1996. Private Communication.

[Lit96b] V. N. Litvinenko and J. M. J. Madey. Nucl. Intr. Meth, **A 375**(1996) 580.

[Lit97] V. N. Litvinenko, B. Burnham, M. Emamian, N. Hower, J. M. J. Madey, P. Morcombe, P. G. O'Shea, S. H. Park, R. Sachtschale, K. D. Straub, G. Swift, P. Wang, Y. Wu, R. S. Canon, C. R. Howell, N. R. Roberson, E. C. Schreiber, M. Spraker, W. Tornow, H. R. Weller, I. V. Pinayev, N. G. Gavrilov, M. G. Fedotov, G. N. Kulipanov, G. Y. Kurkin, S. F. Mikhailov, V. M. Popik, A. N. Skrinsky, N. A. Vinokurov, B. E. Norum, A. Lumpkin, and B. Yang. Phys. Rev. Lett., **78**(1997) 4569.

[Lit99] V. N. Litvinenko, S. H. Park, I. V. Pinayev, Y. Wu, M. Emamian, N. Hower, P. Morcombe, O. Oakeley, G. Swift, and P. Wang. Nucl. Intr. Meth., **A 429**(1999) 151.

[Lit00] V. N. Litvinenko, 2000. Private Communication.

[Liv69] J. J. Livingood. *The Optics of Dipole Magnets.* Academic Press, 1969.

[Lut68] G. Lutz. Nuovo Cimento, **17a**(1968) 332.

[L'v90] A. I. L'vov. Sov. J. Nucl. Phys., **34**(1990) 597. and Private Communication.

[Mac87] R. Machleidt, K. Holinde, and Ch. Elster. Phys. Rep., **149**(1987) 1.

[Mac95] B. E. MacGibbon, G. Garino, M. A. Lucas, A. M. Nathan, G. Feldman, and B. Dolbilkin. Phys. Rev. C, **52**(1995) 2097.

[Mad71] J. M. J. Madey. J. Appl. Phys., **42**(1971) 1906.

[Mar85] Thomas C. Marshal. *Free-electron Lasers.* Macmillan, Inc., 1985.

[Mei94] U. G. Meißner. *Baryon Chiral Perturbation Theory A.D. 1994*, November 1994.

[Mil63] R. H. Milburn. Phys. Rev. Lett., **10**(1963) 75.

[Nag97] Y. Nagai, T. S. Suzuki, T. Kikuchi, T. Shima, T. Kii, H. Sato, and M. Igashira. Phys. Rev. C, **56**(1997) 3173.

[Nel85] W. R. Nelson, H. Hirayama, and D. W. O. Rogers. *The EGS4 Code System.* SLAC, 1985.

[Nor94] B. E. Norum. *Polarized Photons for Nuclear and Particle Physics.* In V. Burkert, editor, *Proceedings of the Workshop on Spin Degrees of Freedom in Electromagnetic Nuclear Physics*, page 123, 1994.

[Par98] S. H. Park, V. N. Litvinenko, B. Burnham, Y. Wu, J. M. J. Madey, R. S. Canon, C. R. Howell, N. R. Roberson, E. C. Schreiber, M. Spraker, W. Tornow, H. R. Weller, and I. V. Pinayev. Nucl. Intr. Meth., **A 407**(1998) 224.

[Par99] S. H. Park, 1999. Private Communication.

[Par00] S. H. Park. Ph.D. thesis, Duke University, 2000.

[Rei68] R. V. Reid. Ann. Phys., **50**(1968) 411.

[Rin82] A. Rindi. Health Physics, **42**(1982) 187.

[Ris72] D. O. Riska and G. E. Brown. Phys. Lett., **38B**(1972) 193.

[Rup99] G. Rupak. *Precision Calculation of $np \to d\gamma$ Cross Section for Big-Bang Nucleosynthesis*, 1999. nucl-th/9911018 v2.

[Rup00] G. Rupak, 2000. Private Communication.

[San83] A. M. Sandorfi et al. IEEE Trans. Nucl. Sci., **NS-30**(1983) 3083.

[Sat95] T. Sato, T. Niwa, and H. Ohtsubo. *Radiative Capture of a Low-Energy Neutron by a Proton.* In H. Ejiri, T. Kishimoto, and T. Sato, editors, *Weak and Electromagnetic Interactions in Nuclei*, page 488. World Scientific, 1995.

[Sch96] G. Schmid, R. M. Chastler, C. M. Laymon, H. R. Weller, E. F. Moore, C. R. Bybee, J. M. Drake, D. R. Tilley, G. Vavrina, and P. M. Wallace. Nucl. Phys., **A607**(1996) 139.

[Sch97] G. J. Schmid, B. J. Rice, R. M. Chastler, M. A. Godwin, G. C. Kiang, L. L. Kiang, C. M. Laymon, R. M. Prior, D. R. Tilley, and H. R. Weller. Phys. Rev. C, **56**(1997) 2565.

[Sie37] A. J. F. Siegert. Phys. Rev., **52**(1937) 787.

[Sig94] James R. Sigurdson. *A Magnetic Pair Spectrometer to Detect Photon Splitting.* Master's thesis, Univeristy of Saskatchewan, 1994.

[Wel81] H. R. Weller and N. R. Roberson. IEEE Trans. Nucl. Sci., **NS-28**(1981) 1268.

[Wel92] H. R. Weller, J. Langenbrunner, R. M. Chastler, E. L. Tomusiak, J. Asai, R. G. Seyler, and D. R. Lehman. Atomic Data and Nucl. Data Tables, **50**(1992) 29.

[Wir95] R. B. Wiringa, V. G. J. Stoks, and R. Schiavilla. Phys. Rev. C, **51**(1995) 38.

[Wu93] Y. Wu, V. N. Litvinenko, and J. M. J. Madey. *Lattice and Dynamic Aperture of the Duke FEL Storage Ring.* In *Proc. of the 1993 IEEE Particle Accelerator Conference, Washington D. C.*, page 218, 1993.

[Wul98] E. A. Wulf. Ph.D. thesis, Duke University, 1998.

Biography

Eric Charles Schreiber

Personal

- Born in Columbus, Ohio on September 2, 1970

Education

- B.S. Physics, University of Notre Dame, Notre Dame, Indiana, 1993
- A.M. Physics, Duke University, Durham, North Carolina, 1996

Positions

- Teaching Assistant, Duke University, 1993-1995
- Research Assistant, Duke University, TUNL, 1994-2000
- Recitation Professor, Duke University, 1998-1999

Appointments

- Henry W. Newson Fellowship for Nuclear Physics, 1999-2000
- Preparing Future Faculty Fellow, 1997-1999

Publications

First Measurement of the Near-threshold $^2\mathrm{H}(\vec{\gamma},\mathrm{n})\mathrm{p}$ *Analyzing Power using a Free-Electron Laser Based Gamma-ray Source*
E. C. Schreiber, *et al.* To be published in Phys. Rev. C

Radiographic Tomography using Near-monochromatic γ-rays
E. C. Schreiber and P. G. O'Shea, Proc. SPIE **3154** (1997) 94

Gamma-ray Production in a Storage Ring Free-Electron Laser
V. N. Litvinenko *et al.* Phys. Rev. Lett. **78** (1997) 4569